

**UNIVERSITÀ
DEGLI STUDI
DI PADOVA**

Sede Amministrativa: Università degli Studi di Padova
Dipartimento di Tecnica e Gestione dei Sistemi Industriali

SCUOLA DI DOTTORATO DI RICERCA IN INGEGNERIA MECCATRONICA E DELL'INNOVAZIONE
MECCANICA DEL PRODOTTO

INDIRIZZO DI MECCATRONICA

CICLO XXX

Hardware in the loop, all-electronic wind turbine emulator for grid compliance testing

Direttore della Scuola: Ch.mo Prof. Roberto Caracciolo

Coordinatore di Indirizzo: Ch.mo Prof. Roberto Caracciolo

Supervisore: Ch.mo Prof. Paolo Mattavelli

Dottorando: Andrea Petucco

2017

Andrea Petucco:

Hardware in the loop, all-electronic wind turbine emulator for grid compliance testing,

© October 2017

SUPERVISOR:

Paolo Mattavelli

LOCATION:

Vicenza

TIME FRAME:

October 2017

A Matilde, Cristina, Gianni e Francesco

ABSTRACT

During the last years the distribution of renewable energy sources is continuously increasing and their influence on the distribution grid is becoming every year more relevant. As the increasing integration of renewable resources is radically changing the grid scenario, grid code technical requirements as [16–19, 31, 42–44] are needed to ensure the grid correct behavior. To be standard compliant wind turbines need to be submitted to certification tests which usually must be performed on the field. One of the most difficult tests to be performed on the field is the low voltage ride through (LVRT) certification due to the following reasons:

- The standards specify it must be performed at different power levels. For this reason it is necessary to wait for the right atmospheric conditions.
- It requires a voltage sag generator which is usually expensive and bulky.
- The voltage sag generator needs to be cabled between the grid and the wind turbine.
- The voltage sag generator causes disturbances and perturbation on the power grid, for this reason agreements with the distributor operator are needed.

For all these reasons a laboratory test bench to perform the LVRT certification tests on wind turbines would be a more controlled and inexpensive alternative to the classic testing methodology. The research presented in this thesis is focused on the design and the realization of a test bench to perform certification tests on energy converters for wind turbines in laboratory. More specifically, the possibility of performing LVRT certification tests directly in laboratory over controlled conditions would allow faster testing procedures and less certification overall costs. The solution presented in this thesis is based on a power hardware in the loop implementing a digitally-controlled, power electronics-based emulation of a wind turbine. This emulator is used to drive the electronic wind energy converter (WEC) under test. A grid emulator is used to apply voltage sags to the wind turbine converter and perform LVRT certification tests. In this solution AC power supplies are used to emulate both the wind turbine and the grid emulator. For this reason the test bench power rating is limited to the AC supplies one. Two working versions of the test bench have been realized and successfully tested. The work here presented has evolved through the following phases:

- Study of the grid code requirements and the state of the art.
- Modeling of the parts of a wind turbine and complete system simulations.

- Design and realization of the test bench.
- LVRT testing and results analysis.

Every phase will be presented in detail in the following chapters.

This thesis was typeset adopting the typographical *classichthesis* style
developed by André Miede

ACKNOWLEDGMENTS

First of all I would like to express my deep and sincere gratitude to Professor Matavelli, for giving me the opportunity to work with him. His profound knowledge, his problem solving mindset and his rigorous technical approach helped me to become a better engineer. More importantly, his humanity, kindness, tact and fairness in dealing with people has been a continuous source of life lessons that helped me to become a better person. Working with him has been a privilege I'll always be grateful for.

I wish to thank my fellow Ahmed Abdelhakim for his precious help during the beginning this PHD. His contribution to this work has been essential, especially during the model development phase. With his competence, enthusiasm and efficiency he saved me a lot of time, providing consistent results, which proven to be very useful during all the phases of this work.

I would like to thank my colleague and friend Tommaso Caldognetto. Besides the daily and enriching confrontation, and the multiple discussions on the passion for electronics we both share, I am grateful for his precious help in reviewing this manuscript.

I would like to thank all the colleagues and professors I share the integrated mechatronics engineering laboratory with: Francesco Cavazzana, Fabio Tinazzi, Roberto Losco, Riccardo Sgarbossa, Luca Dalla Santa, Aram Khodamoradi, Guangyuan Liu, Luca Tagliapietra, Antonio D'Andrea, Michele Vivian, Paolo Magnone, Roberto Oboe, Alessandro Sona and Mauro Zigliotto. Because of these people the last three years of this PHD have been a great experience, both on technical and personal level.

I would also like to express my gratitude to my family: Matilde for casting light over my life, for her everyday support, patience and dedication. My mother Cristina, my greatest life teacher, supporter and inspirational model. My father Gianni, to whom I own my practical oriented mindset, for his support during all the education years. My uncle Giulio and aunt Isabella for encouraging and supporting my passion for electronics since my early age. My brother Francesco for teaching me how to be a fighter in real life.

CONTENTS

1	INTRODUCTION	1
1.1	Background and motivation	1
1.2	Purpose of the thesis	2
1.3	Thesis contributions	3
I	WIND ENERGY SOURCES AND GRID CODE STANDARDS	5
2	WIND ENERGY SOURCES	7
2.1	Global scenario	7
2.2	Wind energy conversion	7
2.3	Wind turbine typologies	11
2.4	Fixed speed wind turbines	12
2.5	Variable speed wind turbines	13
2.5.1	Doubly fed induction generator based WTs	14
2.5.2	Full scale energy converter based WT	15
3	GRID CODE STANDARDS	17
3.1	Introduction	17
3.1.1	Voltage and frequency operating range	18
3.1.2	Active power regulation	19
3.1.3	Reactive Power regulation	19
3.1.4	Flicker	20
3.1.5	Current harmonics	21
3.1.6	Low Voltage Ride Through	21
3.2	Low voltage ride through certification	22
3.2.1	Impedance based voltage sag emulator	23
3.2.2	Generator based voltage sag emulator	24
3.2.3	Transformer based voltage sag emulator	25
3.2.4	Full converter based voltage sag emulator	26
3.2.5	Grid emulator	26
3.2.6	Quality certification test	27
3.3	State of the art on wind turbine emulators	28
II	MODELING AND SIMULATIONS	33
4	WIND TURBINE MODEL	35
4.1	Introduction	35
4.1.1	Wind	35
4.1.2	Rotor	36
4.1.3	Pitch angle controller	39

4.1.4	Gearbox	39
4.1.5	Generator	40
4.2	Models	41
4.3	Wind turbine rotor model	42
4.4	Pitch angle controller model	44
4.4.1	PI controller with angle gradient limiter	48
4.5	Drive train and gearbox model	50
4.6	Permanent magnet synchronous generator model	52
4.7	Overall wind turbine model	56
4.8	Wind energy converter model	56
4.8.1	Generator side converter	61
4.8.2	Generator side converter operation	61
4.8.3	Grid side converter	62
5	SIMULATIONS	63
5.1	Introduction	63
5.2	LVRT simulation results	63
III DESIGN AND REALIZATION		71
6	TEST BENCH DESIGN	73
6.1	introduction	73
6.2	Controllable power supply	75
6.3	Isolation transformer	75
6.4	External inductances	79
6.5	Sensing board	80
6.6	Real time hardware	81
6.6.1	National Instruments cDAQ	84
6.6.2	National Instruments cRIO	85
6.6.3	Texas Instruments TMS320F28377S microcontroller	86
6.7	cRIO programming and testing	88
6.8	TI LAUNCHXL-F28377S programming and testing	93
6.9	Impedance emulation	97
6.9.1	Resistive load	99
6.9.2	Current controlled inverter load	102
6.9.3	Inductance emulation in DQ reference frame	103
IV LOW VOLTAGE RIDE THROUGH TESTING		111
7	RESULTS	113
7.1	Introduction	113
7.2	Test procedure	113
7.3	LVRT test results	116
7.3.1	45% V_n - 390 ms symmetrical voltage sag LVRT test	117

7.3.2	45% V_n - 390 ms asymmetrical voltage sag LVRT test	120
7.3.3	Wind speed step variation	122
7.3.4	45% V_n 410ms symmetrical voltage sag LVRT test	122
7.4	On field tests	131
8	CONCLUSIONS	135
8.1	Future work	135
8.2	Other applications	136
	BIBLIOGRAPHY	137

INTRODUCTION

1.1 BACKGROUND AND MOTIVATION

The generalized diffusion of renewable energy sources (RES) is going to play a major role toward a sustainable future. During the last two decades their penetration into modern distributed power systems has increased rapidly and today is still far from reaching a plateau. The constant increase in renewable energy production from renewable sources, e.g. photovoltaics (PV) and wind turbines (WT), has introduced a wide variety of issues in distribution and transmission energy grids handling. As a matter of fact, those grids have initially been conceived to be powered by heavy power plants and to provide power to the users, which usually were only seen as passive utilizers. The radical change of power grid structural scenario, due to the massive increase of distributed energy generation from wind, PVs and hydroelectric sources, introduced the need for a new set of technical regulations focused on medium and small distributed energy sources.

As the reliability of the electrical grid is based on the quality of the injected energy and on how generators react to a grid failure, the distribution system operators (DSO) added a series of new standards to their grid codes to regulate the connection of renewable energy sources to the electricity grid. The grid code standards are conceived to regulate the interaction between the RES inverters and the grid. Generally, the grid code specifies how the distributed generators should behave during normal operation and how they should react to abnormal grid conditions. The requirements specified by the standards concern the generator steady state voltage and frequency range, its ability to inject reactive power into the grid, the possibility to modify its behavior accordingly to the DSO specific commands and its tolerance to grid faults. In particular, renewable energy sources should withstand any grid perturbation specified by the standards without being damaged and, in determinate conditions, without being disconnected from the grid.

As a consequence, before being connected to the grid, the new generation and conversion devices must comply with the rules specified by the respective grid code. For this reason, the generator must be submitted to a series of tests performed by a certification laboratory accordingly to the standards. More specifically, the tests specified for static generators without moving parts (e.g. , photovoltaic systems) are relatively simple to be performed, because the DC/AC converter certification can be done directly in the laboratory by using a DC power supply, instead of a PV source.

Differently, when the renewable energy source is based on moving parts, e.g. wind turbine generators, the standards specify a series of tests that must be performed on the field. This requirement considerably increases the overall complexity of the certification process. Additionally, on field tests are subjected to the aleatory behavior of the wind speed. The standard requirements heavily influence the design phase, so manufacturers and designers have to interact with the certification laboratory during both the design and certification phases and possibly modify their equipment during the review phase.

The most expensive, time consuming and delicate test to be performed on the field is the evaluation of the wind turbine ability to withstand power grid faults such as voltage sags. This particular kind of certification is called Low Voltage Ride Through (LVRT). To perform this test it is necessary to bring on the field an impedance based voltage sag emulator, which has to be connected between the wind turbine under test and the distribution grid. Moreover, this device can cause non negligible perturbations in the power network during switching operations; thus, it requires special agreements with the concerning DSO, which is not always an easy task in some countries.

As certification costs can become relevant in the overall installation expenses, a different approach allowing compliance laboratory tests is a very interesting alternative both for wind power manufacturers and for certification laboratories.

1.2 PURPOSE OF THE THESIS

The object of this work is to develop an innovative approach to the problem of grid code compliance testing of WTs to make the test process easier to be performed and more cost effective. The wind turbine electronic converter can be tested directly in the laboratory, allowing faster and cheaper certification procedures and more repeatable measures. More specifically, this work is oriented toward LVRT compliance testing, as it is the most difficult, expensive and time consuming test to be performed on the field.

This thesis is focused on the development of an all-electronic laboratory test bench emulating WT-based generators, offering the possibility to perform grid code testing directly and completely in the laboratory. The proposed test bench is based on a power hardware in the loop (PHIL) platform modeled to emulate the behavior of a permanent magnet synchronous generator (PMSG) based WT. The advantages of the proposed solution as compared to the traditional on-field testing are the simplification of the certification process that would lead to lower costs, lower testing time and improved testing repeatability.

The structure of this thesis is divided in three main parts, which correspond to the main phases of this work:

- Wind energy sources and grid code standards
- Modeling and simulations

- Design and realization
- Low voltage ride through testing

1.3 THESIS CONTRIBUTIONS

This thesis describes a novel solution to perform wind energy converters (WEC) testing in laboratory, instead of performing it on the field. The WT modeling and laboratory standard certification testing has already been studied in many works. However, the literature seems to be lacking of a test bench intended only to perform standard certification on a WEC. To develop this technology, many studies on WT modeling and methods to perform LVRT test on real WTs has been examined. The major scientific contributions of this thesis are related to the following topics:

- Wind turbine systems typologies. Many WT designs exist, they differ in the turbine geometry and the nacelle internal components, as well as electronic converters and electric generators. As the certification test bench structure is related to the WT type, the identification of the most used WT designs is essential to choose a useful testing technology. Many publications summarize the WT structures over the years, their features, their design approaches and their worldwide WT market trend [1, 7, 8, 40, 51, 71].
- Wind energy converters control strategies. Electronic converters topology and structure varies depending on the WT type. WEC plays a fundamental role in a WT power system, maximizing its efficiency and intervening during emergency situations, as described in [1, 7, 8, 10, 11, 36, 37, 45, 51, 54, 63, 73, 80, 85].
- Analysis of the existing grid code standards. A comparison between international grid code standards is necessary to understand their differences in different countries. The study has been focused on the small-medium power WT and on the LVRT certification aspect. In literature many comparisons of the international grid codes are described in [16–19, 27, 28, 31, 42–44, 57, 61, 68, 70].
- Modelling and simulation of a WT system. To be correctly emulated, a WT must be modeled in all its parts, including the turbine aerodynamics, the pitch angle actuator and controller, the drive train and the generator. The model has been used to implement an all-electronic WT emulator, used to test the WEC. The mathematical representation of the WT parts and the modeling has been reported in several publications [1, 7, 12, 25, 33, 35, 48, 50, 51, 55, 56, 59, 60, 62, 64, 66, 67, 78, 87].
- Analysis of the existing solutions used to perform LVRT certification tests on WTs. This analysis includes a study of existing technologies used to perform

on field WT testing, experimental researches on voltage sag generators and WT laboratory testing, as presented in [4–6, 20, 28, 29, 38, 39, 75, 83].

Part I

WIND ENERGY SOURCES AND GRID CODE STANDARDS

WIND ENERGY SOURCES

2.1 GLOBAL SCENARIO

During the last 15 years, the amount of wind power installations has grown almost exponentially. At the end on 2015 wind power installations was approximately equal to half the global electricity growth [21]. During the last three years the mean average growth of wind power capacity amounted to 55GW per year and, at the end of 2016, its cumulative power production reached a total of 487GW, as shown in Fig. 2.1.

China, USA and Germany are the four major investors in this market, owning together 61.9% of the total wind energy installed capacity, as reported in Fig. 2.2 [22]. China is the nation having the largest wind power installation and the biggest investors. China also has the biggest wind farm in the world in Gansu, capable of 6.8GW power generation.

In Europe the total power capability increased from 41GW, to 154GW, i.e. , 6% to 16.7% of the total energy production, as reported in Fig. 2.3. This means that in 2016 European new wind power capacity has reached the 59.2% of the power production from renewable energy sources, constituting alone the main clean energy production technology, Fig. 2.4.

According to [3], during 2014 global carbon emissions have remained nearly constant despite the economical growth. This happened for the first time in 40 years, due to improved industrial restructuring, energy efficiency and renewable energies growth [21]. It is clear that wind energy is playing a major role in reducing carbon emissions, and will probably be more an more relevant in the next decades. The Global Wind Energy Council expects the cumulative global installation to reach a capacity of 792GW by 2020, that is a 60% growth in only four years.

2.2 WIND ENERGY CONVERSION

Wind energy extraction has a very long history and its first trace is a representation of a sailing boat, been found in Kuwait and dating between 5000 and 5500 BCE [15]. The first mentions of wind energy based machines have been found in Mesopotamia, windmills were used during Hammurabi kingdom in irrigation systems and are dated 1700 B.C. [34]. Ruins of Persian windmills can be found even today in Afghanistan and Iran, and were used in Persia about 500-900 A.D. They were based on a long vertical shaft driven by rectangular blades made of cloth and were used to grind grain to make flour. The first WT used to generate electricity was built in 1887 in Scotland by James

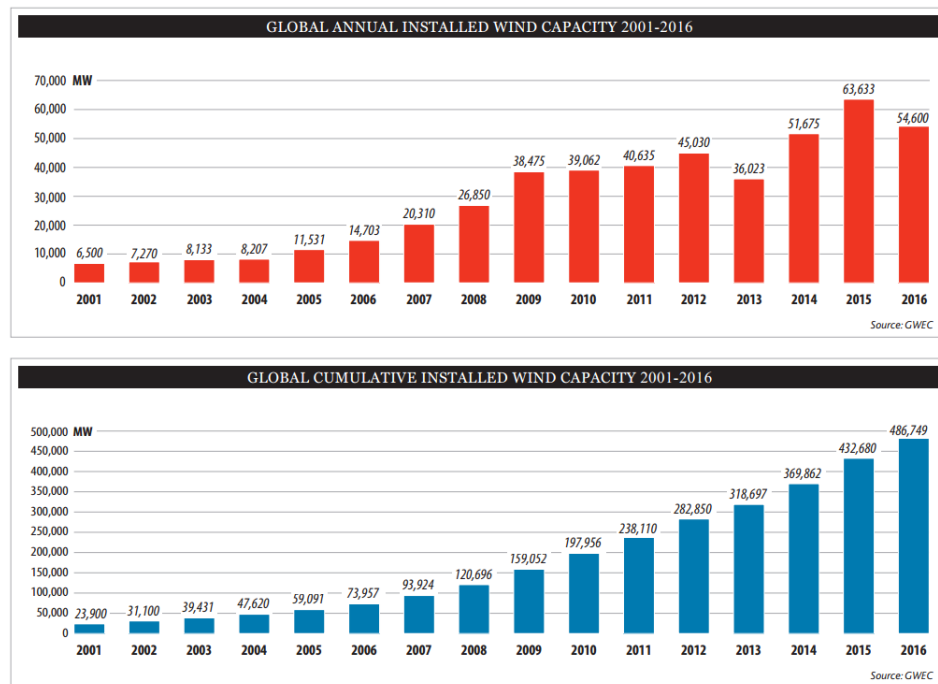


Figure 2.1: Global annual installed wind capacity and global cumulative installed wind capacity from 2001 to 2016 [22]

Blyth, for battery charging applications. Some months later, the first automatic wind turbine was built in Cleveland by Charles F. Brush, it was 18m tall and able to drive a 12kW generator [53].

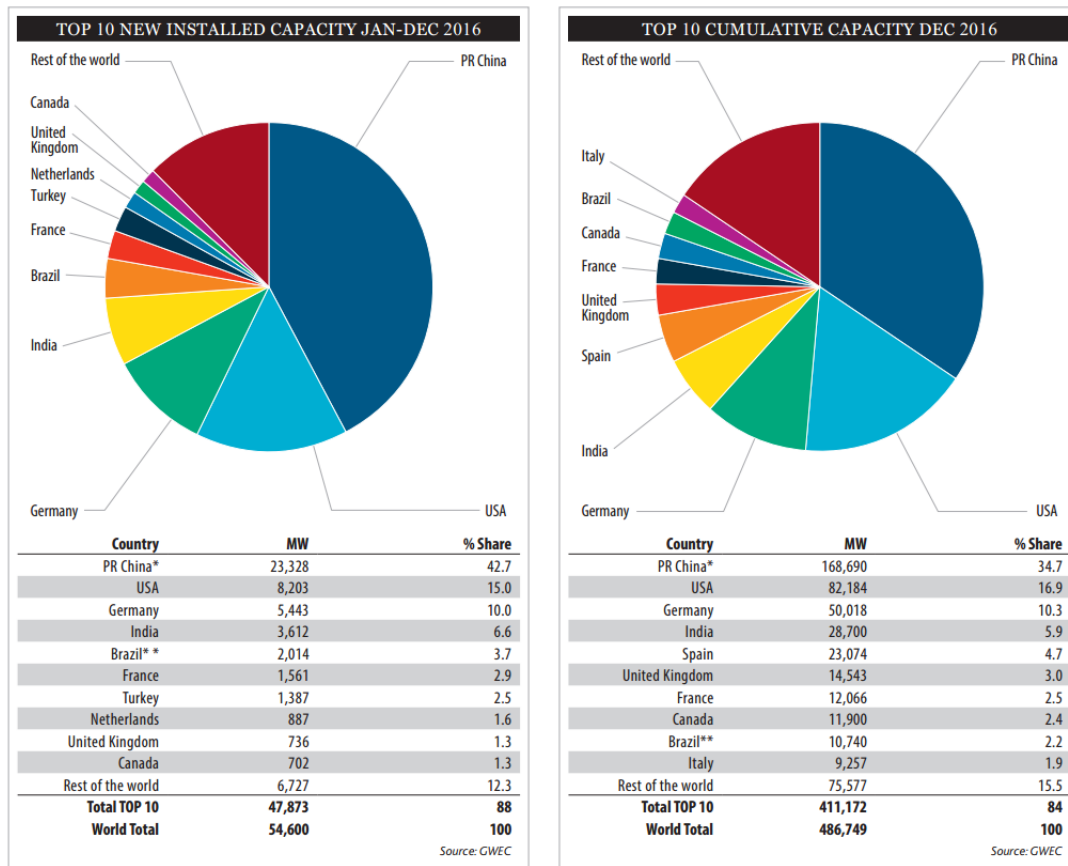
Today one of the most powerful WT is the Vestas V164, which, with a rotor diameter of 164m and a total height of 187m, is able to generate 8.4MW.

In the 1980s wind turbines power capability was about few tenth of kilowatts. Since then, the technologies used to implement wind turbines radically changed: 5 generations of wind turbines have been developed during the years.

As depicted in Fig. 2.4, the structure of a WT system has remained similar though years. It is based on a rotor, a gearbox, a generator, an electronic converter and a power transformer to interface the WT with the distribution grid [8]. The rotor role is to extract power from wind and to convert it in rotating mechanical power. Over the years, various types of rotors has been used. Based on how they spins, they can be divided in two main families:

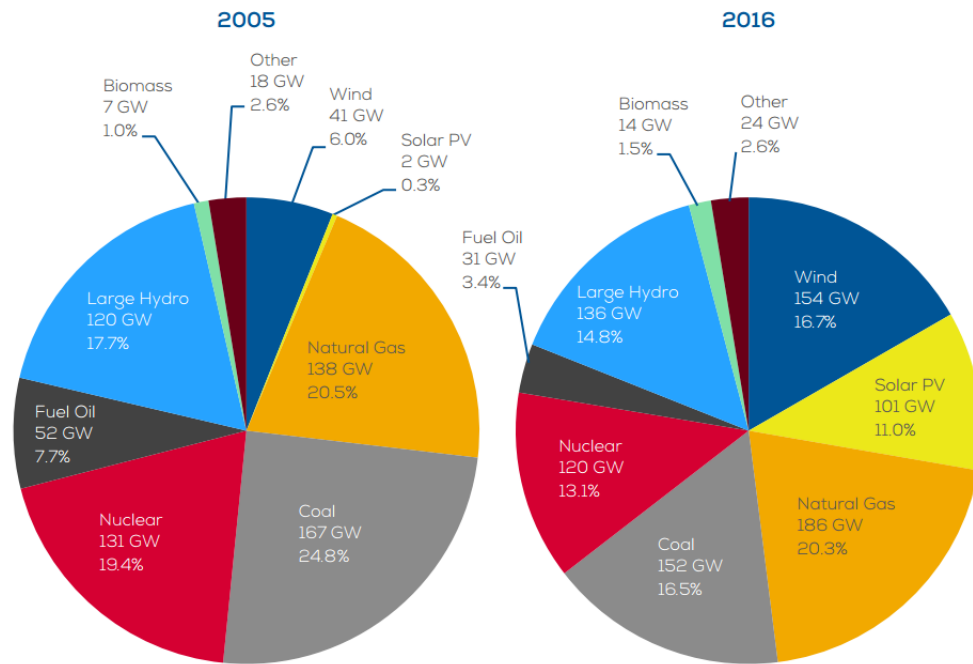
- Vertical axis wind turbine
- Horizontal axis wind turbine.

Vertical axis WTs are based on a vertical rotor shaft in which the main components (i.e gearbox, WEC, generator) are mounted on the base. Compared to the traditional hor-



* Provisional figures
 ** Projects fully commissioned, grid connections pending in some cases

Figure 2.2: Worldwide new and cumulative wind capacity in 2016 [22]



Source: WindEurope

Figure 2.3: European shares in installed capacity in 2005 and 2016 [30]

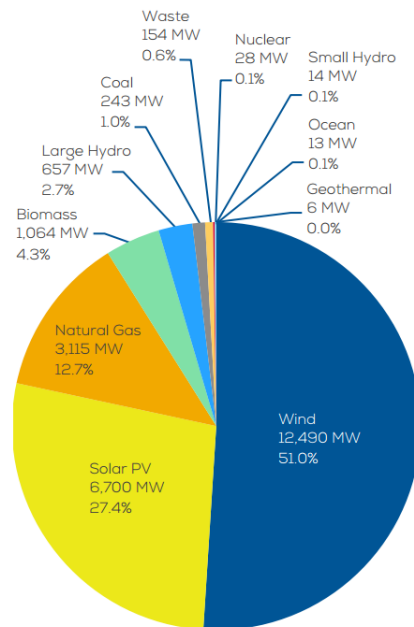


Figure 2.4: European new installed capacity in 2016 [30]

horizontal axis WTs, their structure is less complex to maintain, as the main components are at ground level. Moreover, as the center of gravity is lower, they are more stable in an offshore context. Finally, because of the omni-directionality of the rotor, wind direction tracking is not needed [71].

Horizontal wind turbines are based on a horizontal rotor shaft connected to a generator mounted on the top of a supporting tower. The shaft is connected to a propeller, which must be pointed on the wind direction. Their maintenance is more difficult as all the main components of a horizontal WT are placed at the top of its tower and they are not easy to reach or to be changed when a fault occurs.

The rotor of a horizontal WT can be built with different numbers of blades, allowing different characteristics in terms of rotating speed and operating range. As an example, traditional American windmills use 18 blades based propellers because of their high starting torque. On the contrary, two bladed propellers have a poor starting torque but can operate efficiently on a very high range of rotation speed. Now the vast majority of modern WT are based on three blades propellers, as their aerodynamics allow to reach the higher efficiency in wind power extraction. For this reason only horizontal, three bladed WTs will be considered herein.

A gearbox is used to increment the low rotational speed of the turbine rotor in order to adapt it to the higher nominal speed of the generator. The gearbox sometimes is not necessary, depending on the size of the WT propeller and on the generator type.

The generator is a component needed to convert the mechanical power into electricity and can be realized using different technologies. Depending on the WT typology an electronic converter can be used to adapt the frequency and amplitude of the generator output to the waveform of the distribution grid. The use of an electronic converter allows the wind turbine to work at variable rotational speed. As the maximum efficiency condition of a WT depends on its rotation speed, variable speed WTs are able to track the maximum power point and maximize their power extraction.

A power transformer can be used to adapt the WT output voltage amplitude to the grid when needed. Depending on the WT power rating, the connection to the grid is possible at low, medium and high voltage. Despite the fact that modern wind turbines are usually connected to medium voltage grids, large offshore windfarms are connected to high and extra high voltage grids [8].

When allowed by the grid code standards, between the electronic converter (or the generator if the electronic converter is not present) and the transformer, a circuit breaker is used to disconnect the WT to protect the WT from anomalous grid conditions by disconnecting the WT from the grid.

2.3 WIND TURBINE TYPOLOGIES

Wind turbines, based on their generator type and the presence of an electronic converter, can be divided in two fundamental families:

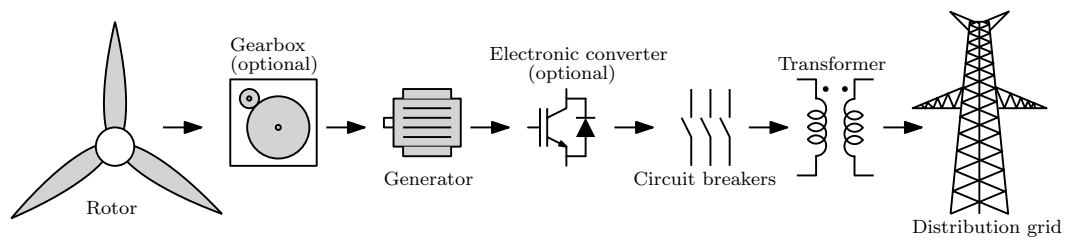


Figure 2.5: Modern WT power system, main components

- Fixed speed wind turbines. Their structure is simpler, but it is also becoming obsolete.
- Variable speed wind turbines. They are based on electronic converters to maximize energy extraction.

2.4 FIXED SPEED WIND TURBINES

The first commercially available WT for grid-tied applications was a fixed speed WT, installed between the late 1970s and the early 1980s. As shown in Fig. 2.6, in a fixed speed wind turbine the generator is directly connected to the grid through a step up transformer to increase the generator output voltage to the grid voltage level. Fixed speed WTs are usually based on an asynchronous squirrel-cage induction generator (IG) in which the rotational speed is determined by the pole pairs and by the grid frequency. In an IG, the rotor speed variation is limited to a small percentage of the nominal speed, namely the IG slip factor, usually less than 5%. Depending on the poles number, a induction generator can rotate at a fixed speed of 1000rpm or 1500rpm [84], a fixed speed WT needs a gearbox to increase the slow rotational speed of the rotor to the generator nominal one. The power extraction is usually limited aerodynamically, i.e., by designing the blades to stall during high wind speed or by actively controlling the blades pitch angle to limit the turbine torque. Fixed speed WT advantages are their simplicity, cost effectiveness and reliability. Even though those characteristics make this technology very attractive, it suffers from multiple drawbacks [8] :

- As it has to operate at constant speed it needs a stiff power grid to ensure stable operation.
- Flicker and power oscillations due to wind turbulence are injected directly into the grid.
- It needs a more expensive mechanical construction to absorb stresses caused by wind gusts.

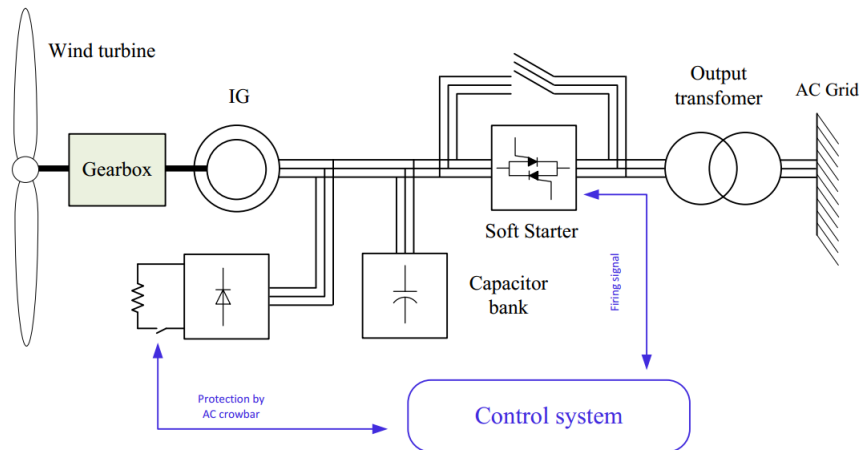


Figure 2.6: Typical fixed speed WT power system [28]

- Its IG causes high inrush currents at connection and disturbances into the grid, experiencing dangerous high torque peaks in the gearbox.
- It needs a reactive power compensator to reduce reactive power.
- Its optimal efficiency is limited to a very narrow wind speed range due to the fixed rotation speed.
- Its power extraction is less efficient as compared to variable speed WTs.

During power grid disturbances, a low voltage sag can cause large fault currents on the induction generator, causing the protection system to activate. As the IG is directly connected to the grid, it is very difficult to design a system fulfilling the grid codes, especially in cases where WT disconnection is not permitted during voltage sags [28]. For all these reasons fixed speed WTs are now almost obsolete.

2.5 VARIABLE SPEED WIND TURBINES

Variable speed WTs rely on an electronic converter to interface the generator to the utility grid. This allows the generator to be independent of the grid frequency and to work in a wide range of rotational speeds. The main advantages of the variable speed WTs over the fixed speed WTs are:

- Simpler pitch control, as the generator can be used to limit the rotor speed.
- Reduced mechanical stresses, as wind gusts can be absorbed in the form of kinetic energy.

- High system efficiency, as the variable speed WT systems can optimize the power extraction for a wide range of wind speeds.
- Standards compliance, as the power converter can be programmed to behave as specified in the grid codes.

Based on the electrical generator, there are many types of variable speed WTs. The most commons can be divided in two main families [8, 40]:

- Doubly fed induction generator (DFIG) based WTs.
- Full scale energy converter (FSEC) Integrated Systems.

2.5.1 *Doubly fed induction generator based WTs*

A typical DFIG based WT system is shown in Fig. 2.7. A DFIG is an induction generator with accessible rotor windings used to generate a variable speed rotating magnetic field. The stator is directly connected to the grid through a step up transformer to increase the output voltage to the grid level. The rotor windings are accessible by slip rings. If the generator is rotating above synchronous speed, the electrical power is injected into the grid by both the stator and the rotor windings. Vice versa, when the generator is rotating below synchronous speed, the electrical power is injected from the grid to the rotor and from the stator to the grid [59].

Using an electronic energy converter to drive the stator currents and controlling their waveform frequency, it is possible to obtain about $\pm 30\%$ speed variation over the generator nominal speed. Additionally, output active and reactive power can be delivered into the grid independently from each other [32].

The main advantage of a DFIG over a full scale energy converter based WT is the reduced inverter costs, as the electronic converter has to process only 20% to 30% of the rated power of the generator. This implies that one third of the total power has to be converted by a WEC to drive the WT in a wide range of rotational speeds. Moreover, the inverter filters and EMI filters are cheaper as compared to those inside a full scale energy converter based WT because of the reduced power rating.

The drawbacks of the DFIG includes the wear of its slip rings, which need maintenance during the years. Moreover, during grid voltage sags, the grid side converter is unable to inject (or absorb) the produced (or needed) power into the grid without exceeding the converter current rating. In this situation, as the excess of energy cannot be delivered to the grid, a resistive crowbar is often used to protect the turbine and the converter [28].

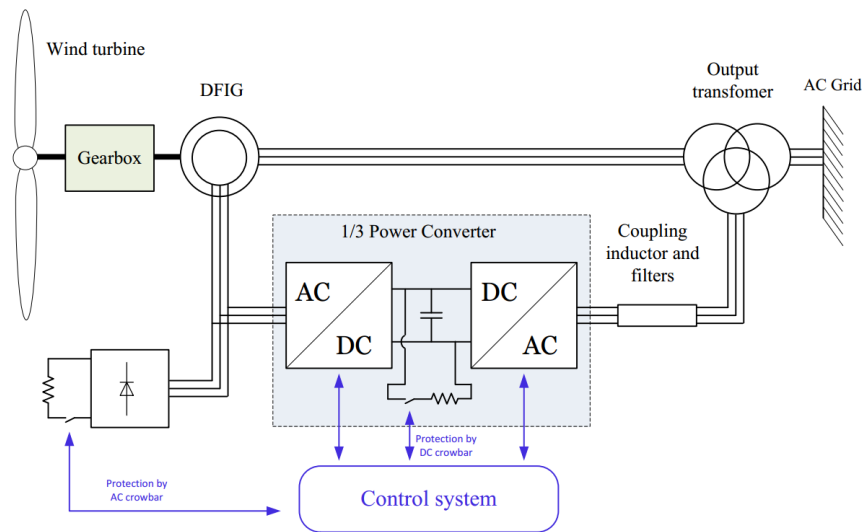


Figure 2.7: Typical doubly fed induction generator based WT system [28]

2.5.2 Full scale energy converter based WT

A full scale energy converter (FSEC) based WT is shown in Fig. 2.8. The system is characterized by the connection of a full scale AC/DC converter between the generator and the step up transformer, adapting the converter output voltage to the power grid amplitude. This solution allows the frequency of the generator output to be completely independent from the power grid.

As the energy converter processes the entire power at the output of the generator, it is considerably more expensive and bulky compared to the DFIG one. FSEC systems can be based on different types of generators:

- Induction generators
- Synchronous generators
- Low speed multi-pole synchronous generators
- Permanent magnet synchronous generators (PMSG)
- Low speed multi-pole permanent magnet synchronous generators

The most used generators in FSEC systems are permanent magnet synchronous generators. More specifically, multi-pole low speed generators allow the rotor to be connected directly to the generator shaft. This solution makes the system more reliable and cheap, as the gearbox is not needed and it is not subject to mechanical wear. Because of these reasons, multi-pole PMSG based WTs are becoming the preferred choice

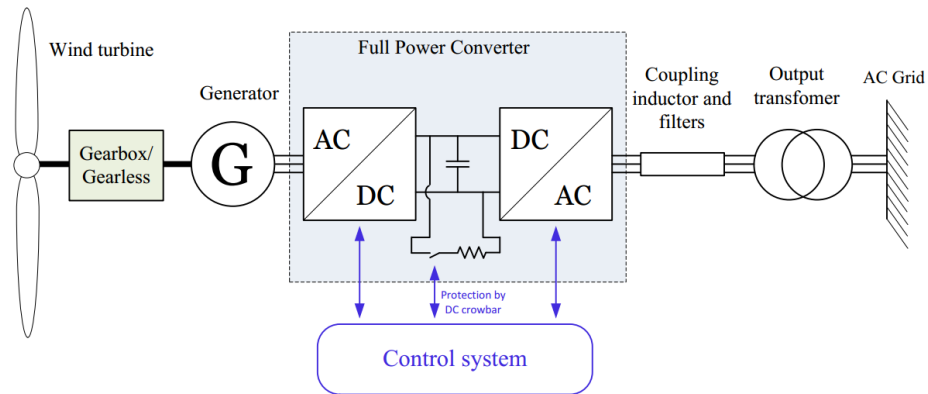


Figure 2.8: Typical full scale power converter based WT system [28]

in cases where maintenance can be a serious issue, as in offshore applications. Moreover, the absence of a gearbox leads to less mechanical friction losses, which improves the overall efficiency .

The FSEC can be easily designed to inject reactive power into the grid as specified by the standards during particular conditions. Moreover, the full scale converter allows great flexibility in the WT behavior, during both normal and abnormal working conditions. For example, during grid voltage sags the grid side currents can be controlled fast enough to prevent any over current to be injected into the grid and so any fault in the grid side converter. In this situation a crowbar is often used to prevent the DC link to overcharge by redirecting the generator excess energy into a resistive load.

GRID CODE STANDARDS

3.1 INTRODUCTION

During the last years the number of distributed generators connected to the power grid has been increasing very rapidly. The large diffusion of renewable energy sources is continuously changing the structure of the medium voltage (MV) and low voltage (LV) distribution grids.

More specifically, the residential scenario has experienced one of the most relevant growth of distributed renewable energy resources. Most of these small-scale generation systems are based on power converters interfacing the energy source and the grid. Their use increases the complexity of network management and operation for the DSO. In this scenario, the increasing distributed energy penetration required the introduction of new technical regulations for the new small to medium power distributed energy sources. The main goal is to increase the flexibility of the grid and to facilitate its growth and integration in the emerging context [65].

The main issues connected to power quality are flickers, power peaks, harmonics, voltage and frequency fluctuations. As the power grid was not originally conceived to be powered by a substantial amount of distributed generators, transmission system operators have been required to update their grid code standards to guarantee a reliable grid behavior. Distributed generators are asked to support the grid and provide useful features to improve the power quality and the stability of the overall network.

These requirements are not the same in every country and vary depending on the DSOs, the grid stiffness and the penetration of renewable sources. However, many of the grid code requirements deal with the following aspects [26, 27, 43]:

- Voltage and frequency operating range
- Active power regulation
- Reactive power regulation
- Flicker
- Low voltage ride through (LVRT)
- Harmonics
- Anti-islanding
- Connection and reconnection conditions

- DC output current
- Over Voltage Ride Through (OVRT)
- Reconnection in phase opposition

Despite this study is focused on LVRT testing, all the other aspects concerning grid code certification can be inspected by performing minor modifications on the test bench that is the object of this work. More specifically, the first four aspects are the most interesting in the WEC testing point of view. For this reason they will be covered more in depth in the following sections. As these aspects often depend on the DSO and national regulations, their requirements will be covered from a general point of view, unless in those cases where practical examples are considered.

Usually the grid codes are referred to the point of common coupling (PCC), the electrical point of connection between the wind farm and the grid or to the point of connection (POC), the electrical point of connection between of the single wind turbine and the power grid.

3.1.1 Voltage and frequency operating range

A power network frequency variation can be used as an index of the power production over the power consumption. If the power consumption becomes higher than the power production, the connected rotating generators will be slowed down and the power network frequency will decrease. Differently, if the power consumption becomes lower than the power production, the excess of energy causes an increase of the rotation speed of the connected generators. This leads to an increase of the the overall power network frequency.

Grid code standards specify the WT to remain connected in a given range of frequencies and voltages amplitudes. As an example, [16] specifies that a WT must be designed to work continuously under normal conditions:

$$\begin{aligned} 90\%U_n &\leq U_{PCC} \leq 110\%U_n \\ 49.9\text{Hz} &\leq f_{PCC} \leq 50.1\text{Hz} \end{aligned}$$

where U_n is the grid nominal voltage, U_{PCC} and f_{PCC} are the voltage and frequency at the PCC. Moreover when the PCC voltage and frequency are:

$$\begin{aligned} 85\%U_n &\leq U_n \leq 110\%U_n \\ 47.5\text{Hz} &\leq f \leq 51.5\text{Hz} \end{aligned}$$

the WT is asked to stay connected modifying the power delivered to the grid according to the standards.

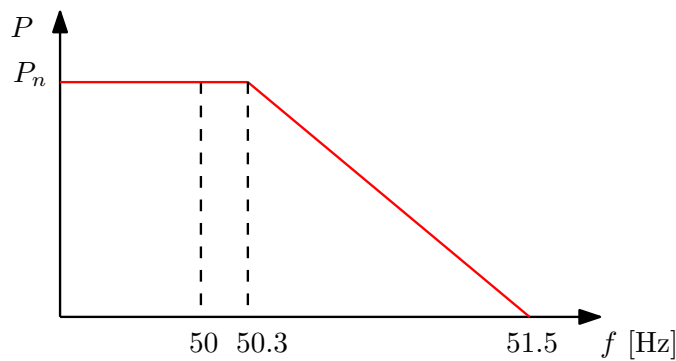


Figure 3.1: Active power regulation P/f curve required by the Italian standards [16, 17]

3.1.2 Active power regulation

As already mentioned in the previous section, frequency deviations are caused by an unbalance between power production and demand. This can happen, for example, when a fault causes a part of the grid to disconnect, causing an overproduction of power leading the grid frequency to increase. On the other side, when a power plant is disconnected from the grid the power demand exceed the power production and the grid frequency decreases.

The ability of a wind turbine to regulate its active power during over frequency situations is very important from the grid stability point of view. For this reason, DSOs require WTs to limit the active power regulation in order to balance the generation and demand. Most grid requirements demand active power curtailment in response to grid frequency deviations.

As an example, the Italian standards CEI 0-16 and CEI 0-21 require full converter based wind turbines to change their active power level accordingly to the droop curve shown in Fig. 3.1, where P_n is the nominal power of the WT.

Moreover the Italian standards specify the WT to gradually increase the active power injection in response to an over-frequency situation. The power increase must follow the P/f curve reported in Fig. 3.1 in the opposite direction, with a gradient of $20\%P_n/\text{min}$.

3.1.3 Reactive Power regulation

The voltage level in a power grid must stay in a given range around the nominal value, as the connected equipment is designed to work inside that range. WTs are usually required to generate or absorb reactive power in order to contribute to the grid voltage level regulation.

The Italian standards CEI 0-16 and CEI 0-21 require full converter based wind turbines to regulate their reactive power injection according to the droop curve shown

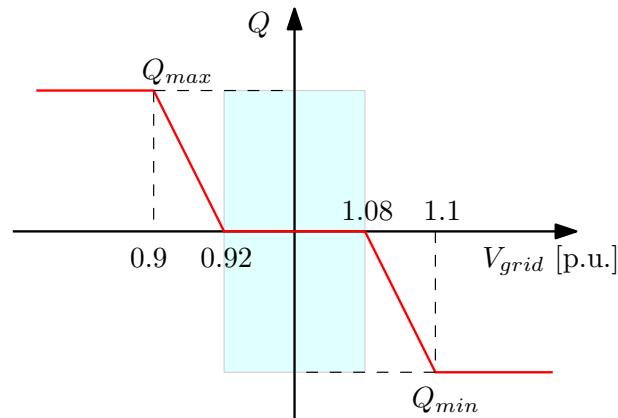


Figure 3.2: Reactive power regulation Q/V curve required by the Italian standards [16, 17]

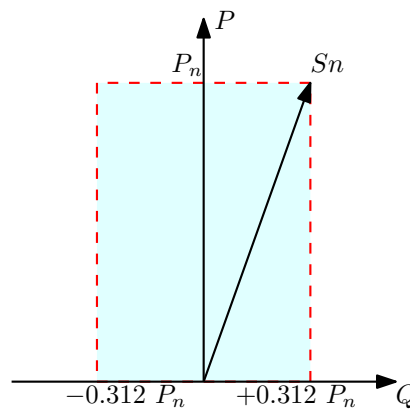


Figure 3.3: Capability of WEC for low voltage grid connection[17]

in Fig. 3.2. In this case the reactive power limits Q_{max} and Q_{min} are based on the imposed capability shown in Fig. 3.3 , where S_n is the apparent power. The effect on the grid line voltages depends on the grid impedance, the grid stiffness and the load connected in the PCC proximity [68].

3.1.4 Flicker

Flicker is a term that refers to the visible unsteadiness of light intensity caused by the supply voltage fluctuation. Flickers are usually caused by changes in the loads or by power fluctuations in the active sources connected to the grid. Flickers can lead to an annoying light perception especially if the flicker frequency is below 20Hz.

In a WT flicker may be caused by the effect of the tower shadow effect, the wind shear, wind turbulences or by a fluctuation in control systems [70]. As an example, the

shadow effect of the tower introduces an aerodynamic disturbance, which translates in a power sag every time one of the rotor blades is aligned with the tower.

For these reasons a three blades WT produces a flicker whose frequency is three times per rotor revolution [57]. This effect causes periodic power fluctuations whose frequency is influenced by the rotor dimensions, as large WTs spin at a lower speed than small WTs, and by the wind speed. The functional and design specifications for a flicker measurement apparatus intended to measure the flicker severity according to the standards are described in [44].

3.1.5 *Current harmonics*

Voltage and current harmonics are always present in the power network and are usually caused by connected equipments like rectifiers, inverters, non linear loads and switches. The standards defines the tolerable harmonics generated by a WT working in steady state.

The current harmonics measure and evaluation methods are described in [42]. This standard defines that harmonics and interharmonics must be measured in subgroups of different frequency ranges and evaluated in percent of the nominal current.

3.1.6 *Low Voltage Ride Through*

The ability of a wind turbine to react and support the grid during a fault is called Low Voltage Ride Throug (LVRT). LVRT is one of the most important aspects in the dynamic control of WTs as it is fundamental for a reliable operation of power networks, especially in areas with high penetration of distributed generation. Faults in the grid can cause voltage sags whose effect can be propagated far away from the fault origin. The duration of those voltage sags is influenced by the protection systems response, which takes time to detect the fault and disconnect the affected part of the grid. A grid voltage sag can cause serious issues in WT control and safety, dependently on the WT type. Usually, in full converter based WTs, it is not possible to inject the nominal power into the grid during a voltage sag as the converter would have to increase its output currents beyond its nominal capability.

In the past, wind generators were allowed to disconnect from the grid during a voltage sag. This situation can lead to grid instability issues since, during voltage sags, all the distributed generators would disconnect, in a cascading effect instead of supporting the grid [61]. Moreover, the loss of power generation can lead to more severe drops in the grid frequency [68]. For these reasons, the new grid codes require WTs to remain connected to the network during and, more importantly, after a fault.

The modern grid codes specify the voltage sag profile in which the WT should stay connected without tripping. Voltage sag profiles are different for every TSO and differ in terms of dip duration, magnitude, time and recovery ramp, as shown in Fig. 3.4.

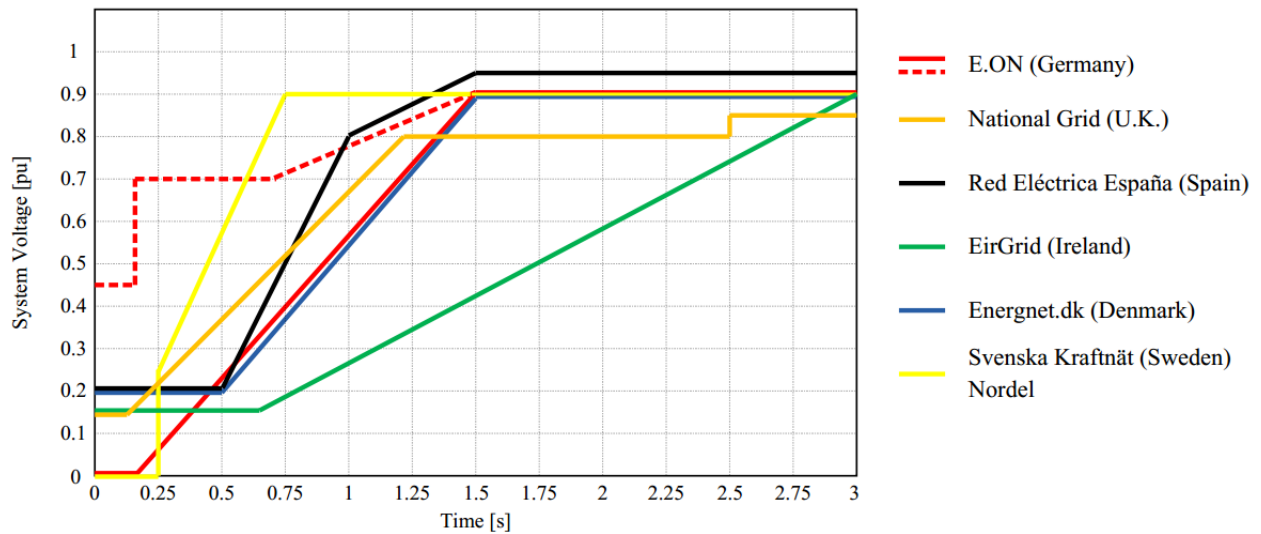


Figure 3.4: Different TSOs LVRT profiles [28]

WTs are asked to tolerate voltage sags of given percentage and duration, disconnection is not allowed if the grid voltage is above the limit line.

Some DSOs additionally require to generate reactive power during the voltage sag to support the grid voltage. As an example [27] specify that wind farms "must support the grid voltage with additional reactive current during a voltage dip" and that "the voltage control must be activated in the event of a voltage dip of more than 10% of the effective value of the generator voltage." Moreover, the amount of reactive current to be injected, depending on the voltage dip amplitude, is specified in Fig. 3.5. Differently, the Italian high voltage grid codes do not currently require reactive current injection during voltage sags [16, 17].

3.2 LOW VOLTAGE RIDE THROUGH CERTIFICATION

Grid code standards require specific test equipment to certify a WT LVRT compliance. For instance, the grid code [43] describes the design specifications for an impedance based voltage sag generator to be connected between the WT under test and the power grid.

The voltage sag generator schematics, shown in Fig. 3.7, is composed of the impedance Z_1 , to limit the short circuit effect on the up-stream grid, and a parallel impedance Z_2 , to generate the voltage sag. The switch S can be implemented by a mechanical circuit breaker or a power electronic device; it is used to connect and disconnect Z_2 during the voltage sag generation and must be able to accurately control the time between connection and disconnection for all of the three phases. Impedance values must be

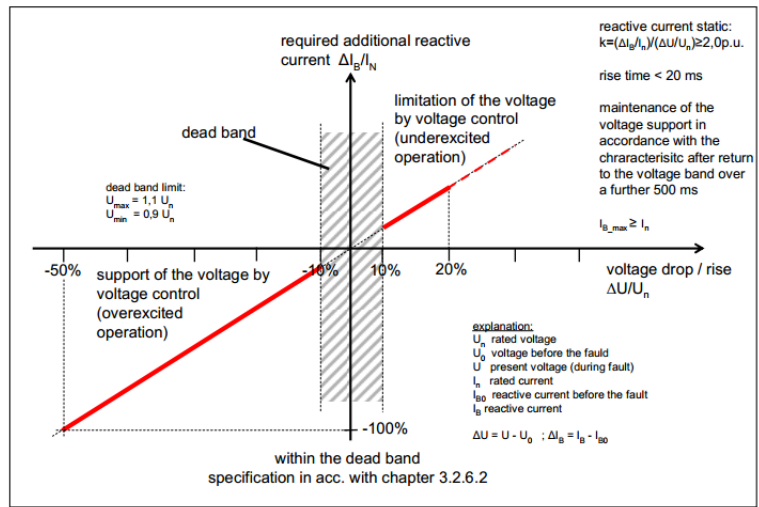


Figure 3.5: Voltage support during grid faults as specified in the EON German grid code [27]

calculated to recreate the voltage amplitudes specified in Fig. 3.6. The same grid codes specify the procedures and the amount of nominal power at which each test must be performed on the field.

As every grid code add specific requirements for the LVRT, the test procedures and requirements can differ from region to region [28, 46, 58, 68, 82]. For instance, some grid codes specify the measurement point should be the PCC, while others the generator terminals POC, some require symmetrical voltage sag testing, others symmetrical and asymmetrical [4]. For these reasons the LVRT compliance testing is closely related to the power network region and its DSOs.

According to [83], sag generators can be obtained using four different approaches:

- Impedance based voltage sag emulator
- Generator based voltage sag emulator
- Transformer based voltage sag emulator
- Full converter based voltage sag emulator

3.2.1 Impedance based voltage sag emulator

The impedance based voltage sag emulator is the one mentioned in the previous section, specified in [43] and depicted in Fig. 3.7. Its principle relies on Z_2 creating a voltage divider together with Z_1 when S is closed. The amount of voltage sag can be set by changing the impedance value. As the switch commutation produces unwanted

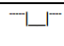

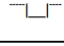
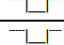
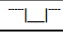
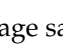
Case	Magnitude of voltage phase to phase (fraction of voltage immediately before the drop occurs)	Magnitude of positive sequence voltage (fraction of voltage immediately before the drop occurs)	Duration (s)	Shape
VD1 – symmetrical three-phase voltage drop	$0,90 \pm 0,05$	$0,90 \pm 0,05$	$0,5 \pm 0,02$	
VD2 – symmetrical three-phase voltage drop	$0,50 \pm 0,05$	$0,50 \pm 0,05$	$0,5 \pm 0,02$	
VD3 – symmetrical three-phase voltage drop	$0,20 \pm 0,05$	$0,20 \pm 0,05$	$0,2 \pm 0,02$	
VD4 – two-phase voltage drop	$0,90 \pm 0,05$	$0,95 \pm 0,05$	$0,5 \pm 0,02$	
VD5 – two-phase voltage drop	$0,50 \pm 0,05$	$0,75 \pm 0,05$	$0,5 \pm 0,02$	
VD6 – two-phase voltage drop	$0,20 \pm 0,05$	$0,60 \pm 0,05$	$0,2 \pm 0,02$	

Figure 3.6: Specification of voltage drops occurring at the WT side of the voltage sag generator, when the WT is not connected [43]

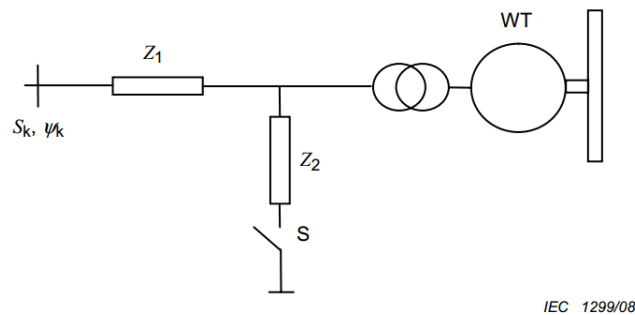


Figure 3.7: Impedance based voltage sag specified by the IEC61400 standard, to test the WT response to temporary voltage drops [43]

harmonic disturbances, this method requires additional filtering. Moreover, the switch commutation delay is unpredictable and cannot be controlled precisely.

The design of the impedance based voltage sag generator is very simple and robust, as it depends mainly on passive components. The main drawback is the impossibility of generating voltage recovery ramps replicating the standards LVRT voltage profiles; in fact it is only possible to change voltage levels in steps. In [4] a 2MW impedance based voltage sag emulator has been designed and built. The final realization has been assembled in a container to be easier to be transported on the field, where tests on WTs must be performed. Despite of that, the impedance based voltage sag emulator is still significantly difficult to transport as the container can be very bulky, especially for high power levels.

3.2.2 Generator based voltage sag emulator

Generator based voltage sag emulators rely on modified diesel generators. The excitation field of the synchronous generator can be directly controlled to produce the

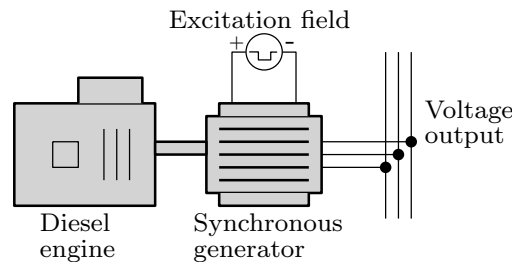


Figure 3.8: Diesel generator based voltage sag emulator

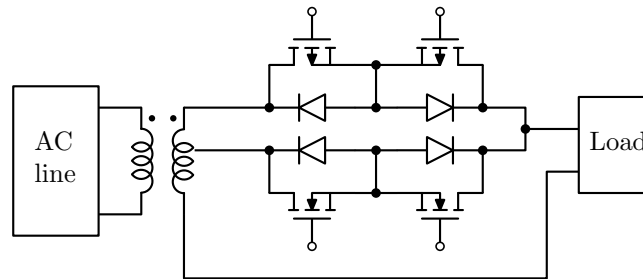


Figure 3.9: One phase equivalent schematic of transformer based voltage sag emulator

needed voltage sag on the synchronous generator output. Moreover, this system can reproduce voltage sags whose decrease in voltage amplitude is relatively slow, as stated in [20], where a 15kW generator has been used. Additionally, this system can only generate symmetrical voltage sags, so it is not suitable to generate asymmetrical voltage sags. For those reasons generator based voltage sag emulators are not the best solution to implement voltage sag generators. A simplified schematic of the generator based voltage sag emulator is shown in Fig.3.8.

3.2.3 Transformer based voltage sag emulator

A transformer based voltage sag generator is based on a multi output transformer to change the secondary voltage level. The voltage dip is generated by connecting the device under test to a different transformer output with a smaller primary to secondary turn-ratio. Using different turn-ratios it is possible to adapt the voltage sag level to many different amplitudes. In this setup the switches must be bidirectional, to allow the current flow in both directions. In [83] a 30kW transformer based voltage sag generator has been built by using IGBT switches and a variable output transformer with five different levels of voltage adjustments. A simplified, one-phase, equivalent schematic of the transformer based voltage sag emulator is shown in Fig. 3.9.

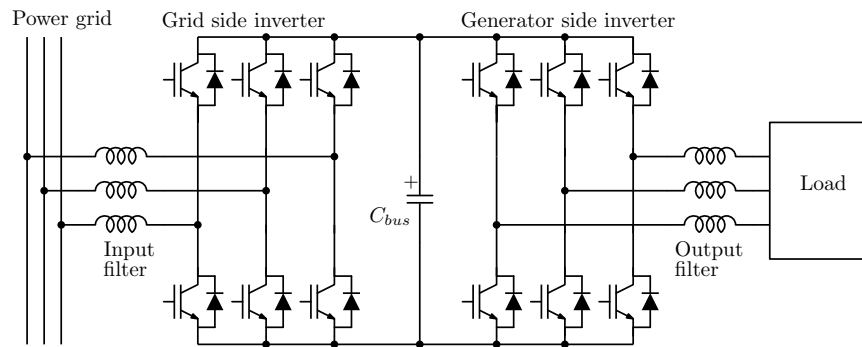


Figure 3.10: Full scale back-to-back converter simplified schematic

3.2.4 Full converter based voltage sag emulator

The most flexible solution to implement a voltage sag emulator is by using a full scale power converter. In this setup a back-to-back electronic converter is connected between the grid and the WT under test. The back-to-back converter is based on two bidirectional inverters. The grid side one acts like a three phase current generator injecting (or absorbing) current into the grid, the WT side one act as a voltage source. The grid side inverter output voltages are modulated to generate voltage sags. A simplified schematic depicting a typical implementation of a back-to-back full converter is shown in Fig. 3.10.

By properly programming the microcontroller driving the WT side converter any kind of grid fault can be emulated. As the grid side is completely decoupled from the WT side, the electric properties seen from the WT are not dependent on the grid. This means that the grid strength is not an issue when using a full converter based voltage sag generator, as long as its power rating is higher than the required one. Additionally the WT side controller can be programmed to implement all the LVRT voltage profiles described by the standards, including the recovery ramp [29]. This system is so flexible that countless network scenarios can be reproduced and emulated: frequency deviations, phase jumps, grid electrical characteristics and impedance, distorted or harmonic addition grid voltages, flickers, overvoltages and so on. The main drawback of a full converter based voltage sag emulator is its cost and complexity, definitely larger than the previously presented emulators [28].

3.2.5 Grid emulator

Besides the fact this work is focused mainly on LVRT testing certification, other power quality tests can be performed on a WEC using the WT emulator and a grid emulator. For this purpose the grid emulator must be able to vary both the emulated grid line frequency and voltages abruptly and with continuity, allowing to reproduce the

abnormal grid situations specified in the standards. The system should also be able to reproduce anomalies like overfrequencies and underfrequencies, overvoltages and undervoltages, both gradually or abruptly. A complete grid emulation system should be able to emulate network impedances as well. This feature allows to reproduce the effects of a WT on the point of connection, if the grid impedance is known. Moreover, the grid emulator should be able to reproduce grid unbalances, needed to perform asymmetric LVRT tests. The only suitable solution to implement an advanced grid emulator able to perform all these tasks, is an electronic power converter. Its advantageous features allow to implement different behaviors, as reported in [13, 23, 28].

3.2.6 *Quality certification test*

Through minor modifications on the WT real time emulator, other additional quality tests can be performed on a WEC using the test bench object of this thesis. The following list briefly illustrates the versatility of the proposed test bench to perform some of the certification tests described in the Italian standards [16, 17]:

- Voltage and frequency operating range. The grid emulator can be programmed to modify the emulated grid voltage and frequency to inspect the WEC operating range. The WEC protection interface system voltage and frequency thresholds and its intervention times can so be compared to the requirements included in the certification standards [17].
- Active power regulation. The WEC behavior during frequency deviations can be inspected by just programming the grid emulator to reproduce those situations. For example, to perform power quality tests in overfrequency conditions, the WEC active power injection can be monitored while the emulated grid frequency increases over its nominal value. In this situation the WEC injecting active power should follow the curve depicted in Fig. 3.1, accordingly to the Italian standards [16, 17].
- Reactive Power regulation. The grid emulator can be programmed to reproduce an overvoltage or undervoltage anomaly on the power network. In this situation the WEC is supposed to modify its injected reactive power accordingly to the curves shown in Fig. 3.2 and Fig. 3.3. If these conditions are met, the WEC complies to the standards requirements regarding reactive power regulation [16, 17].
- Flicker. The WT emulator can be programmed to reproduce the mechanical power fluctuations caused by the effect of the tower shadow and wind shear on the WT. The effect of the tower shadow can be reproduced by periodically reducing the equivalent wind speed and so the power extracted by the wind turbine. In a three blade WT this happens three times per rotor revolution.

The effect of the wind shear can be reproduced by increasing the equivalent wind speed three times per rotor revolution, in phase opposition with the tower shadow effect. This phenomena can be described including their effects on the mathematical description of the wind speed model, as reported in [24, 72, 81].

Although in principle the WT emulator can be upgraded to simulate the wind power fluctuation, it is very difficult to quantify the model correctly as the aerodynamics taking part in the phenomena are highly non linear and depend on the WT geometry, shape and dimension.

Through similar methodologies other tests can be performed on the WEC under test. As an example the following certification tests can be executed on the test bench:

- Harmonics
- Anti-islanding
- Connection and reconnection conditions
- DC output current
- Over Voltage Ride Through (OVRT)
- Reconnection in phase opposition

3.3 STATE OF THE ART ON WIND TURBINE EMULATORS

The state of the art analysis revealed that studies on WT LVRT alternative testing procedures have already been attempted, especially at academic level. In Chalmers university, a back-to-back converter based voltage sag generator has been used to perform WT standard compliance tests [28, 29]. In this study the bidirectional converter, placed near a real WT, has been programmed to generate voltage sags of different durations and shapes. This application is a very versatile and flexible solution, compared to the traditional impedance based voltage sag emulator, allowing for instance the generation of variable amplitude voltage sag. In [28] LVRT tests have been performed on a 4MW wind turbine by using a 8MW back-to-back HVDC station placed in the harbour of Goutenburg, Sweden. This interesting solution is limited by the need of bringing a high power converter on the field, implying all the drawbacks of a conventional on field certification procedure.

Another approach has been studied in the RWTH institute in Aachen university [39], where a WT test bench based on a real-time simulator controlled motor has been designed and developed. The electrical machine is driven by an hardware-in-the-loop (HIL) platform programmed to emulate the mechanical and aerodynamic behavior of the WT rotor. As the revolution speed of a WT rotor is too low and its torque too high

to be reproduced by a conventional motor, the prime mover has to be realized either by using a low speed multi-pole direct drive machine or by a motor-gearbox combination to reduce revolution speed and increase torque. In this test bench the emulated rotor is connected mechanically to the WT nacelle under test.

As stated in [38], a set of 106 sensors has been placed in a 850kW Vestas WT nacelle to monitor electrical values, temperatures, displacements, accelerations, speeds and forces, allowing a complete behavioral monitoring. In the same setup the grid emulator has been realized by using power electronics converters implementing voltage sources. Moreover, the power produced by the WT generator is injected into the grid and reused to supply the motor driver. Thus, only system losses need to be supplied by the external power network during tests [39]. The first realized test bench can be used to test WT nacelles with nominal power up to 1MW. A second test bench, shown in Fig. 3.12 has been developed to reach a nominal power capability of 4MW [6]. The 4MW test bench schematic is shown in Fig. 3.11. This is a complete solution to perform very detailed and in-depth tests on real WT nacelles, however, it requires the realization of a very complex, expensive and bulky test bench.

The high cost of this solution is due to the mechanical realization, the building structural reinforcement, the electronics and the electromechanical parts. The test bench realization cost is definitely out of reach for a common certification laboratory.

The test bench proposed in this work enables the substitution of the electromechanical parts composing a WT with an electronic power supply. The block diagram test bench is shown in Fig. 3.13. This approach is not intended to test the mechanical and electromechanical parts of a WT; therefore it is less complete as compared to the Aachen test bench and can only be used to test wind energy converters. On the other side this solution is less complex, easier to built, more versatile and cheaper, making it a great solution to be adopted in certification laboratories.

This approach enables to perform certification tests of WECs in predictable, controlled and repeatable conditions: wind speed, emulated grid conditions and power extraction are completely under control. The ability to perform LVRT certifications directly into laboratory can theoretically solve all the on field tests issues, in controllable and predictable testing conditions, allowing the test procedure to be easier, quicker and less expensive. This approach is possible only if the WT converter power rating is smaller than the emulator power supply one.

Additionally the test bench relies on a back-to-back power converter to implement the voltage sag generator needed to test the WT converter LVRT compliance. Again, this is possible only if the nominal power of the WT converter under test is smaller than the voltage sag emulator one. For those reasons, the test bench in this study is focused on small to medium power WT wind energy converters certification tests.

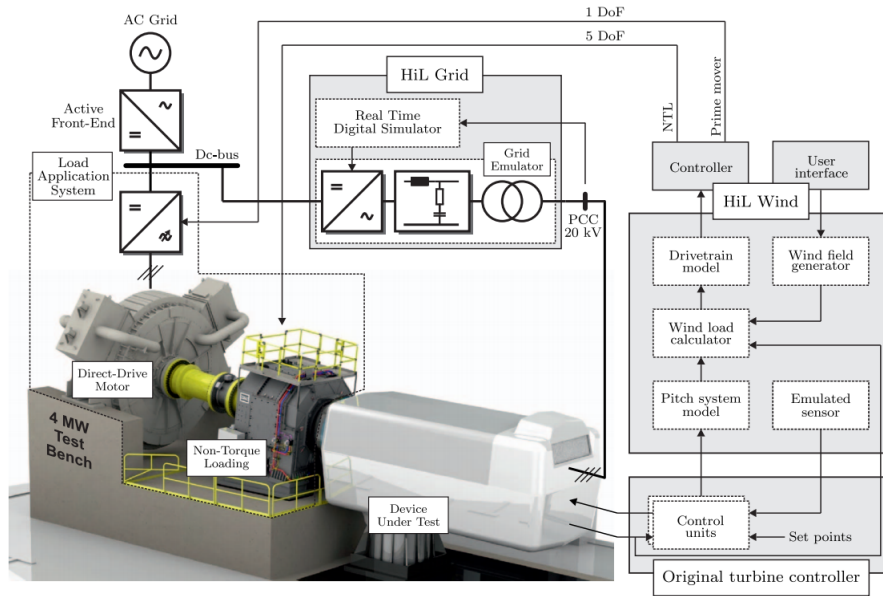


Figure 3.11: Aachen 4MW WT nacelle test bench schematic

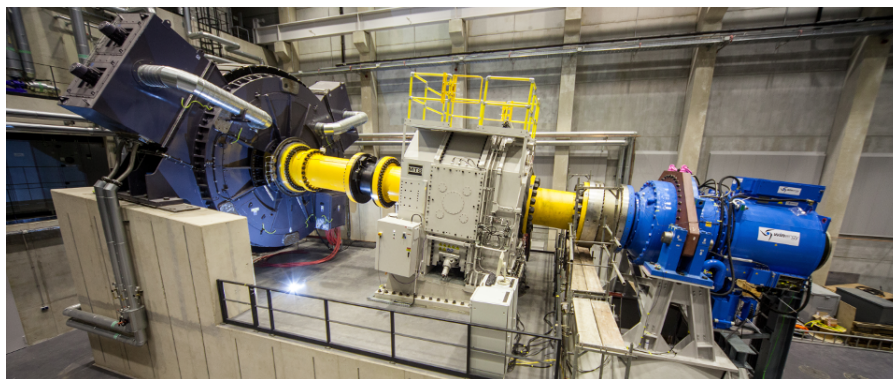


Figure 3.12: Aachen 4MW WT test bench realization

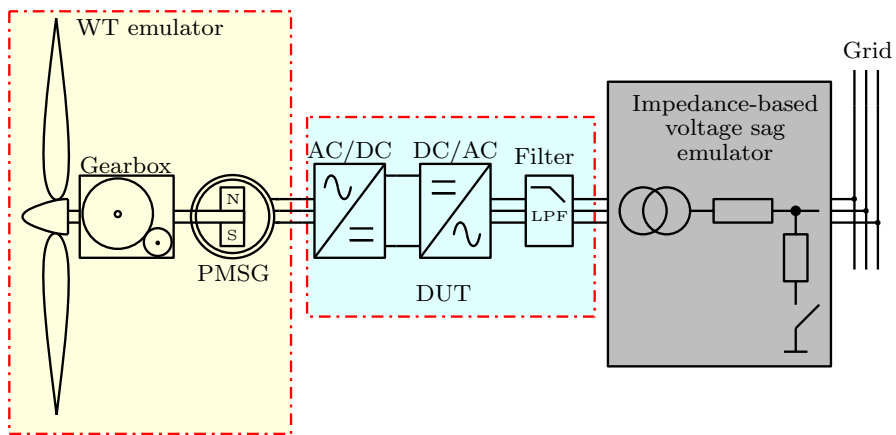


Figure 3.13: Proposed test bench block diagram

Part II

MODELING AND SIMULATIONS

WIND TURBINE MODEL

4.1 INTRODUCTION

In order to realize a faithful emulation of a WT, every component composing the system must be mathematically modeled in detail and correctly interconnected.

As shown in Fig. 4.1, the aspects needed to be considered to obtain an accurate WT emulation are:

- Wind
- Rotor
- Pitch angle controller
- Drive train
- Generator

4.1.1 *Wind*

Wind is a complex physical phenomenon depending on a multitude of factors. It is mainly caused by the temperature gradient between the poles and equator and the rotation of the planet. As its behavior is highly chaotic, a model of the wind can be obtained by describing the wind kinetic energy as an aleatory variable having the Van

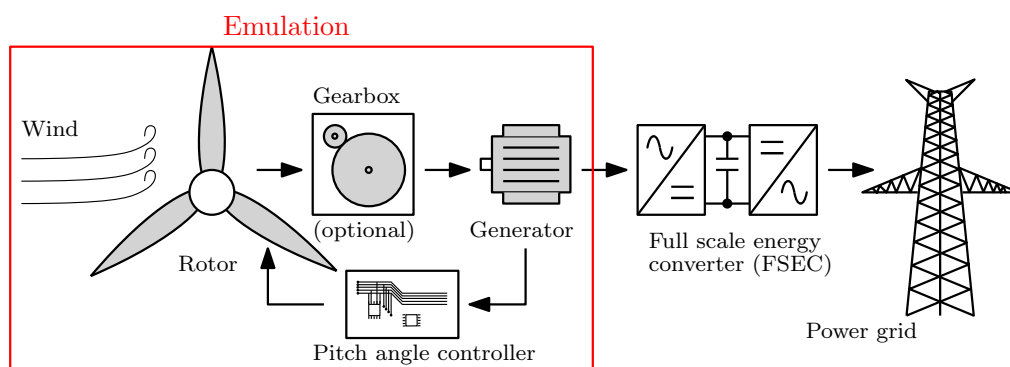


Figure 4.1: Typical structure in a modern WT

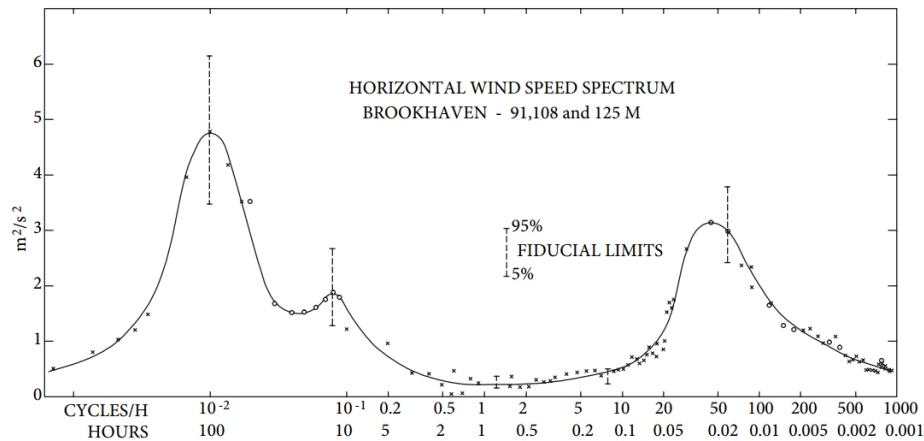


Figure 4.2: Van der Hoven spectrum [49, 79]

Der Hoven power spectrum [79]. The Van Der Hoven spectrum is a description of the frequencies composing the wind speed variability. The Van Der Hoven spectrum, shown in Fig.4.2, presents peaks corresponding to turbulences and synoptic effects, as recorded in Brookhaven, NY, USA in 1957 [49].

As LVRT certification usually requires the tests to be performed at a fixed wind speed, the wind turbine emulator does not require a statistical representation of the wind speed. For example, in [17] and [43] the LVRT tests are required to be performed between 10% and 30% and between 90% and 100% of the WT nominal power. As the standards specify only two ranges of wind speed, its variability does not need to be modeled statistically. Therefore, the wind speed is considered a fixed variable in the implemented model.

4.1.2 Rotor

The rotor is the spinning propeller converting part of the kinetic energy of the wind into mechanical energy. As modern WT designs are most of the times based on three blades horizontal axis rotors, the model here implemented focuses on this typology. Rotor blades rely on the aerodynamic lift force acting along the blades when the turbine is spinning to develop mechanical torque.

As shown in Fig. 4.3, the two main forces acting on a blade airfoil are the drag force f_d , whose direction is opposite to the blade rotation direction v_p , and the lift force f_l , whose direction is always perpendicular to the apparent wind direction v_a . The lift

force f_l depends on the apparent wind speed, that is a combination of the wind speed and the peripheral speed v_p :

$$\begin{aligned} v_p &= R \cdot \omega_{wt} \\ v_a &= \sqrt{v^2 + v_p^2} \end{aligned} \quad (4.1)$$

where ω_{wt} is the rotor angular speed, v is the wind speed and R is the rotor radius.

The force f_r , responsible for the turbine rotation, results from the projection of the lift force f_l on the rotor axis. Its magnitude depends both on the lift force intensity and on the angle of attack ϕ , given by the angular difference between the blade peripheral speed v_p and the wind speed v direction. For these reasons, the turbine generated torque depends both on the wind speed and on the rotation speed. Given P_w , the power of a tube shaped stream of air with cross sectional area equal to the rotor swept area, and P_{WT} , the mechanical power extracted by the WT rotor. The C_p coefficient, called power coefficient is defined as:

$$C_p = \frac{P_w}{P_{wt}} \quad (4.2)$$

Its maximum value, known as Betz limit [1, 7, 51], given by 4.3, which represents a theoretical boundary archived with zero mechanical losses. C_p depends heavily on the rotor realization and its efficiency.

$$C_{pmax} = \frac{16}{27} = 59.3\% \quad (4.3)$$

Usually C_p is expressed as a function of the tip speed ratio λ , i.e. , the ratio between the blade tip peripheral speed and the wind speed:

$$\lambda = \frac{\omega_{wt} \cdot R}{v_w} \quad (4.4)$$

where ω_{wt} is the turbine rotation speed.

Fig. 4.4 shows the power coefficient curves of different WT typologies, expressed as a function of their tip speed ratio λ . The most efficient WT is the three blades rotor WT as it provides a power coefficient C_p up to 48%. By observing Fig. 4.4, it is also possible to note that there is only a value λ_{max} that maximize C_p . This means that for every wind speed there is only a rotation speed maximizing the power coefficient C_p , or, in other words, for every rotation speed there is only a wind speed value maximizing the power extraction. This is the reason why fixed speed WT are less efficient than their variable counterparts; in fact for a fixed rotation speed there is only a wind speed maximizing the power extraction efficiency.

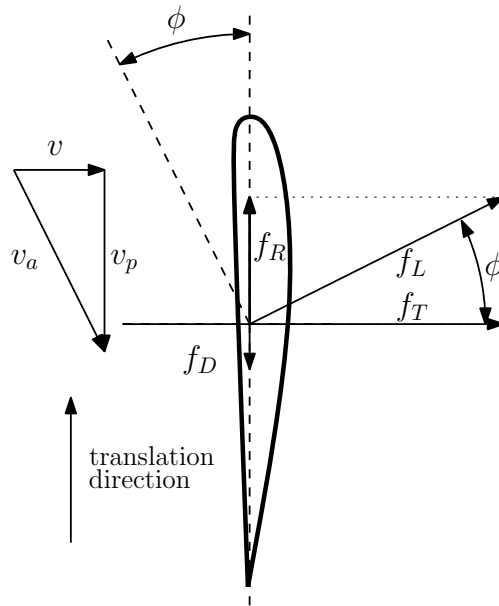


Figure 4.3: Aerodynamic forces on a rotating blade

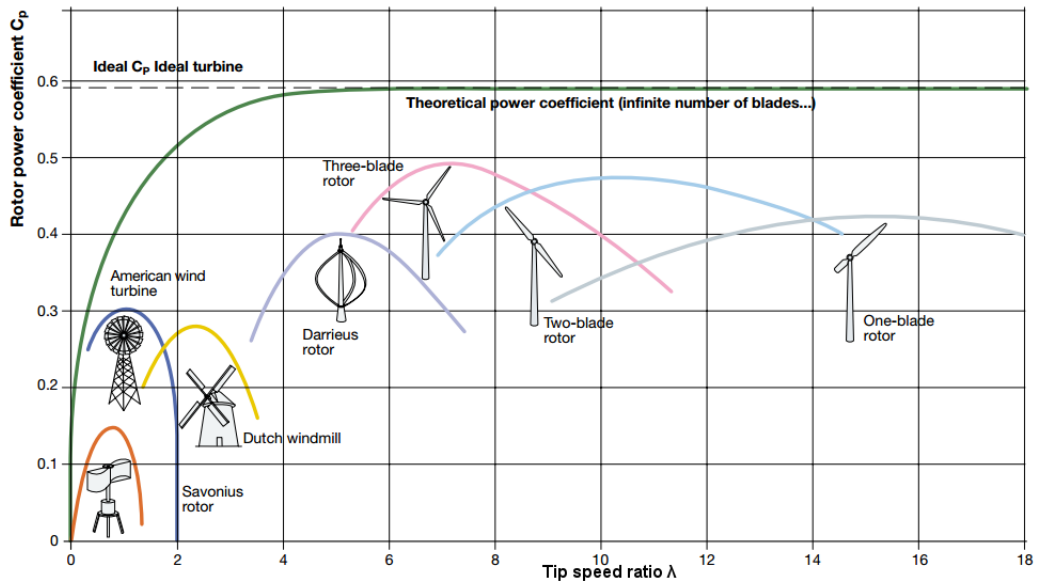


Figure 4.4: Power coefficient for different rotor typologies [1]

4.1.3 Pitch angle controller

The pitch angle controller is the system regulating the rotor blades pitch angle. A pitch angle controller usually monitors the turbine rotation speed and acceleration and it is often used to limit the turbine speed or torque in specific situations. For example, in high wind speed conditions the rotation speed of the turbine can exceed its nominal value. In those conditions, if the WEC is already converting power at its nominal value, the only way to limit the rotor speed by using a mechanical or electric brake or by increasing the turbine blades pitch angle. An increase in the pitch angle will limit the rotor torque and its speed will decrease.

Pitch angle controllers can be used to monitor and control the rotor torque, power and rotation speed by driving the blades pitch angle. In the past, pitch angle controllers were mechanically made by a rudimentary counterweights rotating the blade axis proportionally with the turbine rotation speed. Today, most of the rotors rely on electric or hydraulic drives to turn the blades on their axis and on digital processors to implement a more advanced control system.

4.1.4 Gearbox

Gearboxes are used to adapt the rotor low rotational speed to the higher generator speed needed to convert energy efficiently. According to [1], the drive train system can be divided in three main groups:

- High speed conversion
- Medium speed conversion
- Low speed conversion

In a high speed conversion system, the the gearbox is used to increase the low rotor speed to a high speed, up to 2000rpm [1]. This allows to use lightweight and cheaper generators, but it also implies the use of bulky three stages gearboxes.

In medium speed conversion systems, the gearbox is often implemented in a one or two stage structure and it is used to increase the low rotor speed up to 500rpm [1]. In these systems, mechanical losses and mechanical stresses are smaller than in a systems operating at higher speeds.

Slow speed conversion systems are based on direct drive generators, usually PMSG. These multi pole generators can work with low rotation speed, up to 30rpm, allowing the direct connection of the rotor to the generator [1]. This solution is the more reliable and efficient, as gearboxes are not required.

4.1.5 Generator

Traditionally, WTs rely on the following generators families [8, 28, 85]:

- Squirrel cage induction generators (SCIGs)
- Doubly fed induction generators (DFIGs)
- Wound rotor synchronous generators (WRSGs)
- Permanent magnet synchronous generators (PMSGs)

Induction generators need to be connected to the grid voltages to magnetize the rotor and their rotation speed is linked to the grid frequency. The SCIGs are usually very robust but can only be used to built fixed speed WTs.

DFIGs are induction generators in which the rotor windings are accessible. The rotor magnetic field can be modulated and its rotation speed controlled to obtain a variable speed generator. A DFIG needs a WEC to process only one third of the total extracted power to drive the rotor windings, so the converter nominal power and cost is limited. As DFIGs relies on brushes and slip rings to access to the rotor, they require more maintenance than the SCIGs, thus, over the years, DFIGs are more expensive and less reliable.

In synchronous generators the output voltages amplitude and frequency are proportional to the rotation speed. For this reason they can be used only if a WEC is connected between the generator and the power grid. As the WEC must process the entire generator power it is more expensive than its DFIG counterpart.

In WRSGs, the rotor windings are accessible and can be powered independently of the stator. By controlling the stator current magnitude it is possible to change the generator electromagnetic torque and extracted power. As WRSGs use slip rings and brushes to power the rotor they wear over time and need maintenance.

PMSGs, on the other side, do not require slip rings or brushes, because their rotor magnetic field is generated by a permanent magnet. For this reason PMSGs are more reliable and need less maintenance. PMSGs can also be designed upon multiple interconnected poles to increase the output generator frequency and efficiency. This is useful to realize direct-drive low-speed multi pole PMSGs, which can be connected directly to the rotor without requiring a gearbox. PMSGs are expensive because of the rare earth materials used to manufacture the permanent magnet, even if their price dropped in the last years. On the other hand, the higher cost is usually balanced by the lower maintenance costs and the absence of gearboxes.

The most used WT generator over the last 10 years are the DFIG. In 2015, most of the WTs with nominal power below 2MW used the DFIG technology, however, DFIGs are losing market shares in higher power WTs. In WTs with nominal power between 2MW and 3MW, for example, the direct-drive PMSGs and WRSGs represents the 10%

and the 35%, respectively, of the market shares while DFIG represents the 45%. In WTs above 3MW the medium speed geared PMSGs are the most used solution [40].

Generally, the use of full converters and synchronous generators is gaining market shares over the DFIG generator based WTs [73, 85]. Although the emulation proposed in this thesis is focused on PMSGs, the same methodology can be extended to test DFIG WECs, by introducing in the test-bench a second controllable power supply that emulates the generator rotor electrical behavior.

4.2 MODELS

The software behavioral emulation of machinery parts to be physically integrated in a real system is often referred as hardware in the loop (HIL). The purpose is the connection of physical hardware to a digital emulator running modeled parts of a larger system. By means of this experimental setup it is possible to do measures, run debugging sessions or functional tests on the physical part under test. This solution is very useful in a multitude of situations where it is simpler, faster or cheaper to test individually the single parts of a larger system.

In this specific case, as shown in Fig. 4.5, the simulator models most of the electro-mechanical parts of a WT. The emulator outputs represent the voltage waveforms of a PMSG. As the emulator digital output has to be converted in an analog electrical signal to be able to drive the controlled power supply, a digital to analog converter (DAC) and a conditioning circuit are needed in between. Moreover, the simulator needs as inputs the wind speed and the electric currents absorbed by the WEC under test. These physical currents must be measured and converted in digital domain to be fed to the real time simulator by using current sensors, conditioning circuits and analog to digital converters (ADCs).

The WT modeling is aimed to obtain a mathematical representation of every WT component. This allows to run complete simulations of the entire WT system connected to the grid. The model will be first validated by running computer simulations based on Matlab Simulink. To obtain a complete and coherent simulation of the entire WT system the following components need to be modeled:

- Rotor
- Pitch angle controller
- Gearbox
- Generator
- Energy converter
- Power grid

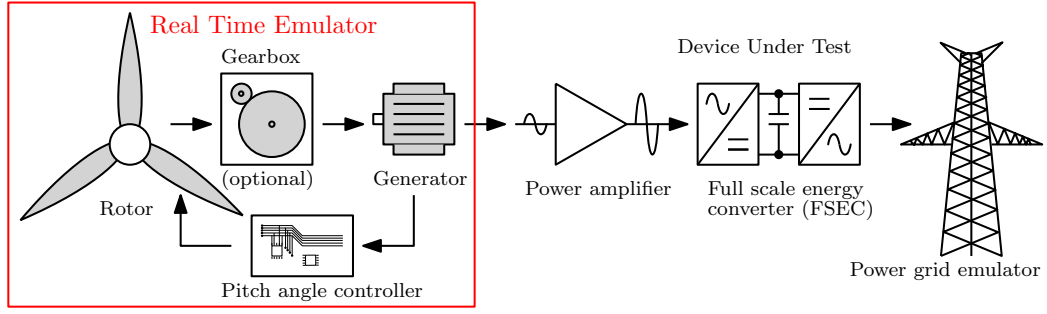


Figure 4.5: Emulation and hardware block schematic of the proposed test-bench

After the debugging and validation, the models can be translated in the real-time hardware platform specific programming language to be integrated in the physical test bench. The following sections are focused on the description of the mathematical models and their Matlab Simulink implementation.

4.3 WIND TURBINE ROTOR MODEL

The kinetic energy of a moving object with mass m and speed v can be expressed as:

$$E = \frac{1}{2} \cdot m \cdot v^2 \quad (4.5)$$

The power of the air moving at a constant mass flow rate is then:

$$E = \frac{dE}{dt} = \frac{1}{2} \cdot m \cdot v_w^2 \quad (4.6)$$

The power of a mass of air passing in a cross sectional area A is then described as:

$$P_w = \frac{1}{2} \cdot \rho \cdot A \cdot v_w^3 \quad (4.7)$$

where ρ is the air density.

Consider a tube of air moving toward a WT with a constant mass flow rate, as shown in 4.6 . Since the WT extracts part of its kinetic energy, the air speed v_i at the input of the WT is higher than the wind speed v_o at its output.

As the air is moving with constant mass flow rate, the tube cross section A_i is smaller than the swept area A and becomes larger after the turbine, A_o [7, 51]. Neglecting losses, the force F applied to the rotor by a mass m of moving air is then:

$$F = m \cdot (v_i - v_o) \quad (4.8)$$

The power extracted by the rotor P_{wt} is then:

$$\begin{aligned} P_{wt} &= m \cdot (v_i - v_o) \cdot v_x \\ v_x &= \frac{1}{2}(v_i + v_o) \end{aligned} \quad (4.9)$$

where v_x is the wind speed at the turbine section. This leads to the expression of the mechanical power as a function of the wind speed at the input and at the output of a WT:

$$P_{wt} = \frac{1}{2} \cdot m \cdot \rho \cdot A \cdot (v_i^2 - v_o^2)(v_i + v_o) \quad (4.10)$$

This equation is usually found in literature in a different form:

$$P_{wt} = \frac{1}{2} \cdot m \cdot \rho \cdot A \cdot C_p \cdot v^3 \quad (4.11)$$

where C_p is the turbine power factor obtained substituting (4.11) in (4.10) and expressing it as a function of v_i and v_o :

$$C_p = \frac{1}{2} \cdot \left(1 - \left(\frac{v_o}{v_i}\right)^2\right) \left(1 + \frac{v_o}{v_i}\right) \quad (4.12)$$

As shown in Fig. 4.1, the maximum theoretically achievable value of the power coefficient is 0.593 when the $v_i = 3v_o$ [1, 7, 84]. This means that one third of the initial speed is lost before the wind turbine and one third after. C_p is often obtained empirically from a scaled version of the turbine under study and expressed as a function of the tip speed ratio λ and the blades pitch angle β . For a three blades WT, the expression of C_p can be approximated as [51, 55, 63, 64]:

$$\begin{aligned} C_p(\beta, \gamma) &= \frac{1}{2} \cdot \left[\frac{116}{x} - 0.4 \cdot \beta - 5 \right] e^{-21/x} + 0.0068 \cdot \gamma \\ \frac{1}{x} &= \frac{1}{\gamma + 0.08 \cdot \beta} - \frac{0.035}{\beta^3 + 1} \end{aligned} \quad (4.13)$$

In Fig. 4.8 the values of C_p coefficient are plotted for different values of β and λ . It is easy to note that the maximum value of the power coefficient is obtained when the blades pitch angle is near to zero. This is the reason why the pitch angle is used to limit the rotor torque and the extracted power. Moreover, the maximum value of C_p is 0.48, that is lower than the theoretical one. It is very important to note that for any given value of β , there is only a tip speed ratio λ that maximizes C_p .

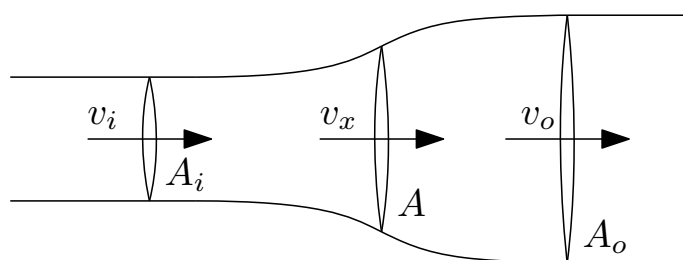


Figure 4.6: Tube of air moving at constant mass flow rate through a WT rotor

From (4.11) it is possible to obtain the equation of the WT torque simply by dividing the mechanical power by the rotational speed:

$$T_{wt} = \frac{P_{wt}}{\omega_{wt}} \quad (4.14)$$

Commonly, WT power and torque are expressed in terms of the power coefficient $C_p(\beta, \gamma)$ obtained by (4.13) as:

$$\begin{aligned} T_{wt} &= \frac{1}{2} \cdot \pi \cdot R^3 \cdot \rho \cdot \frac{v_w^2}{\gamma} \cdot C_p(\beta, \gamma) \\ P_{wt} &= \frac{1}{2} \cdot \pi \cdot R^2 \cdot \rho \cdot v_w^3 C_p(\beta, \gamma) \end{aligned} \quad (4.15)$$

In Fig. 4.11 and Fig. 4.10 the torque and power curve has been traced for $R = 5\text{m}$, $\beta = 0$, and different values of wind speeds (i.e. , $v_1, v_2, v_3 = 6, 9, 12\text{m/s}$). As expected, the torque and power curves highly depend on the turbine rotation speed ω_{wt} . In Fig. 4.8 the power coefficient is expressed as a function of the tip speed ratio for different blades pitch angle.

Equations (4.15),(4.4) and (4.13) can be used to obtain the rotor model, as shown in Fig. 4.9. The model depends on the wind speed v , the blades pitch angle β and the turbine rotation speed ω_{wt} . Finally, in Fig. 4.12, a Matlab Simulink implementation has been reported. The model inputs are the rotor rotational speed ω_{wt} , the blades pitch angle β and the wind speed v . The model outputs are the rotor torque T_{wt} and power P_{wt} .

4.4 PITCH ANGLE CONTROLLER MODEL

Since an increase of the blades pitch angle β determines a reduction in the power coefficient C_p for a given tip speed ratio λ , as shown in Fig. 4.8, the blades pitch angle is usually used to reduce the mechanical power extracted by the wind turbine. Thus, the mechanical power extracted from wind can be controlled by regulating the blades pitch angle.

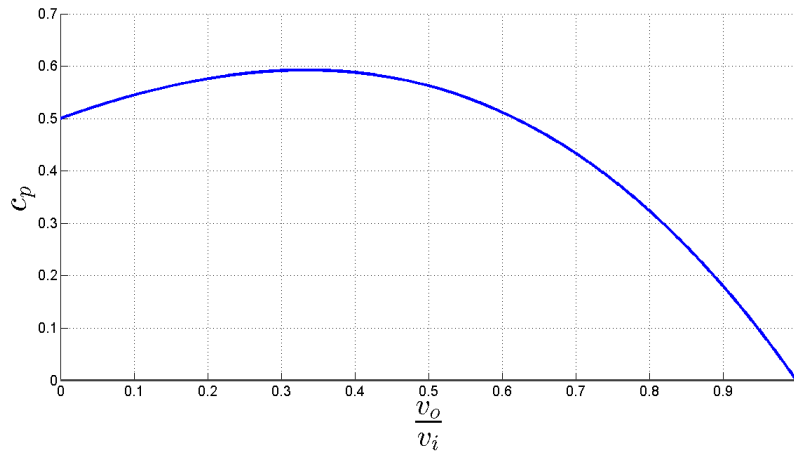


Figure 4.7: Theoretical power coefficient expressed as a function of the input and output wind speed ratio

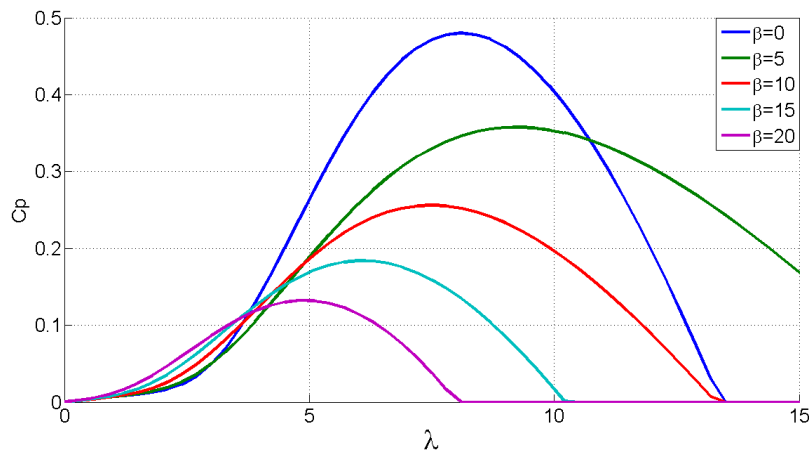


Figure 4.8: Power coefficient expressed as a function of the tip speed ratio λ and the blades pitch angle β

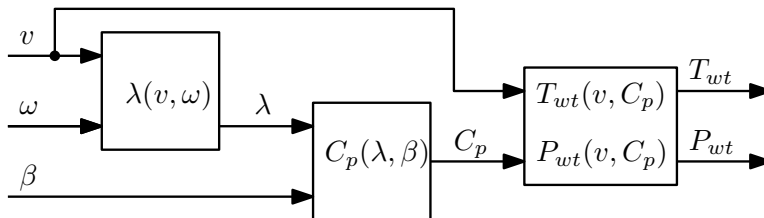


Figure 4.9: Rotor model block diagram based on (4.15), (4.4) and (4.13)

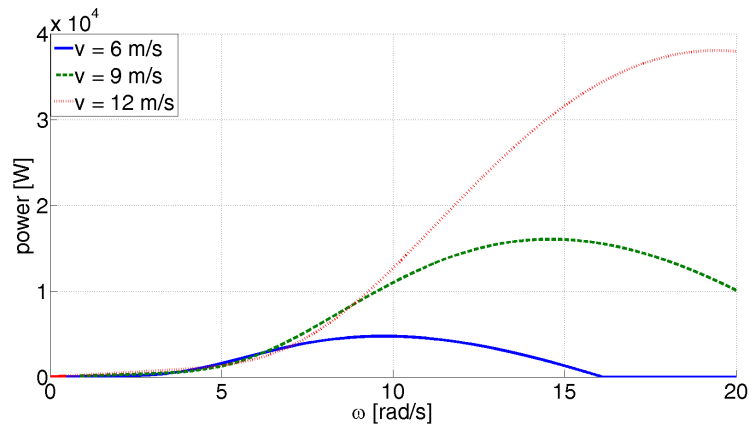


Figure 4.10: Mechanical power curves of WT with rotor radius $R = 5\text{m}$, pitch angle $\beta = 0$ and wind speed $v_1, v_2, v_3 = 6, 9, 12\text{m/s}$.

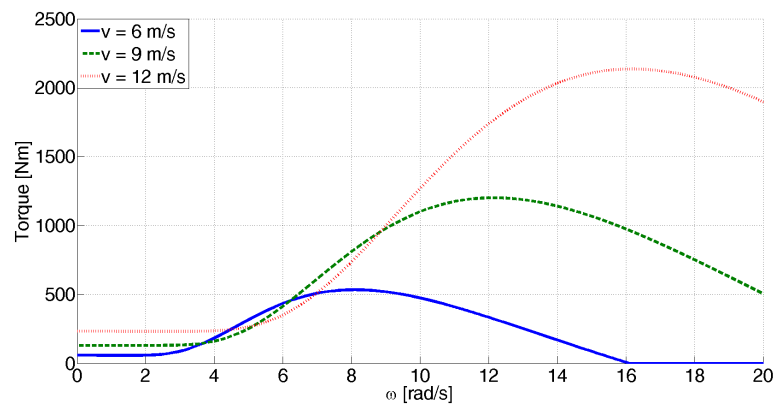


Figure 4.11: Torque curves of a WT with rotor radius $R = 5\text{m}$, pitch angle $\beta = 0$ and wind speed $v_1, v_2, v_3 = 6, 9, 12\text{m/s}$.

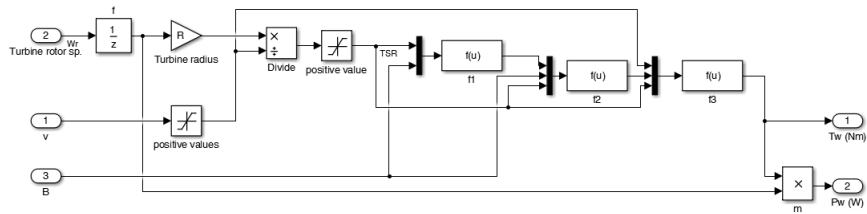


Figure 4.12: Rotor model in Matlab Simulink

In modern wind turbines a servo mechanism on the turbine rotates the blades on their axis in order to change their angle. To change the blades position electrical or hydraulic servos can be employed. The servo is controlled by the so called pitch angle controller, which provides the regulation and the limitation of the turbine performances during strong wind conditions. The pitch angle controller is strongly dependent on the WT characteristics and the manufacturer. Usually β ranges from -2° to 30° and varies at a maximum rate of $\pm 10^\circ/\text{s}$ [35]. In literature various control strategy are reported. In [7, 33, 35, 51, 87], the following four different control strategies are described.

1. Speed regulation PI controller. The pitch angle reference can be obtained from the difference between the turbine rotation speed and its nominal speed. The error between the two signals is then processed by a PI controller, which generates the reference value for the pitch angle, β_{ref} . This value is then compared with the measured pitch angle β and sent to the blades angle servo drive. This method allows to regulate the speed of the wind turbine at its nominal value [7]. The block diagram of this controller is shown in Fig. 4.13.
2. Speed regulation gain scheduling controller. An improvement of the previous controller can be obtained by using a gain scheduler to adapt the PI gains to the actual pitch angle [35]. The gain scheduling control compensates for the non-linear aerodynamic characteristics of the wind turbine. The total gain of the wind turbine can be expressed as the multiplication of the proportional gain $K_{P_{\text{pi}}}$ of the PI controller by the sensitivity $\frac{dP}{d\beta}$ of the system in a given operating point:

$$K_{pw} = K_{P_{\text{pi}}} \frac{dP}{d\beta}$$

The gain scheduler keeps constant the wind turbine gain, counteracting the variation of aerodynamic sensitivity $\frac{dP}{d\beta}$. This can be achieved by dividing the proportional gain by the sensitivity of the system at its operating point:

$$K'_{P_{\text{pi}}} = K_{P_{\text{pi}}} \frac{d\beta}{dP}$$

The block schematic of this controller is shown in Fig. 4.14.

3. Power regulation gain scheduling controller. The pitch controller shown in Fig. 4.15 calculates the difference between the output power of the generator and the rated power of the wind turbine. The obtained error is fed to a PI controller that produces the reference pitch angle β_{ref} . In this approach the pitch angle controls directly the generator output power to its nominal value. A gain scheduler can be used to linearize the aerodynamic characteristics of the wind turbine. As

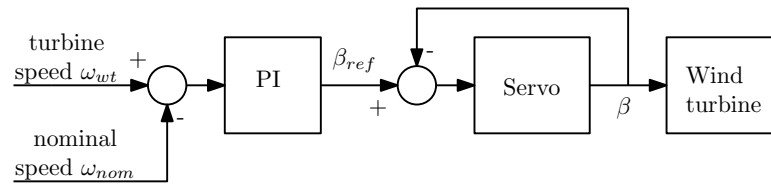


Figure 4.13: Pitch angle controller using the wind turbine nominal speed as reference

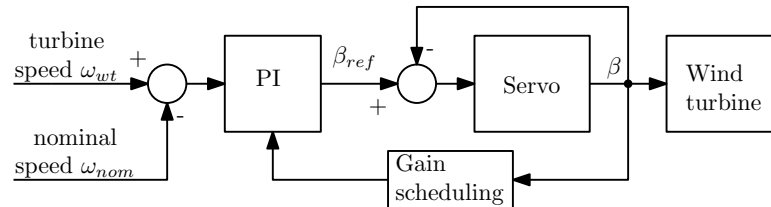


Figure 4.14: Rotor speed pitch angle controller based on gain scheduler

the sensitivity of the aerodynamic torque to pitch angle $K_{P_{pi}} \frac{dT}{d\beta}$ is small for low wind speeds, the controller requires a larger gain than in stronger wind conditions, where the same sensitivity is greater. Since the torque sensitivity typically changes almost linearly with the pitch angle, the gain scheduler is designed to change the PI controller gain in inverse proportion to the pitch angle [87].

4. Power regulation, fuzzy logic. A completely different approach is the fuzzy logic based pitch angle controller shown in Fig. 4.16. Fuzzy logic controllers are useful when the system is highly non linear or when its dynamics are not well known. This is often the case of a wind turbine in turbulent wind conditions. In those situations, fuzzy logic controllers can help reducing mechanical fatigue and stresses [87].

4.4.1 PI controller with angle gradient limiter

The chosen structure for the pitch controller model is a PI regulator in conjunction with an angle gradient limiter. The main goal of the controller is to prevent the rotor

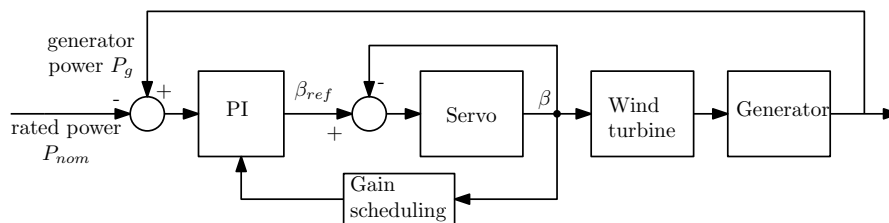


Figure 4.15: Pitch angle regulator using nominal power as reference

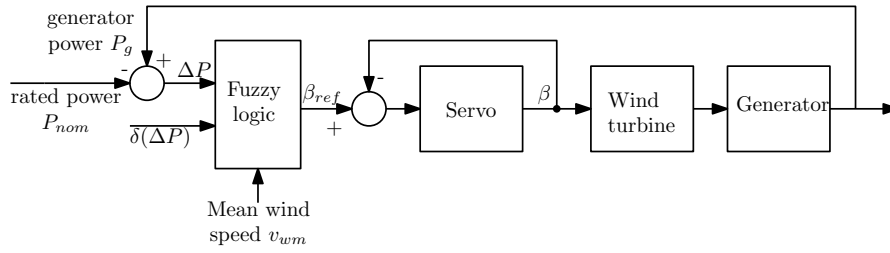


Figure 4.16: Pitch angle regulation controller based on fuzzy logic

speed from exceeding its nominal value under high wind speed conditions [7] and, working together with the wind energy converter, to limit the extracted power to its nominal value. As shown in Fig. 4.8, the whole system power extraction can be divided into three operative zones [7, 51], as shown in Fig. 4.17:

1. Low wind speed: v_w is below its nominal value v_{wnom} so the turbine rotational speed ω_{wt} is smaller than its nominal value ω_{nom} . Therefore the pitch angle controller is disabled and the WT operates in the maximum power extraction point. The turbine speed in this operative area is regulated only by the WEC.
2. Medium wind speed: v_w is higher than its nominal value v_{wnom} , causing the WT speed to exceed its nominal value ω_{nom} . Therefore the pitch angle controller is activated and β is increased to reduce the mechanical extracted power. In this region the WEC and the pitch controller operates together and ω_{wt} is limited to its nominal value ω_{nom} .
3. High wind speed: v_w is much higher than v_{wnom} . In those conditions the WEC is processing its maximum power and it is not able to limit the turbine speed by raising the extracted currents and so increasing the generator torque. Therefore the WT speed regulation can only be performed by the pitch angle controller, regulating ω_{wt} to its nominal value ω_{nom} by acting on the blade pitch angle β , while the WT energy converter extracts its rated nominal power.

Since the pitch angle controller structure is highly variable and is dependent on both the manufacturer and wind turbine type it is impossible to synthesize a generic model. Nonetheless, there are some generic characteristics common along all the pitch angle controllers. More specifically the controller usually drives a servomechanism typically modeled as a single pole time constant [7]. Moreover, a pitch angle limiter and a gradient limiter is added to some models [33, 35]. Thus, in general terms, the pitch controller can be modeled as shown in Fig. 4.17, where the controller is active only when $\omega_{wt} > \omega_{nom}$. The servo time constant takes into account of the servomechanism responsiveness and the gradient limiter emulates its maximum speed, limiting the angle variation rate of the blades. An angle limiter takes into account of the finite excursion of the blades angle.

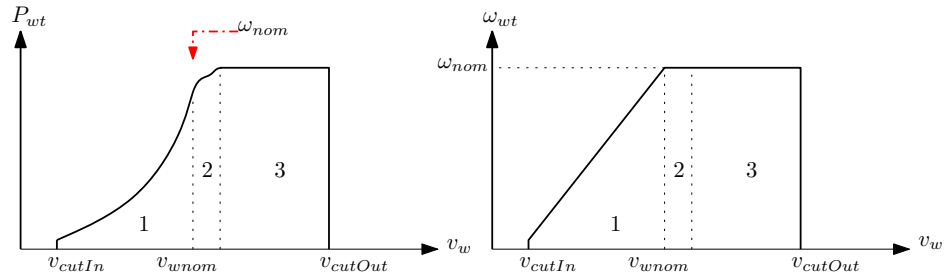


Figure 4.17: Power extraction operative zones

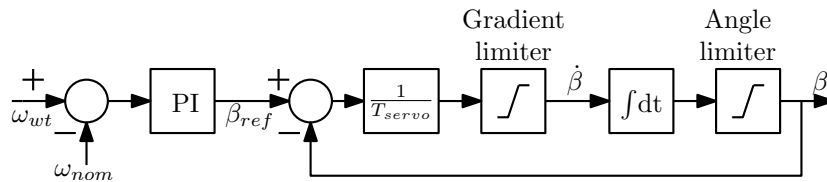


Figure 4.18: Model of the pitch angle controller and servo mechanism

4.5 DRIVE TRAIN AND GEARBOX MODEL

The drive train of a WT consists of:

- Rotor
- Low speed shaft
- Gearbox
- High speed shaft
- Generator

The low and high speed shafts are designed to connect mechanically the rotor with the gearbox and the gearbox with the generator, respectively. The gearbox role in a WT system is to convert the low speed, high torque mechanical power at the rotor shaft to a high speed, low torque mechanical power at the generator shaft. Neglecting gearbox losses, the rotor and the generator mechanical power are equal:

$$P_{wt} = T_{wt} \cdot \omega_{wt} = P_e = T_e \cdot \omega_g \tag{4.16}$$

where T_e , P_e and ω_g are, respectively, the torque, power and angular speed at the generator side. The constant that links the rotor rotational speed ω_{wt} , its torque T_{wt} , the generator speed ω_g and its torque T_g is the gearbox ratio n_g given by:

$$\begin{aligned} n_g &= \frac{\omega_g}{\omega_{wt}} \\ n_g &= \frac{T_{wt}}{T_g} \end{aligned} \quad (4.17)$$

Kinetic energy is stored in the WT rotating masses. More specifically, the kinetic energy stored at the rotor E_{kwt} and generator side are E_{kg} :

$$\begin{aligned} E_{kwt} &= \frac{1}{2} \cdot J_{wt} \cdot \omega_{wt}^2 \\ E_{kg} &= \frac{1}{2} \cdot J_g \cdot \omega_g^2 \\ \omega_g &= n_g \cdot \omega_{wt} \end{aligned} \quad (4.18)$$

where J_g is the generator and gearbox moment of inertia and J_{wt} the rotor moment of inertia. When power losses are neglected, all the energy harvested by the rotor equals the energy on the generator side, therefore, substituting (4.17) in (4.18) leads to :

$$J_g = \frac{J_{wt}}{n_g^2} \quad (4.19)$$

In the drive train mathematical description of the gearbox rotating parts it is a common practice to neglect second order effects, as their dynamics are much slower than the generator one [56, 69]. This allows to treat the entire drive train as a single lumped mass [55]. Using (4.19), it is possible to compare the turbine moment of inertia with the generator one. This leads to the simplified dynamic equation describing the rotational system:

$$\frac{T_{wt}}{n_g} = J_{eq} \cdot \frac{d(n \cdot \omega_g)}{dt} + T_g + B(n \cdot \omega_g) \quad (4.20)$$

where B is the friction coefficient, expressed in $\frac{Nm}{rad/s}$, and J_{eq} is the equivalent generator side rotational inertia, obtained as:

$$J_{eq} = J_g + \frac{J_{wt}}{n_g} \quad (4.21)$$

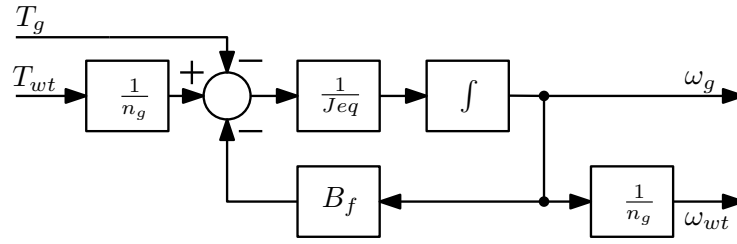


Figure 4.19: Drive train block diagram highlighting the model inputs and outputs

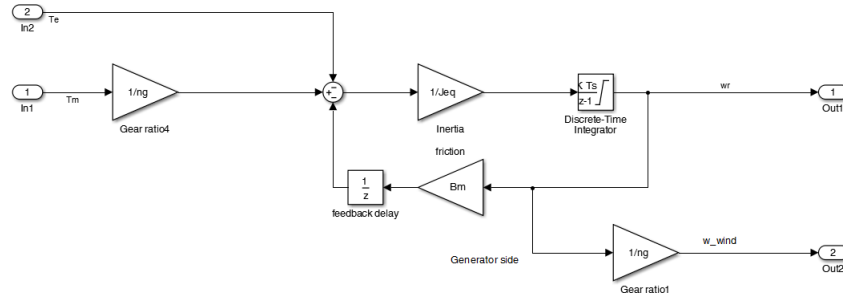


Figure 4.20: Drive train model in Matlab Simulink

By using (4.20), (4.21) and (4.17) the model shown in Fig. 4.19 can be obtained. Finally, Fig. 4.20 shows one of the possible implementations of the drive train model using Matlab Simulink. The model inputs are the turbine torque T_{wt} and the generator torque T_g . Its outputs are the turbine rotational speed ω_{wt} and the generator rotational speed ω_g .

4.6 PERMANENT MAGNET SYNCHRONOUS GENERATOR MODEL

The PMSG equations representing its output voltages can be expressed as:

$$\begin{aligned}
 u_a &= R_s \cdot i_a + L_a \frac{di_a}{st} - \Psi_f \cdot \omega_e \cdot \sin(\theta_e) \\
 u_b &= R_s \cdot i_b + L_b \frac{di_b}{st} - \Psi_f \cdot \omega_e \cdot \sin\left(\theta_e - \frac{\pi}{2} - \frac{2\pi}{3}\right) \\
 u_c &= R_s \cdot i_c + L_c \frac{di_c}{st} - \Psi_f \cdot \omega_e \cdot \sin\left(\theta_e - \frac{\pi}{2} - \frac{4\pi}{3}\right)
 \end{aligned} \tag{4.22}$$

where u_a, u_b, u_c are the generator output voltages, i_a, i_b, i_c the output currents, Ψ_f the permanent magnet magnetic flux, R_s the stator winding resistance, and ω_e the electromechanical speed obtained by multiplying the rotor speed by the number of poles pairs p :

$$\omega_e = p \cdot \omega_g \tag{4.23}$$

Consequently, the electric angle is given by the generator angle multiplied by the pole pairs:

$$\theta_e = p \cdot \theta_g \quad (4.24)$$

Moreover L_a, L_b, L_c are the sum of the self and mutual inductance, depending on the angle θ_e .

$$\begin{aligned} L_a &= L_{aa}(\theta_e) + L_{ab}(\theta_e) + L_{ac}(\theta_e) \\ L_b &= L_{ab}(\theta_e) + L_{bb}(\theta_e) + L_{bc}(\theta_e) \\ L_c &= L_{ac}(\theta_e) + L_{bc}(\theta_e) + L_{cc}(\theta_e) \end{aligned} \quad (4.25)$$

This representation is not very useful, as the equations depend on the rotor position. For this reason the equations are usually expressed in the dq0 rotating reference frame. The following matrix $T_{abc/dq0}$ is used to convert a three phase abc system in a dq0 reference frame:

$$T_{abc/dq0} = \sqrt{\frac{2}{3}} \begin{bmatrix} \cos(\theta_e) & \cos(\theta_e - \frac{2\pi}{3}) & \cos(\theta_e + \frac{2\pi}{3}) \\ \sin(\theta_e) & \sin(\theta_e - \frac{2\pi}{3}) & \sin(\theta_e + \frac{2\pi}{3}) \\ \frac{\sqrt{2}}{2} & \frac{\sqrt{2}}{2} & \frac{\sqrt{2}}{2} \end{bmatrix} \quad (4.26)$$

As usually generators work with the neutral connection floating, there is no need to consider the zero sequence, so the zero component can be neglected and the conversion matrix becomes:

$$T_{abc/dq0} = \sqrt{\frac{2}{3}} \begin{bmatrix} \cos(\theta_e) & \cos(\theta_e - \frac{2\pi}{3}) & \cos(\theta_e + \frac{2\pi}{3}) \\ \sin(\theta_e) & \sin(\theta_e - \frac{2\pi}{3}) & \sin(\theta_e + \frac{2\pi}{3}) \end{bmatrix} \quad (4.27)$$

To convert the dq reference frame into abc quantities, an inverse transform matrix is needed:

$$T_{dq0/abc} = \sqrt{\frac{2}{3}} \begin{bmatrix} \cos(\theta_e) & \sin(\theta_e) \\ \cos(\theta_e - \frac{2\pi}{3}) & \sin(\theta_e - \frac{2\pi}{3}) \\ \cos(\theta_e + \frac{2\pi}{3}) & \sin(\theta_e + \frac{2\pi}{3}) \end{bmatrix} \quad (4.28)$$

The PMSG equation can then be converted in the dq0 reference frame as follows:

$$\begin{bmatrix} u_d \\ u_q \end{bmatrix} = \sqrt{\frac{2}{3}} \begin{bmatrix} \cos(\theta_e) & \cos(\theta_e - \frac{2\pi}{3}) & \cos(\theta_e + \frac{2\pi}{3}) \\ \sin(\theta_e) & \sin(\theta_e - \frac{2\pi}{3}) & \sin(\theta_e + \frac{2\pi}{3}) \end{bmatrix} \cdot \begin{bmatrix} u_a \\ u_b \\ u_c \end{bmatrix} \quad (4.29)$$

A well established mathematical model of salient-pole and non-salient pole PMSGs can be obtained under the following two assumptions :

- The stator windings are positioned sinusoidally along the air-gap
- The stator slots cause no appreciable variations of the rotor inductances with the rotor position

The obtained PMSG equations can be finally expressed in a more straightforward representation [25, 48, 60, 64], where the current sign has been expressed in the motor convention, i.e. , entering the generator output terminals :

$$\begin{aligned} u_d &= L_d \frac{di_d}{dt} + R_s \cdot i_d - \omega_e \cdot L_q \cdot i_q \\ u_q &= L_q \frac{di_q}{dt} + R_s \cdot i_q + \omega_e \cdot L_d \cdot i_d + \omega_e \cdot \Psi_f \end{aligned} \quad (4.30)$$

In this representation L_d and L_q , namely, the direct and quadrature characteristic inductances, respectively, do not depend on the rotor position and their values are constant. Finally, the expression linking the generator torque with its output currents is:

$$T_g = \frac{3}{2} \cdot p \cdot [(L_d - L_q) \cdot i_d \cdot i_q + i_q \cdot \Psi_f] \quad (4.31)$$

It is clear that the generator torque depends on the inductances, the absorbed currents, the permanent magnet magnetic field and the number of poles. Additionally, if $L_d = L_q$, as it happens in non-salient poles generators, an external three phase inductance can be added to emulate the PMSG one. This allows to further simplify the PMSG model, moreover, a physical inductance is absolutely necessary to filter the currents absorbed by the WEC from the controllable power supply. By using external physical inductances to emulate L_d and L_q , the following simplified expression can be obtained:

$$\begin{aligned} u_d &= R_s i_d \\ u_q &= R_s i_q + \omega_e \Psi_f \\ T_e &= \frac{3}{2} p i_q \Psi_f \end{aligned} \quad (4.32)$$

In a rotating dq reference frame the expressions to calculate the active and reactive power are:

$$\begin{aligned} P &= u_d i_d + u_q i_q \\ Q &= u_q i_d - u_d i_q \end{aligned} \quad (4.33)$$

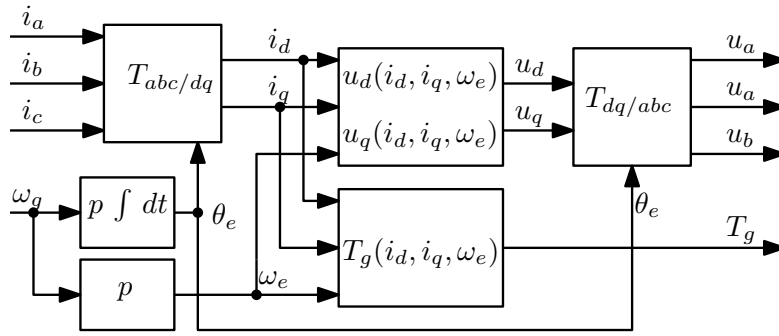


Figure 4.21: Permanent magnet synchronous generator model structure

If the synchronous frame is aligned to the u_q voltage, its direct component u_d is null. This further simplifies the active and reactive power expressions to:

$$\begin{aligned} P &= u_q i_q \\ Q &= u_q i_d \end{aligned} \tag{4.34}$$

As the reactive power depends on the current direct component, the WEC regulates the i_d current to zero. This allows the WEC to absorb only active power from the generator.

Fig. 4.21 represents a block schematic of the PMSG model structure. The model outputs are the generator voltages v_a, v_b, v_c and torque T_g ; its inputs are the absorbed currents i_a, i_b, i_c and rotor speed ω_g .

As the generator output currents have to be measured individually, their natural representation is the abc reference frame, so a transformation has to be applied to convert the currents in the dq. The transformation matrix inputs are the abc currents and the generator electric angles θ_e .

After the conversion, the dq currents will be used to compute the stator voltages (7.1). An integrator block and a multiplier by the pole pairs number p are also needed to convert the generator speed ω_g to the electric speed ω_e and the electric angle θ_e used to perform both the abc to dq and the dq to abc conversions.

As the generator output voltages are needed in the abc reference to be singularly amplified by the test-bench controllable power supply, an inverse transformation is performed. The voltages u_d, u_q are converted back in the abc reference frame by applying the transformation matrix $T_{dq0/abc}$. A Matlab Simulink implementation of the PMSG model implementation is reported in Fig. 4.23.

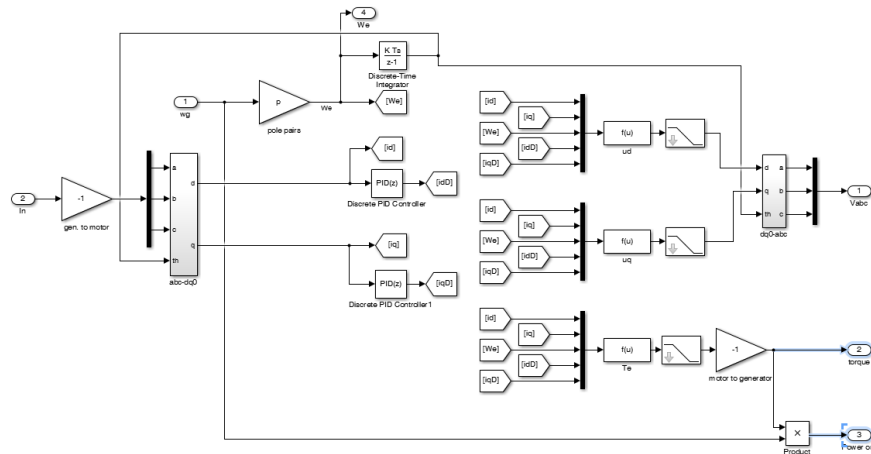


Figure 4.22: Permanent magnet synchronous generator model in Matlab Simulink

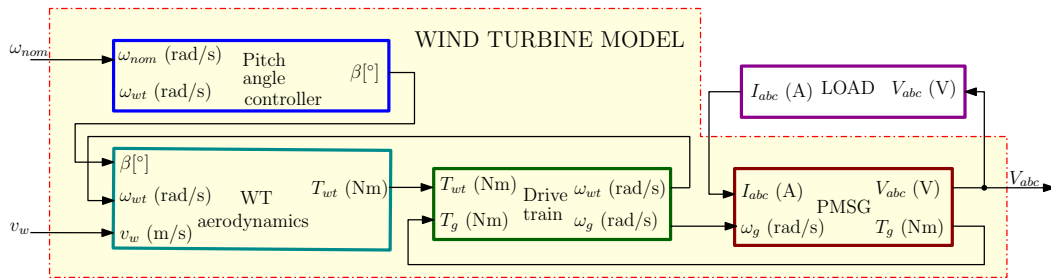


Figure 4.23: Block diagram of the model needed to implement the WT emulator

4.7 OVERALL WIND TURBINE MODEL

Fig. 4.23 shows the overall WT model obtained from all the parts described in the previous paragraph. The overall model requires the wind speed v_w and the abc currents absorbed by the generator. The overall outputs are the PMSG abc three phase voltages.

Fig. 4.24 depicts the Matlab Simulink model implementation, where each functional block has been combined in a single subsystem to make the simulation code more clear. The blue block represents the pitch angle controller model, the yellow block implements the rotor model, the green block represents the drive train and the red block the PMSG model.

4.8 WIND ENERGY CONVERTER MODEL

To be able to run a complete numeric simulation, it is necessary to include the model of the WEC typically mounted on a variable speed WT. Moreover a grid simulation

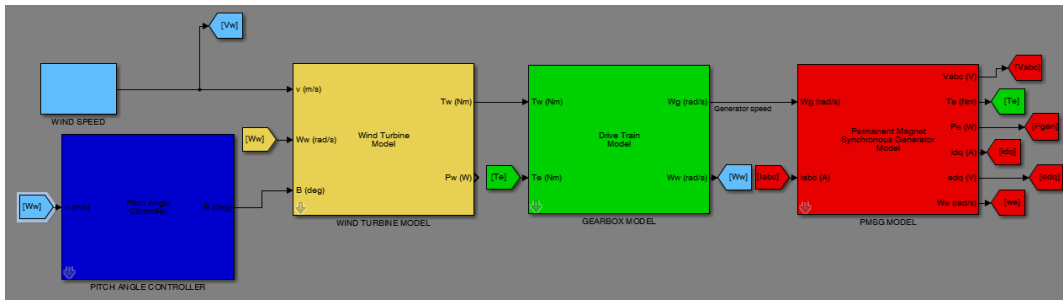


Figure 4.24: Matlab Simulink overall wind turbine simulation model

including a voltage sag generator has to be realized to be able to run LVRT testing simulations on the WT and WEC models.

Two levels, three level or multilevel converters can be considered, depending on the power ratings and voltages of the specific WT application. From the certification point of view, the topology of the WEC is not important as long as the converter is a full rated power converter. The back to back full power converter, whose structure is shown in Fig. 4.27, represents the most used configuration to realize a WEC, especially for medium power WTs [45, 73].

In a back to back WEC the control is realized by using the approach showed in Fig. 4.28, where the grid side inverter controls the DC link bus voltage V_{DC} and regulates the active and reactive power injected into the grid [9, 11, 36, 37].

Differently, the generator side inverter is controlled to absorb the maximum power a WT in given conditions of wind speed and rotation speed can deliver. This can be archived by implementing a maximum power point tracking control, where the WEC converter indirectly controls the WT to work in its maximum C_p power coefficient [41]. Another way to maximize the power extraction is by programming the WEC with specific torque curves [2, 11, 47], function of the WT rotation speed.

Fig.4.25 shows the turbine power curves for different rotation and wind speeds. The WT rotation speed has been converted in the generator output voltages frequency f_e :

$$f_e = 2 \pi p n_g \omega_{wt} \tag{4.35}$$

The dashed curve in Fig.4.25 represents the maximum power extraction point for different wind speeds. This relation has been obtained linking the maximum power point of the WT for different wind speeds. The maximum power curve links the torque to be applied from the generator to the WT to maximize the wind power conversion.

The most used approach to implement a maximum efficiency regulation is the field oriented control (FOC) where the optimum electromagnetic torque is controlled through the stator current in the dq reference frame [9]. This is usually archived by programming a lookup table linking the generator extracted current to the WT rotation speed [2, 47, 52, 63]. The constructor determines the turbine torque curves that maximize the power extraction as a function of rotation speed. The WEC is programmed to

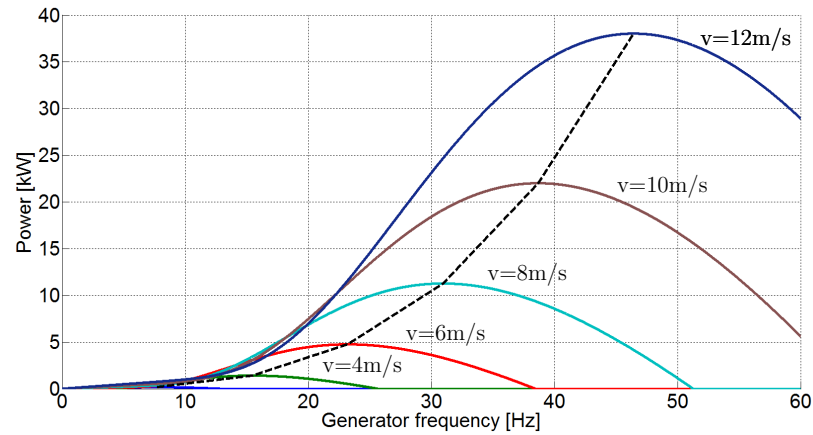


Figure 4.25: WT power and maximum efficiency curves for different wind and rotation speeds

apply the needed resisting torque on the generator side to obtain a maximum efficiency power extraction. In particular, the generator torque can be directly controlled by acting on its quadrature current i_q . As shown in 4.36, by forcing to zero the generator direct current the PMSG torque equation simplifies to:

$$T_g = \frac{3}{2} \cdot p \cdot i_q \cdot \Psi_f \quad (4.36)$$

In Fig. 4.26 it is shown the torque curve to be applied at the generator side to obtain a maximum efficiency conversion. The curves in Fig. 4.26 are obtained for a WT with radius $R = 5\text{m}$, a gearbox with ratio $n_g = 3$, a 5 pole pairs PMSG with magnetic field $\Psi_f = 0.9\text{Wb}$.

It is worth remarking that many topology solutions exists to implement WECs. Some examples are [73]:

- Forced-commutation voltage source inverters
- Phase-controlled line-commutated converters
- Force-commutated current source inverters
- Two levels back to back PWM voltage source inverters
- Two levels back to back PWM current source inverters
- Three levels back to back PWM voltage source inverters
- Thyristor-based phase controlled current source inverters

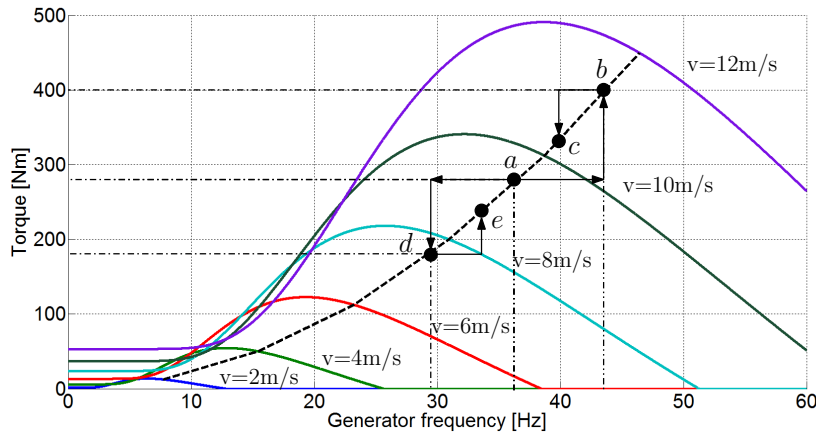


Figure 4.26: Generator side torque and maximum efficiency curves for different wind and rotation speeds

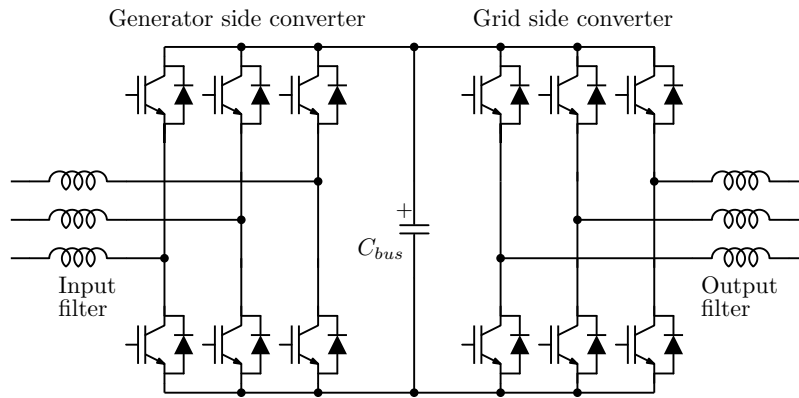


Figure 4.27: Bidirectional back to back power converter based WEC

Nevertheless, an in depth analysis of relevant converter topologies is not present here, as the purpose of the developed test bench is to test the WEC standard compliance independently by its physical realization. Therefore, the most simple and common WEC converter topology has been chosen to be modeled. The simulations have been performed using a two level back to back voltage source based WEC. The back to back WEC model, developed in Matlab Simulink, is represented in Fig. 4.29. The green blocks highlight the generator side converter and the blue blocks the grid side converter. Finally, the light-blue block represents the maximum power point lookup table.

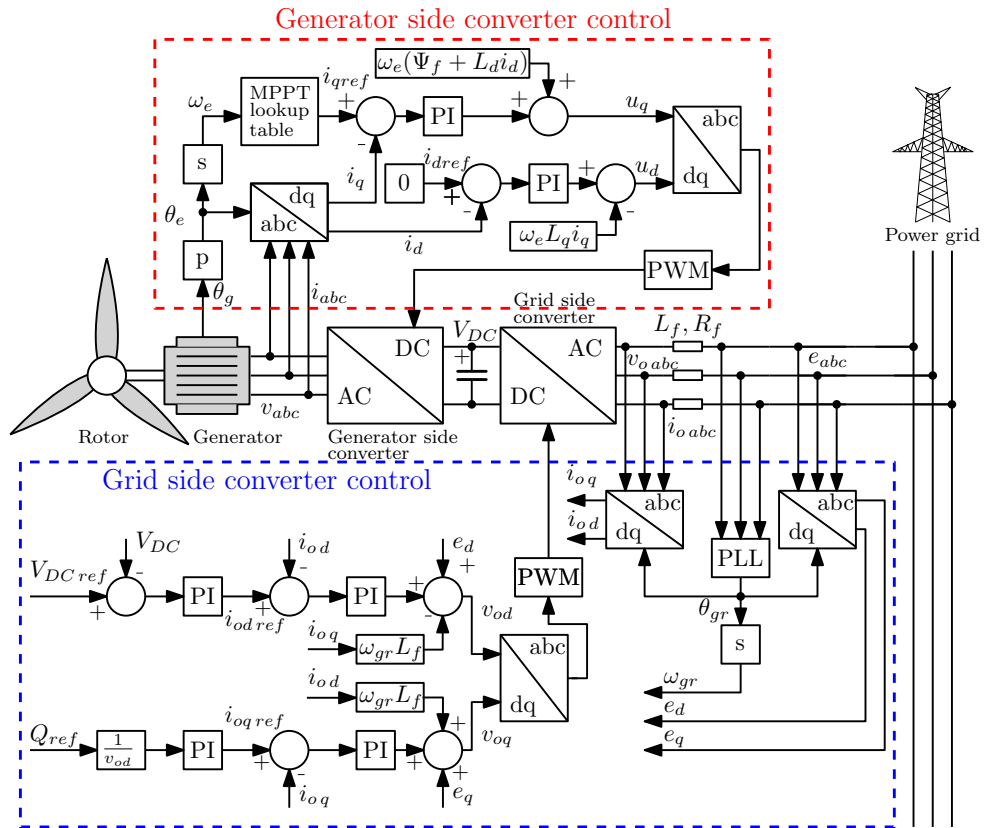


Figure 4.28: Bidirectional converter control block diagram, the generator side converter control highlighted in the red box and the grid side converter in the blue one [9]

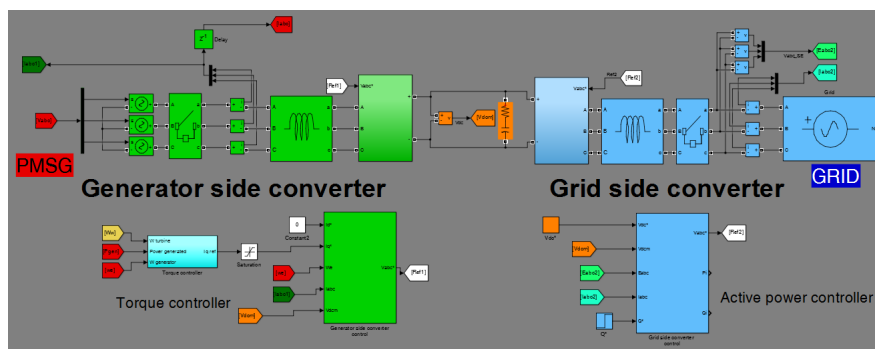


Figure 4.29: Matlab Simulink back to back WEC simulation model

4.8.1 Generator side converter

In the generator side controller the generator position θ_g is measured by an encoder and used to obtain the electric angle θ_e and frequency ω_e . The electric angle is used by the abc – dq reference frame converter to express the generator output currents i_{abc} in the dq reference frame, i_d and i_q . The maximum power point lookup table generates the q axis reference current i_{qref} from the generator electrical speed θ_e . This reference allows to extract the exact torque value to maximize the WT efficiency. On the other hand, the d axis current is regulated to zero by a second PI controller to minimize the extracted reactive power and so the resistive losses [9].

The two current regulators outputs represent the generator converter reference dq voltages. To decouple the voltage references from the currents i_d , i_q the feed-forward compensation terms $\omega_e(\Psi_f + L_d i_d)$ and $\omega_e(L_q i_q)$ are introduced. This allows to separately control the active and reactive power extracted from the generator separately. The voltage references u_d and u_q are then converted in the abc reference frame to be fed into a pulse width modulation (PWM) block driving the full bridges of the grid side converter.

4.8.2 Generator side converter operation

Suppose a WT operating in steady state at the point a) in Fig. 4.26. If the wind speed increases the WT accelerates, increasing the generator speed ω_e . The new rotation speed value will be translated by the maximum power point lookup table to a higher current reference i_{qref} and so to a higher generator torque T_e , reaching point b) in Fig. 4.26. This causes an unbalance between the generator torque T_g and the rotor one T_{wt} . The unbalance lead the system to slow down, reaching point c).

Differently, if a WT operates at a) and the wind speed decreases, the rotor torque and speed will decrease. Consequently the controller reduces the current absorption, according to the point d). Consequently, the torque unbalance causes the system speed ω_e to increase to point e).

This process continues depending on the system time constants and stability margin until the generator torque T_g equals the turbine one T_{wt} and a stable operational point is reached. This mechanism introduces a negative feedback stabilizing the turbine speed to its optimal angular speed and maximum power extraction point.

Furthermore, if the WEC is absorbing the converter nominal current, it is not possible to further increase the resisting torque of the PMSG to limit the rotor speed. For these reasons at high speed conditions the pitch angle controller intervention is of fundamental importance to control the WT rotation speed.

4.8.3 Grid side converter

The grid side converter output currents can be expressed as [73]:

$$\begin{aligned}\frac{di_{od}}{dt} - \omega_{gr} i_{oq} &= \frac{1}{L_f} [R_f i_{od} - e_d + D_d(t) V_{DC}] \\ \frac{di_{oq}}{dt} + \omega_{gr} i_{od} &= \frac{1}{L_f} [R_f i_{oq} - e_q + D_q(t) V_{DC}]\end{aligned}\quad (4.37)$$

where e_d and e_q are the grid voltages in the dq reference frame, i_{od} and i_{oq} the dq output currents, $D_d(t)$ and $D_q(t)$ are the switching duty cycles driving the WEC grid side bridge, expressed in dq reference frame. Finally, R_f and L_f represent, respectively, the resistance and inductance of the grid side filter, ω_{gr} is the grid angular speed and V_{DC} is the WEC DC link voltage.

The control strategy here implemented is the voltage oriented control (VOC). As shown in Fig. 4.28 the grid side controller is based on two main regulation loops, the outer one regulating the active and reactive output power and the DC link voltage, the inner one regulating the grid currents i_{oabc} [9, 86]. Both control loops rely on a PLL synchronized to the grid voltage. The PLL extracts the grid voltage angle used by the abc to dq reference frame converter to convert the grid voltages e_{abc} and the WEC output currents i_{abc} in the dq reference frame.

The DC link voltage can be subjected to transients due to the change of the generator side converter active power absorption. More specifically, an increase of power injected into the DC link by the generator side converter causes a voltage overshoot, while a decrease of power causes a voltage undershoot. Those voltage variations must be compensated by increasing or decreasing the WEC output active power, respectively [73].

The outer loop is based on two separate loops regulating the DC link voltage and the reactive power, as shown in Fig. 4.28. To control the DC link voltage to a constant reference value the entire active power absorbed from the generator must be injected into the grid. This is archived by the outer loop regulating the DC link voltage V_{DC} to its reference V_{DCref} value.

The reactive power is controlled to a reference value by controlling the q-axis current to its reference value i_{oqref} . The active power reference is obtained from the DC link outer loop. The dq voltage reference v_{od} is obtained by a PI controller processing the i_{od} current error and decoupling the result from the i_{oq} current and the grid voltage e_d . Likewise, v_{oq} is obtained by a PI controller processing the i_{od} current error and decoupling the result from the i_{od} current and the grid voltage e_q . The obtained reference voltages are then translated in the abc reference frame and then fed to a PWM modulator driving the WEC grid side converter.

SIMULATIONS

5.1 INTRODUCTION

As this work concerns LVRT tests on a small-medium power WTs, particular reference is made herein to the Italian low voltage grid code CEI 0-21 [17]. The grid code requirements for LVRT are shown in Fig. 5.1 and Tab. 5.1, [17]. More precisely, in Fig. 5.1 the green area highlights the voltage sag profile where the WT disconnection is not allowed, the grey one where disconnection is allowed and the blue one where the WEC must restart inject active or reactive power after the voltage sag.

The WEC is not allowed to disconnect from the grid when a voltage sag of any amplitude happens on the grid, if its duration is smaller than 200ms. If, as highlighted in the gray area in Fig. 5.1, the voltage sag amplitude keeps lower than 40% of the nominal voltage for more than 200ms, or lower than $85\%V_n$ for more than 400ms, then the WT can disconnect from the grid.

If the voltage sag is inside the green area in Fig. 5.1, the WT can interrupt the current injection without being disconnected from the grid. If, after a voltage sag, the voltage returns into the blue area, the WT must restart to deliver power to the grid in 200ms.

5.2 LVRT SIMULATION RESULTS

The complete WT system model has been tested over different operating conditions, voltage sag amplitudes and durations. Tab. 5.2 summarizes the WT parameters used in the simulations.

During a voltage sag the WEC can behave differently, depending on its realization and the specific grid code. In some cases during a voltage sag the WEC injects reactive power into the grid, in other cases it simply stops injecting power. In the case here

Table 5.1: Grid code LVRT requirements [17]

Case	Residual voltage, ph-ph, V/V_n	Duration [ms]
Three-phase symmetrical fault	0.05 ± 0.05	200 ± 20
Three-phase asymmetrical fault	0.45 ± 0.05	400 ± 20
Bi-phase asymmetrical fault	0.05 ± 0.05	200 ± 20
Bi-phase symmetrical fault	0.45 ± 0.05	400 ± 20

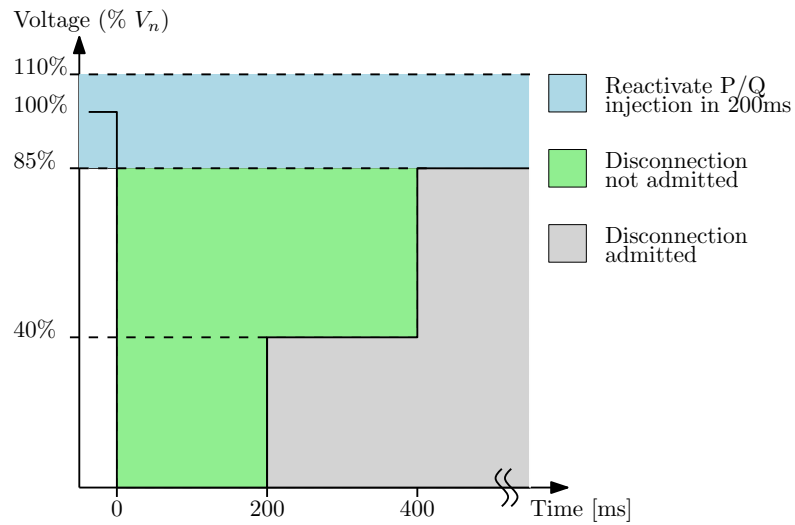


Figure 5.1: Voltage sag profile in CEI 0-21 Italian grid code, [17]

Table 5.2: Simulation parameters

WT nominal power [kW]	30
DUT nominal power [kW]	30
Grid nominal voltage V_n [V]	230
Grid nominal frequency [Hz]	50
Air density [kg/m^3]	1,205
Turbine radius [m]	5
Rotor flux [Wb]	0.9
Pole couples number	5
Generator inductance [mH]	4
Generator resistance [Ω]	0.1
Gear ratio	3
Friction coefficient [Nm/rad]	0
Rotor inertia [$\text{kg} \cdot \text{m}^2$]	90
Pitch actuator maximum speed [$^\circ/\text{s}$]	10

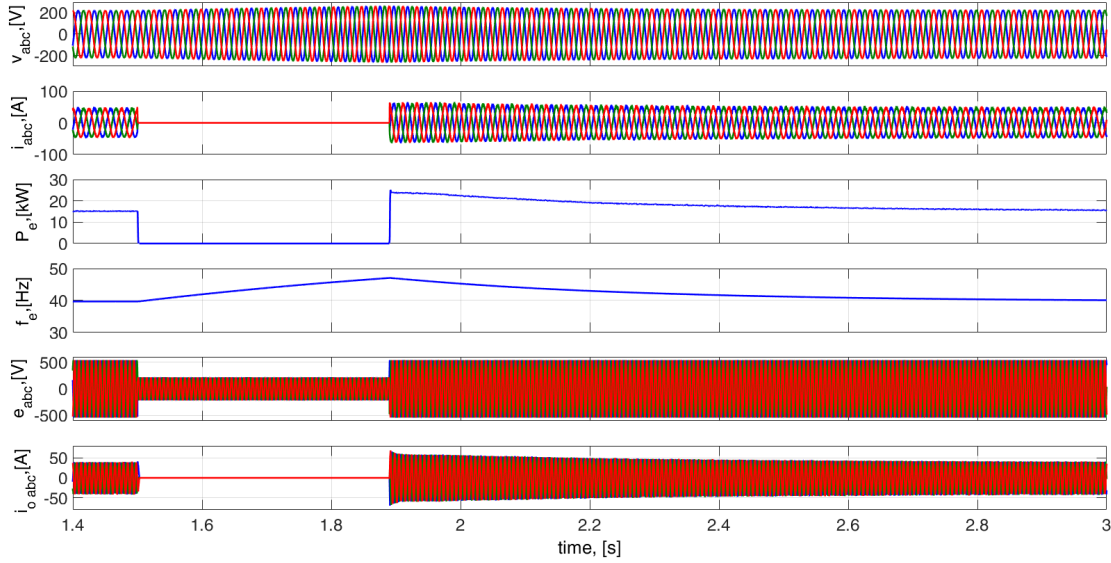


Figure 5.2: Simulation results of a LVRT test of $45\%V_n$ of the nominal voltage amplitude and duration 390ms. From top to bottom: generator voltages v_{abc} , generator currents i_{abc} , generator power P_e , generator output frequency f_e , grid voltages v_{oabc} and grid currents i_{oabc}

considered it is assumed that the WEC turns off the PWM gating during the voltage sag and promptly recovers afterwards, if the voltage sag amplitude is within the area where disconnection is not allowed. This assumption has been verified in the commercial WEC under test used in the test bench. Fig. 5.2 reports the main waveforms during a LVRT where a $45\%V_n$ voltage sag is applied for 390ms. The voltage sag amplitude and duration are identified by the red circle in Fig. 5.9.

Fig. 5.2 shows, from top to bottom, the generators voltages v_{abc} and currents i_{abc} , the generator output active power P_e , the generator output frequency f_e , the grid voltages e_{abc} and currents i_{oabc} . During the voltage sag the DUT stops absorbing power from the PMSG, indeed the generator currents i_{abc} drop to zero. Thus, since the turbine mechanical torque is still applied, without being counterbalanced by the generator one, the WT speed increases, as indicated by the increase of the frequency f_e shown in Fig. 5.3. In this case the simulation shows a WT overspeed of 19.8%. After 200ms the voltage sag amplitude is higher than 45%, so the WEC is not allowed to disconnect from the grid. As the voltage sag ends before 400ms, the standard CEI 0-21 imposes the WEC converter to restart its normal operation absorbing active power from the PMSG and injecting current into the grid. Thus, the system returns to its initial equilibrium state.

In Fig. 5.4 and its zoomed-in view in Fig. 5.5, a $0\%V_n$ voltage sag has been applied for 190ms. This voltage sag is identified by the red dot in Fig. 5.10. As the voltage sag

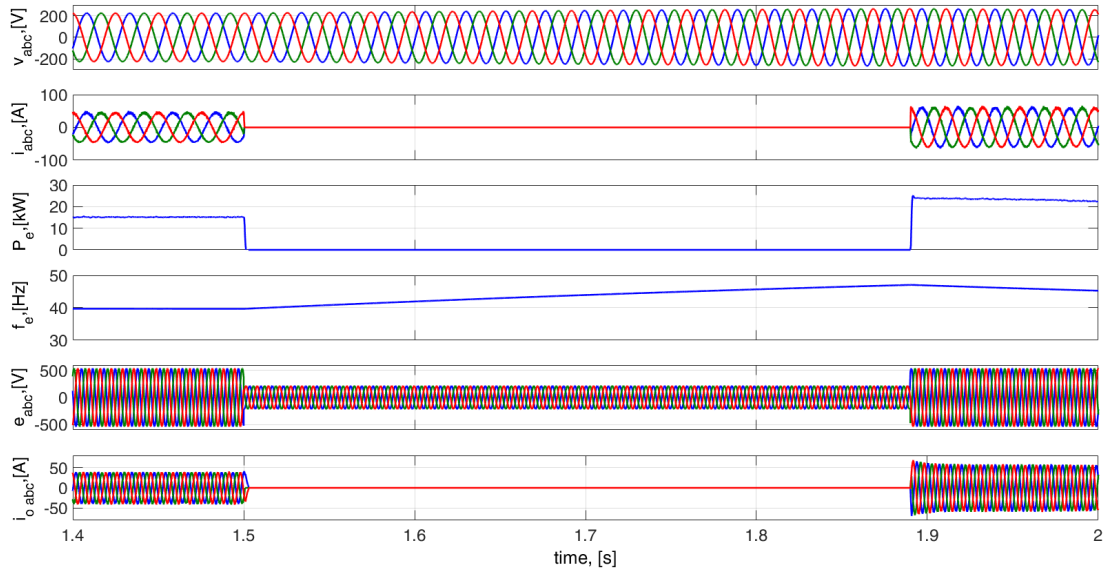


Figure 5.3: Zoomed-in view of the simulation results shown in Fig. 5.2

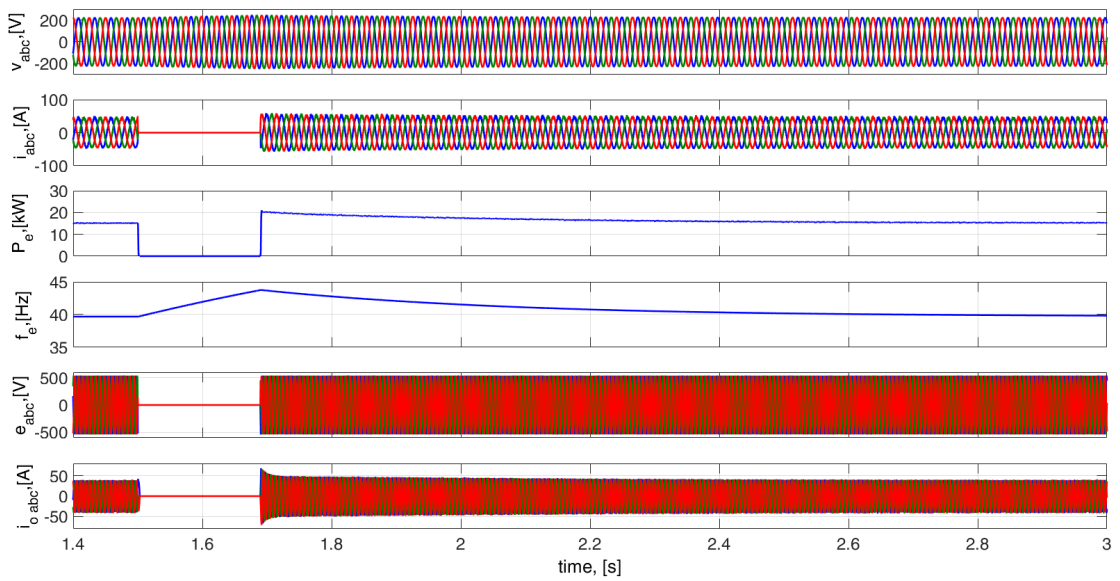


Figure 5.4: Simulation results of a LVRT test of $0\%V_n$ amplitude and duration 190ms: from top to bottom: generator voltages v_{abc} , generator currents i_{abc} , generator power P_{gen} , generator output frequency f_e , grid voltages e_{abc} and grid currents i_{oabc}

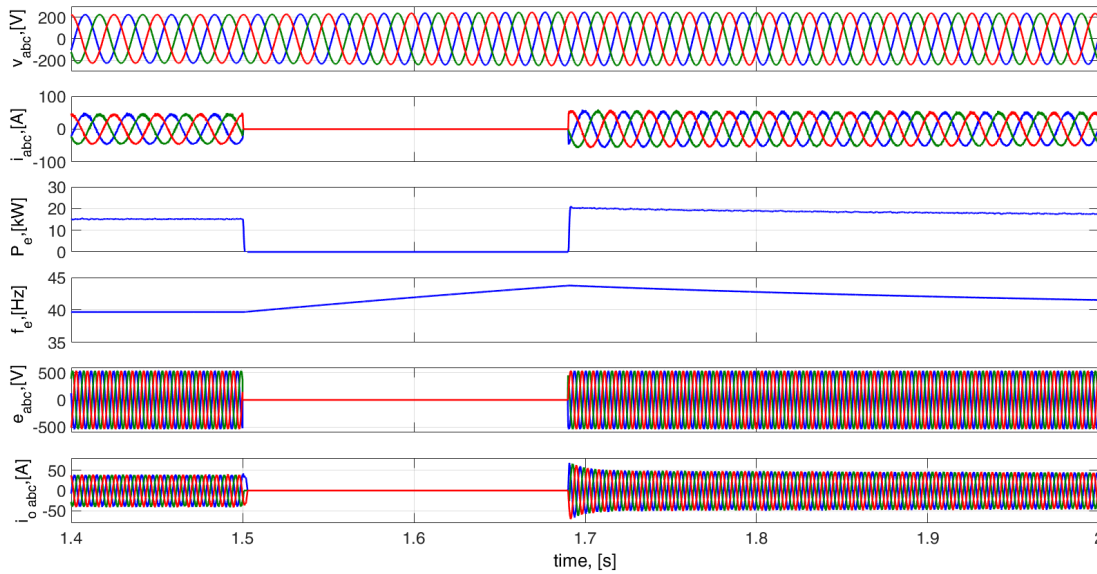


Figure 5.5: Zoomed-in view of the simulation results shown in Fig. 5.4

ends before 200ms, the WEC is allowed to stop injecting current into the grid but its disconnection from the grid is not permitted. Accordingly, the WEC output currents drop to zero during the voltage sag and restart being injected into the grid afterwards. Similarly to the previous test case, the WT experiments a speed increase during the voltage sag, caused by the unbalance between the rotor and generator torques, that is, on its hand, caused by the ceased power absorption from the generator by the WEC. As the voltage sag length is halved as compared to the test in Fig. 5.2, the WT speed experiments a less evident increase of 10.7% .

In Fig. 5.6 a 45% V_n voltage sag with duration of 390ms is applied to the WEC grid side during its normal operation. In this test the pitch angle controller reference rotation speed is set to 165rpm. The WT rotation speed immediately before the voltage sag is 159rpm. Thus, the pitch angle controller starts regulating the turbine speed just after the voltage sag is applied. As the WT speed increases the pitch angle controller increases the blades pitch angle, in order to limit the rotor speed to its reference value, as shown in the zoomed view of Fig. 5.7 provided in Fig. 5.6. From 1.55s to 1.95s, the blades pitch angle is increased almost linearly from 0° to 4°. This proves the pitch angle actuator drive is working at its maximum speed of 10°/s.

In this simulation, the pitch drive system reacts to the 400ms voltage sag, limiting the WT overspeed to 18.8% t. Compared to the simulation of Fig. 5.4 the overspeed is not substantially reduced. This happens because the pitch drive response time is too slow to react immediately to a 400ms voltage sag.

As the voltage sag ends, the WEC restarts absorbing active power from the PMSG. The increased generator frequency causes the WEC lookup table to force the i_q refer-

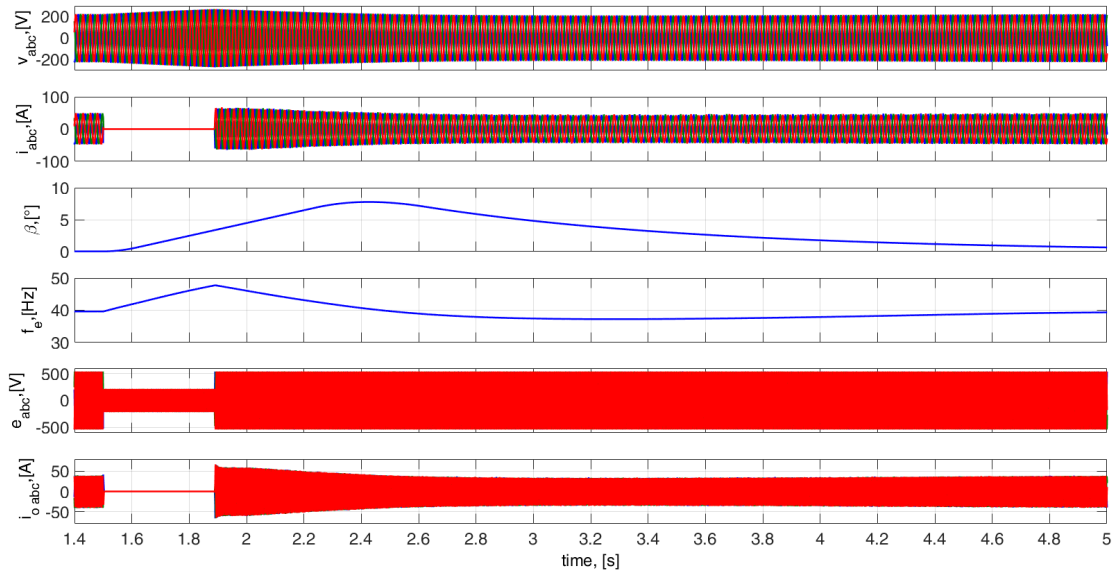


Figure 5.6: Simulation results of a LVRT test of $45\%V_n$ amplitude and duration 390ms with the pitch angle controller reference speed set to 165rpm. From top to bottom: generator voltages v_{abc} , generator currents i_{abc} , blades pitch angle β , generator output frequency f_e , grid voltages e_{abc} and grid currents i_{oabc}

ence value to higher values. For this reason, the generator torque is higher than the WT one, causing the WT speed to decrease. At the same time, the pitch angle controller reacts decreasing the pitch angle until the equilibrium condition preceding the voltage sag is reached again.

Finally, in Fig. 5.8, a voltage sag of $45\%V_n$ is applied for 8s. In this situation the WEC is allowed to be disconnected from the grid. In this test the pitch angle controller reference voltage has been set to 165rpm. As shown in Fig. 5.8, when the voltage sag happens, the WEC stops injecting current into the grid and the WT starts, gaining speed. Consequently, the pitch angle increases the blades pitch angle to regulate the WT rotation speed to its reference value. During the transient, the WT rotation speed reaches a peak speed of 216rpm, experiencing an overspeed of 35%. After 7s the transient can be considered ended, the pitch angle controller limits the WT rotation speed to 165rpm by pitching the blades to an angle of 16° . Remarkably, this simulation highlights the role of the pitch angle controller during the disconnection of the WEC.

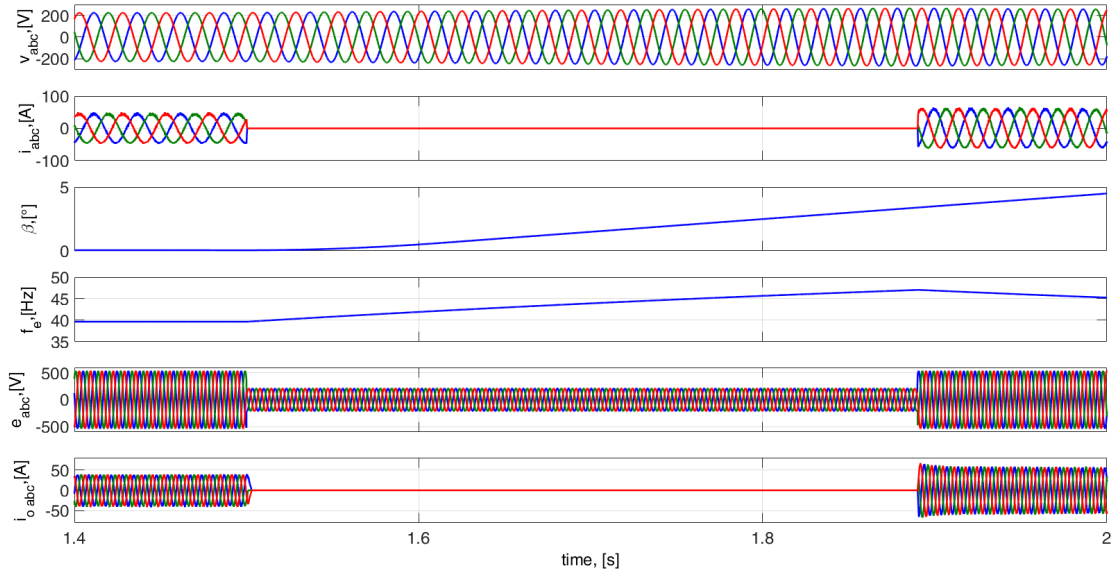


Figure 5.7: Zoomed-in view of the simulation results shown in Fig. 5.6

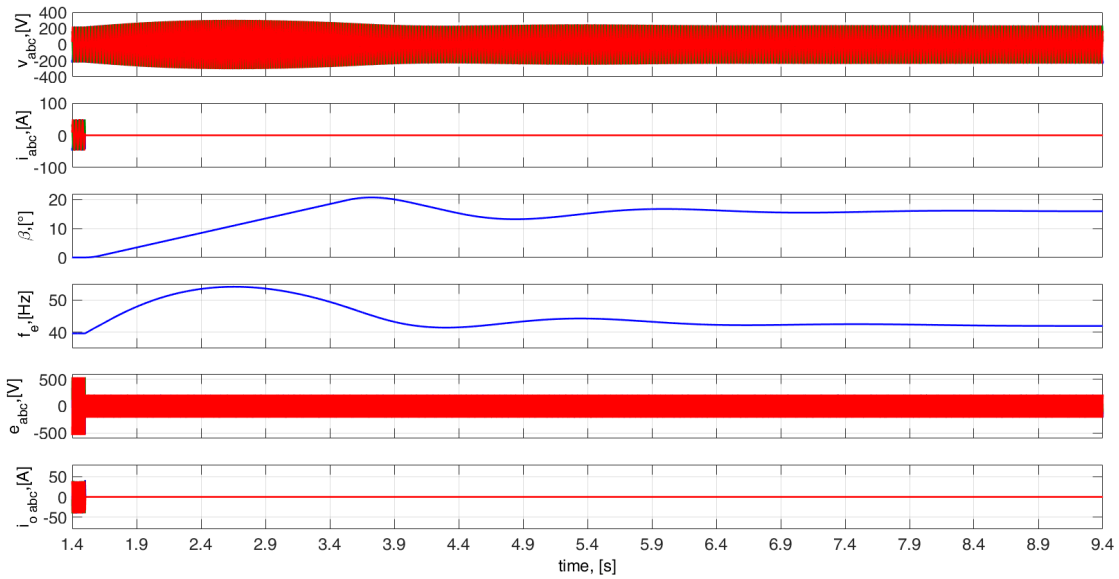


Figure 5.8: Simulation results of a LVRT test of $45\%V_n$ amplitude and duration 8s with the pitch angle controller reference speed set to 165rpm. From top to bottom: generator voltages v_{abc} , generator currents i_{abc} , blades pitch angle β , generator output frequency f_e , grid voltages e_{abc} and grid currents i_{oabc}

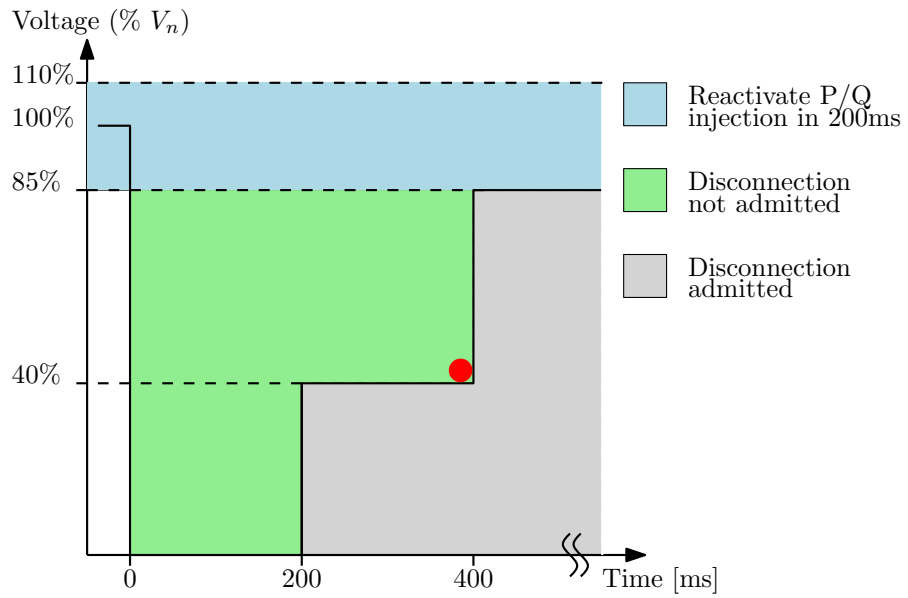


Figure 5.9: Voltage sag amplitude and duration indicated by the red circle in the grid code voltage profile area [17], conditions used to perform the LVRT test in Fig. 5.2

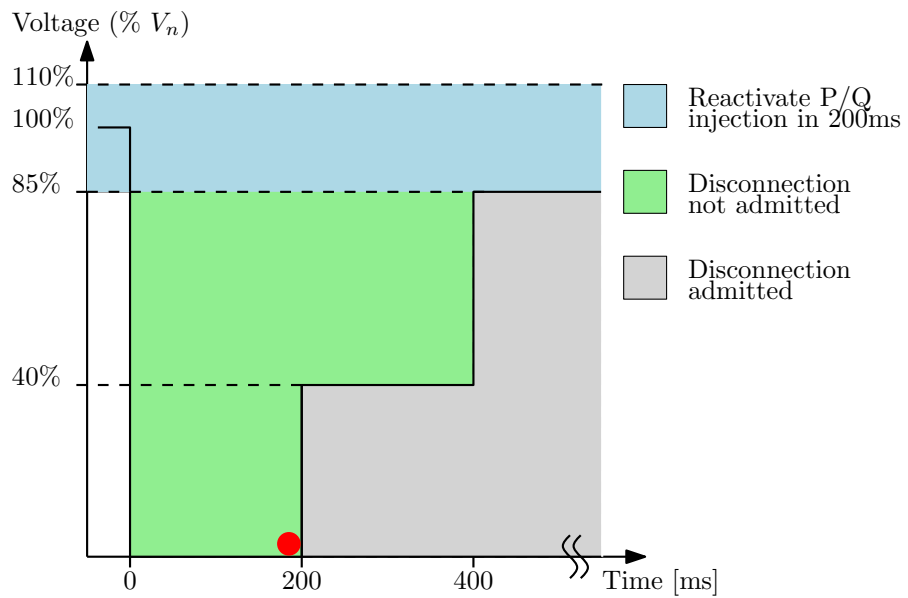


Figure 5.10: Voltage sag amplitude and duration indicated by the red circle in the grid code voltage profile area [17], conditions used to perform the LVRT test in Fig. 5.4

Part III

DESIGN AND REALIZATION

TEST BENCH DESIGN

6.1 INTRODUCTION

The test bench structure can be divided in 3 main blocks, highlighted in fig. 6.1:

- Wind turbine emulator
- Device under test (DUT), that is, herein, a wind energy converter
- Voltage sag emulator

The wind energy converter under test is connected between the WT emulator and the voltage sag emulator, both connected to the power grid. The power absorbed by the WT emulator from the grid is delivered to the WEC, which converts it from the PMSG emulator variable frequency and amplitude voltages into the currents to be injected into the grid. The grid emulator is a bidirectional back to back electronic converter driven as a voltage source at the WEC side and as a current source in the grid side. The voltage sag emulator delivers to the grid the power absorbed from the WEC.

As the power absorbed from the grid by the WT emulator is reinjected into the same grid by the voltage sag emulator, a power recirculation occurs through the test bench to the grid, as highlighted in Fig. 6.1. Therefore, the power dissipated by the test bench is only a small part of its circulating power and corresponds to the losses of the power converters employed to implement the WT and grid emulators.

The schematic depicted in Fig. 7.7 represents the test bench designed, implemented and studied in this thesis work. In Fig. 7.7 the connection between all components are represented in detail. The WT emulator is the most complex device of the overall system; it is composed by the following main sub-systems:

- Controllable power supply (amplifier)
- Isolation transformer
- External inductances
- Sensing board
- Real time platform

In the next sections the test bench parts and the WT emulator components are described in detail.

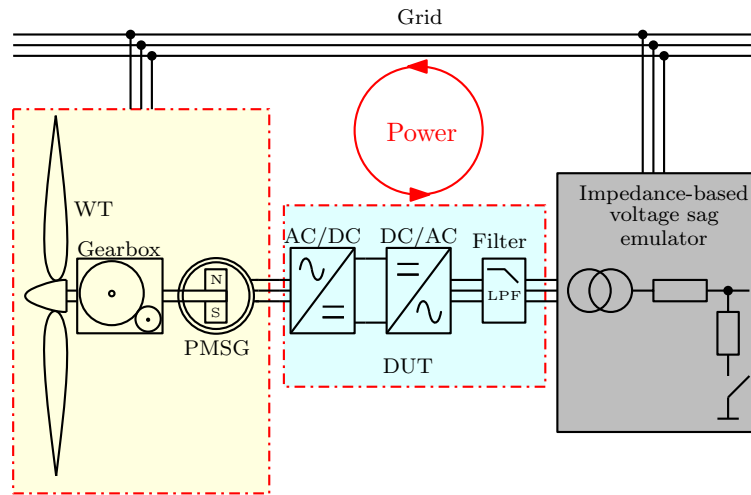


Figure 6.1: Reference test bench structure

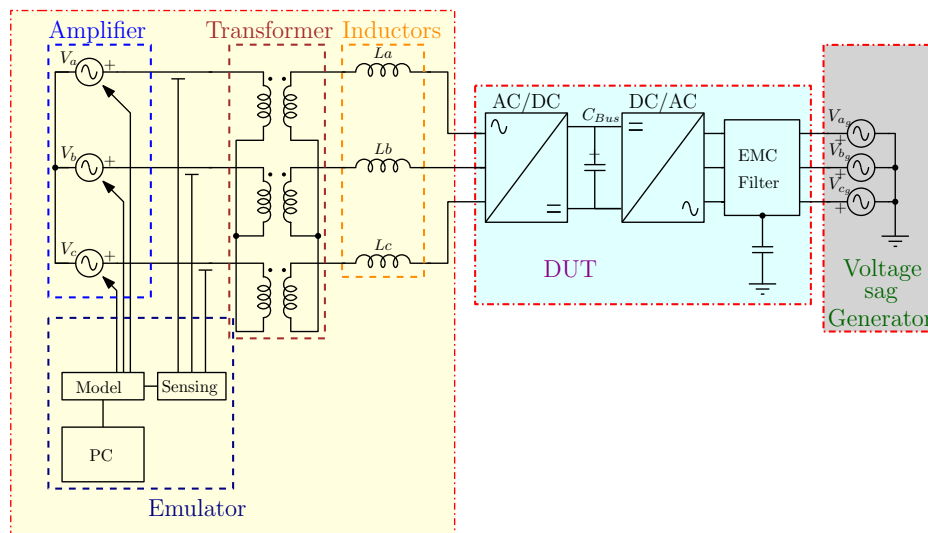


Figure 6.2: Proposed test bench implementation

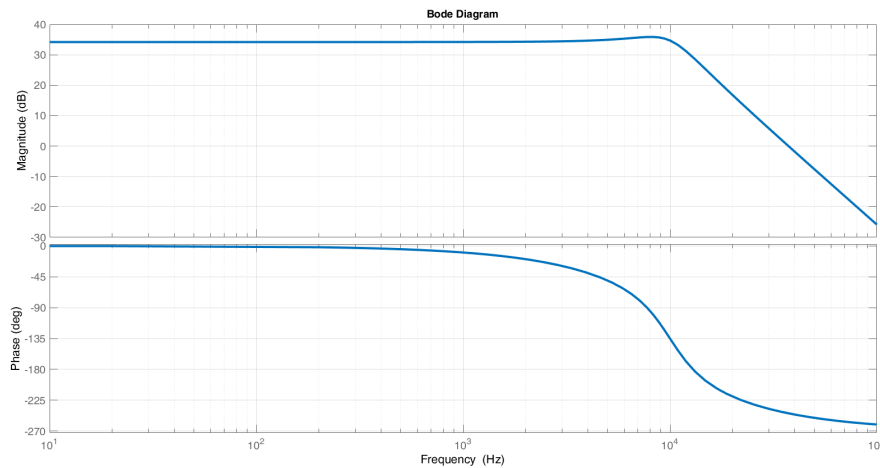


Figure 6.3: Controllable power supply transfer function

6.2 CONTROLLABLE POWER SUPPLY

The controllable power supply adopted to realize provide the implemented WT emulator power is a high bandwidth bidirectional three phase inverter in which every output voltage is controllable and isolated. Every output can reach a peak voltage of $\pm 600\text{V}$ and can be independently driven by an analog signal accessible via BNC connectors. The amplifier transfer function, G_{amp} , reported in Fig. 6.3, shows a DC gain $k_{\text{dc}} = 51$ between the analog inputs and the power outputs, with a cutoff frequency measured at -3dB equal to $F_{\text{amp}} = 13.5\text{kHz}$.

Each output is internally protected against overcurrents, and each output can deliver 10kW for a total delivered power of 30kW on the three outputs. The amplifier gain deviation from the DC gain has been measured and reported to be less than 1% in a 2kHz bandwidth. As the WT generators frequency usually does not exceed 200Hz the amplifier distortion can be considered negligible in to reproduce the emulated PMSG output voltage waveforms.

In those cases where the controllable power gain error is greater, to archive better precision a voltage feedback loop can be implemented by using a voltage sensing board connected to the emulator ADCs.

Moreover, every output offset can be finely calibrated separately by three additional analog inputs. A voltage offset regulation routine has been programmed in the real time hardware to finely calibrate the amplifier DC output.

6.3 ISOLATION TRANSFORMER

Although the amplifier output is isolated, an EMC capacitor C_{EMC} is connected between each output and ground, as shown in Fig. 6.5. The WEC normal switching

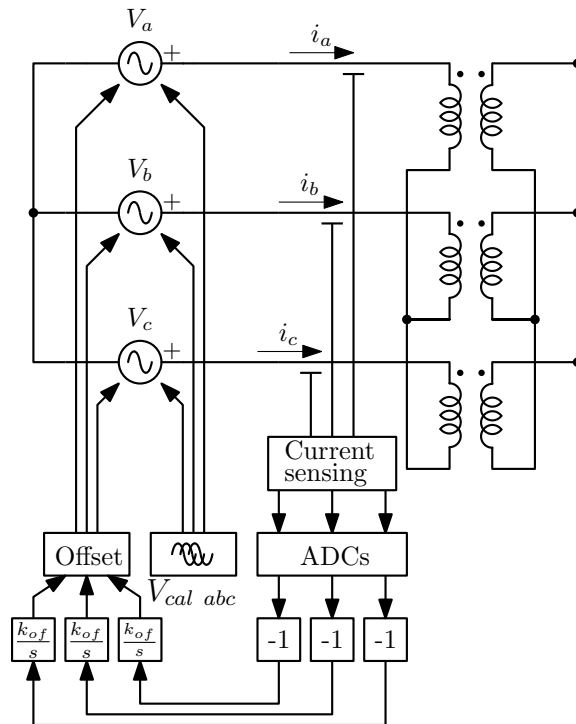


Figure 6.4: Block schematic of the offset voltage calibration routine for the controllable power supply

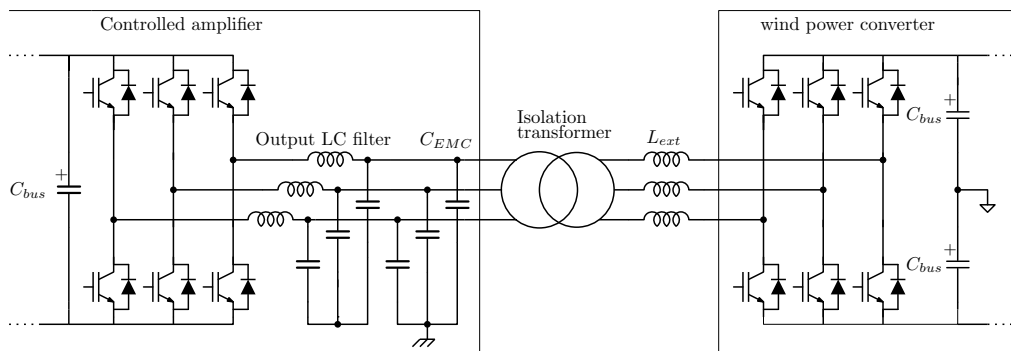


Figure 6.5: Simplified schematic of the amplifier to WEC interface

operation would produce dangerously high common mode currents through the EMC capacitors C_{EMC} , which is detrimental for their reliability and lifetime. Due to this reason an isolation transformer is needed to decouple the WEC from the controllable power supply output, as shown in 6.5. The transformer has been designed and built to withstand a nominal power of 30kW at a nominal voltage of 400V RMS. The transformer saturation current is 61A.

Driving a transformer with a voltage over frequency ratio V/F higher than the transformer nominal one can lead the transformer core to saturate, in case the magnetic flux density exceeds the core saturation limit.

As the PMSG output voltage amplitude is proportional to its rotation speed, the generator V/F ratio is constant over all its rotating speed range. Therefore, transformer saturation can be avoided by designing the component to properly operate at the PMSG nominal speed and output voltage amplitude.

On the other hand, as the amplifier outputs are directly connected to the isolation transformer, even a small voltage offset can cause large DC offset currents on the DC resistance of the primary windings; depending on the current offset magnitude the produced DC flux could lead the transformer to saturate.

A precise method to calibrate the amplifier offsets consists in deliberately saturating the transformer by driving it with low frequency three phase voltages. More precisely, if the voltage over frequency ratio V/F is high enough, the AC magnetic flux magnitude causes the transformer to saturate.

As shown in Fig. 6.6, if the transformer secondary is not loaded and if the DC current offsets on the primary windings are near to zero, the primary current waveforms present symmetrical spikes due to transformer saturation; their magnitude depends on the primary voltage amplitude and frequency. On the other hand, a DC current offset causes the transformer to saturate asymmetrically, as shown in Fig. 6.7. In fact, the DC flux sums to the AC one, forcing the transformer to saturate harder in the direction of the DC offset.

This property can be used to finely adjust the amplifier DC voltage offsets. As shown in Fig. 6.4, a calibration routine drives the controllable power supply to generate the low frequency, three phase voltages $V_{cal\ abc}$ employed to cause transformer saturation. The current waveforms are consequently acquired by the sensing board, converted by the ADCs and processed by the emulator. The digital representations of the measured currents are inverted and fed into a discrete integrator driving the DAC connected to the amplifier offset regulation inputs.

This system integrates the difference between the positive and negative spikes, increasing the amplifier voltage offset if the difference is negative and decreasing it if the difference is positive. In other words, a negative loop drives the amplifier voltage offsets to zero by forcing the AC saturation current to be symmetrical.

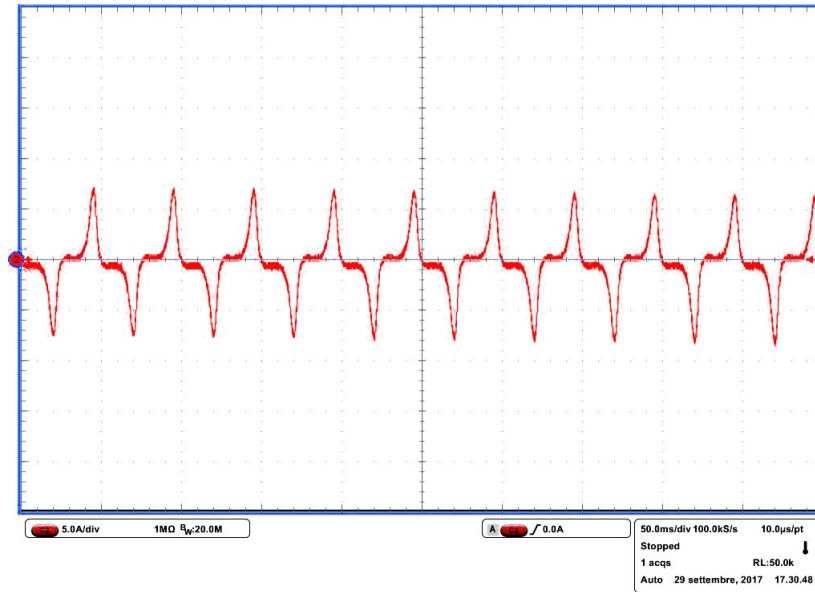


Figure 6.6: Transformer driven to symmetrical saturation using a 75 V_{pp}, 10Hz sinusoid. Amplitude scale 5A/div, timebase 50ms/div

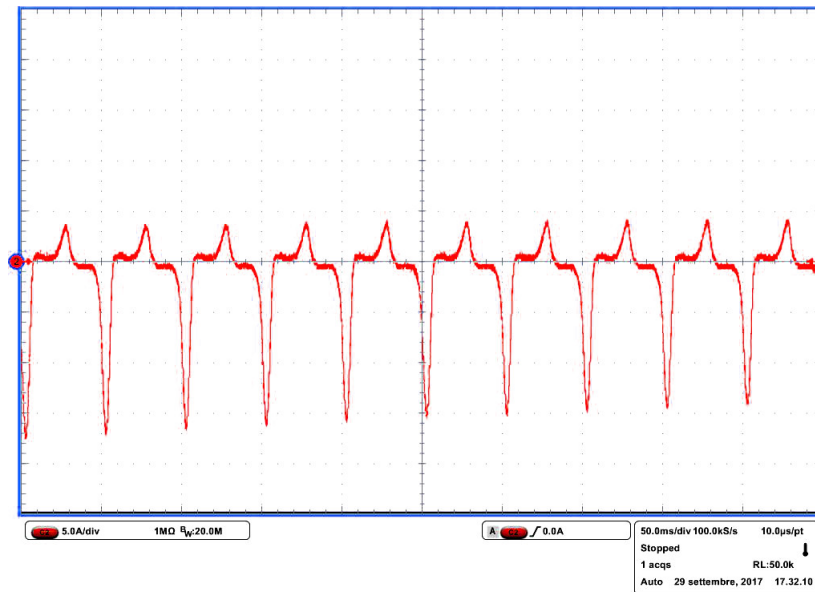


Figure 6.7: Transformer driven to asymmetrical saturation using a 75 V_{pp}, 10Hz sinusoid with a -250mV offset. Amplitude scale 5A/div, timebase 50ms/div

6.4 EXTERNAL INDUCTANCES

In typical electric drive applications, generators and motors are directly connected to the switching bridges of the electric converters. In this application, the capacitors of the amplifier output LC filter would be subjected to high dV/dt voltage variations caused by the WEC normal switching operation. This would cause high currents on the filtering capacitors, which makes a direct connection between the amplifier and the WEC not possible. Therefore, the external filtering inductances L_{EXT} , shown in Fig. 6.5, are mandatory to limit the currents derivatives.

If the generator to be emulated is a non salient pole generator, the choice of an external inductance similar to the generator output inductance would allow the physical emulation of the generator inductive behavior. As a 30kW non salient pole PMSG usually presents an inductance value between 2mH and 6mH, a 4mH filtering inductance has been chosen and realized by using 2mH inductances connected in series two by two. Three 4mH inductances has been inserted between the controllable power supply and the WEC. The inductances has been designed for a saturation current of 70A.

To add flexibility in the PMSG inductance emulation, the WT emulator has been programmed to simulate an inductive behavior on the generator output. This can be archived by including a current loop in the u_{abc} generator output voltages equation, where the current sign is expressed in the generator convention, i.e. , exiting the generator output terminals, as shown in Fig. 6.4:

$$\begin{aligned} u'_a &= u_a - L_{ema} \frac{di_a}{dt} \\ u'_b &= u_b - L_{emb} \frac{di_b}{dt} \\ u'_c &= u_c - L_{emc} \frac{di_c}{dt} \end{aligned} \quad (6.1)$$

where L_{ema} , L_{emb} and L_{emc} are the emulated output series inductances. Alternatively, to emulate a non salient pole generator behavior, the effect of the generator inductances can be expressed in dq reference frame, as in (7.1). This solution allows to add a simulated inductance to the physical one connected between the isolation transformer and the WEC, which enables to emulate a wider range of inductance values.

In this case the equations of the PMSG are expressed as:

$$\begin{aligned} u_d &= L_d \frac{di_d}{dt} + R_s \cdot i_d - \omega_e \cdot L_q \cdot i_q \\ u_q &= L_q \frac{di_q}{dt} + R_s \cdot i_q + \omega_e \cdot L_d \cdot i_d + \omega_e \cdot \Psi_f \end{aligned} \quad (6.2)$$

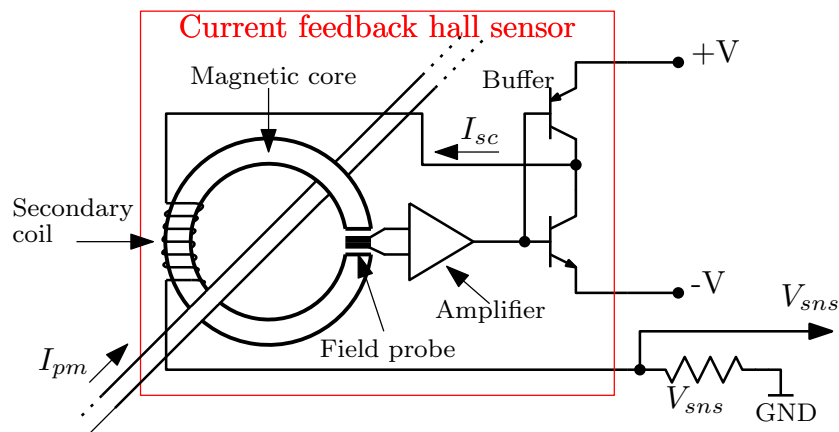


Figure 6.8: Closed loop hall sensor block diagram

6.5 SENSING BOARD

A sensing board has been designed and realized to measure the emulated three phase generator output currents. The current sensing has been realized by using the LEM LA150-P closed loop hall sensors to obtain an isolated measuring system.

The chosen sensor features a closed loop active circuit generating a compensation current in a secondary coil to balance the flux generated by the sensed current in the core.

Hall sensors consist of a magnetic core picking up the magnetic field generated by the measuring current and directing it into a field probe. The probe output current signal is proportional to the measured current; it is conditioned, fed into an amplifier and buffered. As shown in Fig. 6.8, in closed loop hall sensors the buffer output current I_{sc} is used to drive a secondary coil wound on the magnetic core. The secondary current I_{sc} generates a flux on the core equal and opposite to the flux created by the measured current I_{pm} , driving the total flux to zero. The compensating current I_{sc} is also used to obtain the output signal V_{sns} by using an external resistor R_{sns} . As the magnetic core works constantly in zero flux conditions, the non-linearities and the temperature drift that are typical in hall sensors are therefore compensated, but the output offset remains. Therefore a calibration routine on the ADCs is needed to compensate for the hall sensors offsets at the emulator start up.

The advantages of a closed loop hall current sensor over open loop ones:

- Wider frequency range
- Lower gain drift over temperature
- Faster response time
- Better linearity

- Better overall accuracy
- Better immunity to electrical noise

As the cutoff frequency of the analog conditioning circuitry is dimensioned to 350kHz, the measuring system is given by the hall sensor cutoff frequency, which is $F_{sns} = 150\text{kHz}$.

An additional voltage sensing circuit added to measure the amplifier output voltages. Every voltage sensing circuit is based on three operational amplifiers connected in the instrumentation amplifier configuration. The voltage sensing is used for protection purposes; in the emulator code a safety routine checks the amplifier output voltages and shuts down the system if the measured amplitudes are greater than the expected value. Moreover, the voltage sensing can be used to implement a closed loop control to improve the precision of the generated voltages.

Each sensing circuit output includes a 50Ω output resistance to match the coaxial cables impedance used to connect the sensing board with the emulator board. Finally, the sensing board has been mounted inside a metallic box in order to reduce noise, being only the hall sensor outside, as shown in Fig. 6.10. The measuring system schematic is shown in Fig. 6.9.

6.6 REAL TIME HARDWARE

Real time simulation can be a very useful technique in a very wide spectrum of engineering processes. In a power electronics design, if used in conjunction with hardware in the loop (HIL) or power hardware in the loop (PHIL) techniques, it can significantly reduce the design and debug phases during a project development. More specifically a HIL simulator is based on a simulation software used to program a model on a hardware platform performing, at the pace of the wall clock time, all the required calculations and electrically interfacing with the external world through A/D and D/A converters or digital communication interfaces.

This technique is used very often in research and development field due to its extreme versatility. HIL allows to individually test multiple parts used in a larger system without necessarily connecting them to their real counterparts.

In this thesis HIL is used to implement the emulated WT system driving the controllable power supply. The real time hardware is programmed to simulate every single part of a WT. The WT emulator needs a HIL simulation system capable of high processing speed, fast and low latency inputs and output interfaces, such as ADCs and DACs to reduce input acquisition time T_{acq} , output update time T_{upd} and jitter.

A real time system has to perform every cyclic operation in a fixed time T_s , called time step. In other words a time schedule has to be strictly observed, as depicted in Fig. 6.11 to let the emulation operate at a fixed simulation frequency $F_s = \frac{1}{T_s}$. The real

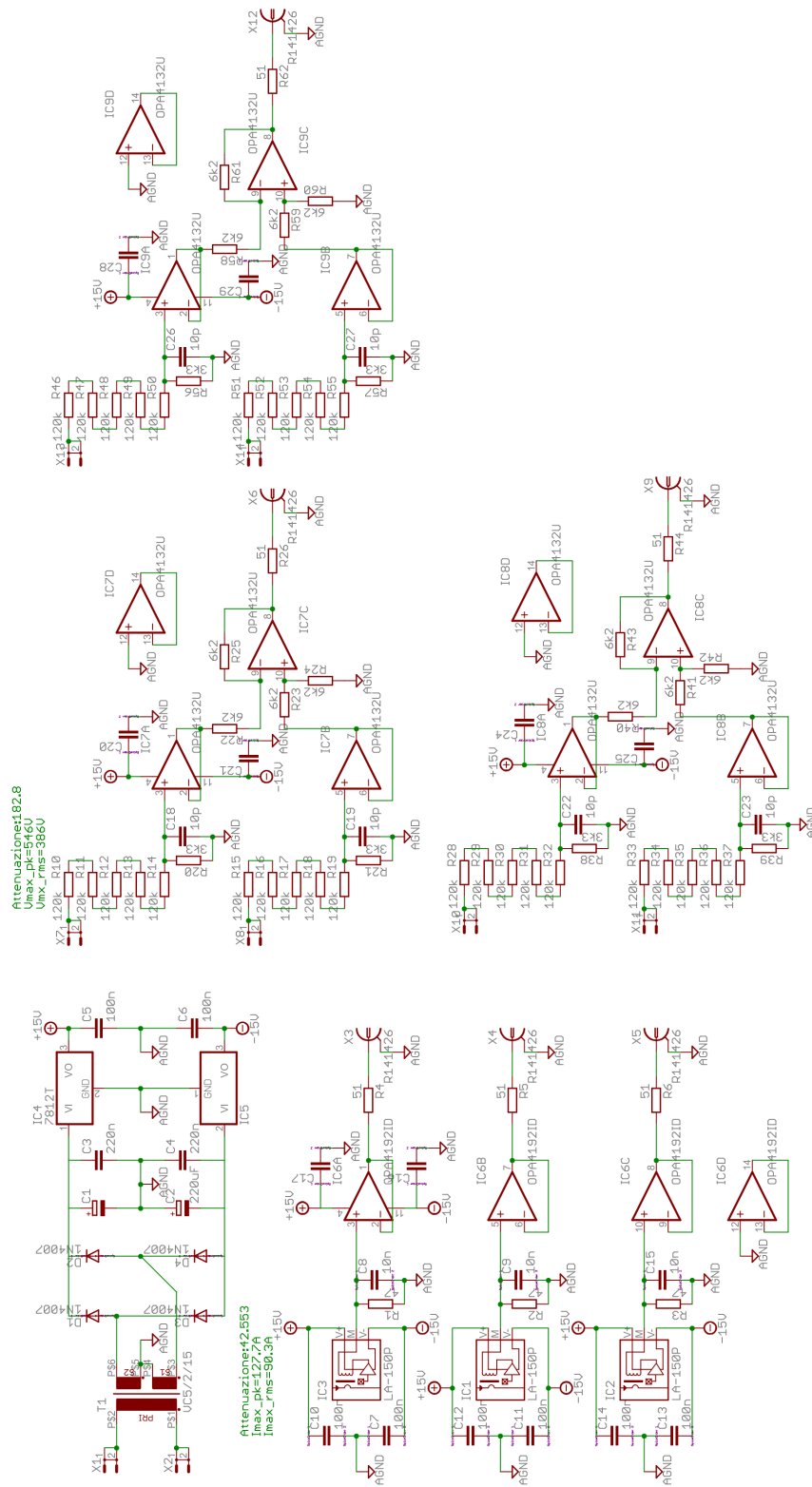


Figure 6.9: Schematic of the current sensing board

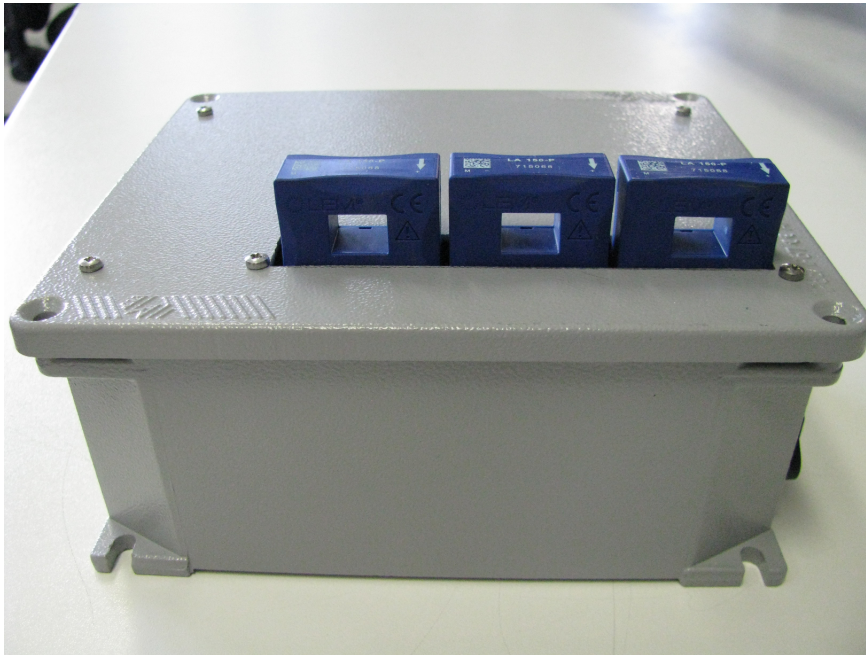


Figure 6.10: Current sensing board realization

time property of a processing system is not bounded to its calculating power or speed, the only requirement is to complete all the operations in a fixed time window.

To implement the WT emulator a high speed real time system is needed to finely describe the output waveforms. A real time system can be obtained by using any hardware platform where a rigid operation time scheduling is possible. For example, it is not possible to obtain a real time system if the platform software is based on a regular operating system where time scheduling is not accessible and depends on the system tasks and computational load. Multiple real time hardware platforms has been compared to understand their potentials and performances. The comparison has been based on the following aspects:

- Computing power
- Programming language
- Input variables acquisition time
- Output variables update time
- Hardware reliability
- Costs

There are plenty of real time hardware solutions available on the market. Some of them rely on an external simulation software, as Matlab Simulink, as programming

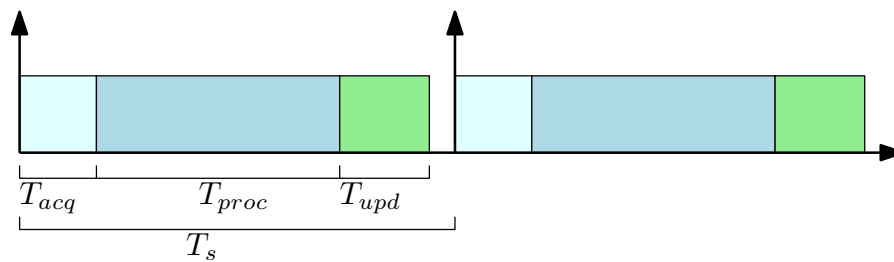


Figure 6.11: Real time system time schedule

language, other are based on its own development environment, others on standard programming languages such as C or C++. Real time simulators can also be obtained by using low level programming languages to program microcontrollers in order to obtain a rigid time scheduling. The following platforms has been compared :

- National Instruments cDAQ
- National Instruments cRIO
- Texas Instruments TMS320F28377S microcontroller

6.6.1 National Instruments cDAQ

National Instruments (NI) cDAQ platforms can be programmed using LabVIEW or C++ and can be operated using Linux real time operative system. Therefore it is possible to run parallel threads, operating with different priorities, automatically handled by the real time operative system. The cDAQ IO interfaces are modular and standardized so that they can be chosen among all the proposed NI solutions.

This platform can be both programmed by LabVIEW or C++ programming language. A study performed on the hardware platform revealed the time required to acquire the inputs and to update the outputs cannot be less than 35ms.

The test has been performed using the following hardware:

- NI cDAQ 9132, based on NI Linux real time operative system
- NI 9244, a four channels analog input module
- NI 9263, a four channels analog output module

A C application has been developed using the NI DAQmx 14.5.1 to evaluate the hardware platform latency. A maximum priority task has been created to sample an analog input with sampling frequency 25kHz, and, concurrently, to update the outputs. The acquired data are returned grouped in packets with a latency that, depending on the computational load, can range between 35ms and 200ms.

The cDAQ structure is made to acquire big moles of data and periodically transfer them in form of large packets. The cDAQ architecture is engineered to be an excellent data logger and post processor but it is not able to perform high speed real time processing. For this reason this platform is not suitable for the application considered herein.

6.6.2 National Instruments cRIO

The cRIO platform is based on an processor and a FPGA. Through a programmable user interface it is possible to control the simulation parameters from a computer connected to the cRIO through a local-area network (LAN). As in the cDAQ, the input/output interfaces can be chosen between the standardized modular NI solutions.

The embedded FPGA technically allows to obtain very low acquisition, processing and output update times. As a high update frequency is essential in this application, especially to implement the current control needed to simulate the generator inductances behavior, cRIO may represent a suitable solution to realize the WT emulator.

More specifically, a NI cRIO-9082 platform has been used to implement the simulation code. This platform is equipped with a dual core Intel i7-660UE processor. As shown in Fig. 6.12, the processor can be used for post processing, storing data on a 32GB SSD hard disk, driving a monitor through a VGA port, transmitting and receiving data over four USB 2.0 ports, two Ethernet interfaces, a RS-232 serial port, a RS-485/422 serial port and a MIX-Express port. The processor runs a Windows Embedded Standard 7 Runtime operative system. The operative system is not intended to perform high speed real time systems tasks as the operative system cycle time can hardly be driven under 500 μ s. For this reason, to implement high speed applications the Intel processor may be used to just supervise the elaboration performed on the FPGA.

In fact, the processor can be used as a bridge between a user interface running on a PC and the FPGA. The FPGA embedded in the cRIO-9082 is a Xilinx Spartan-6 LX150 featuring:

- 184304 flip-flops
- 92152 6 inputs lookup tables (LUTs)
- 180 DSP slices
- 4824 kbit RAM block
- 3 direct memory access (DMA) channels
- 32 logical interrupts

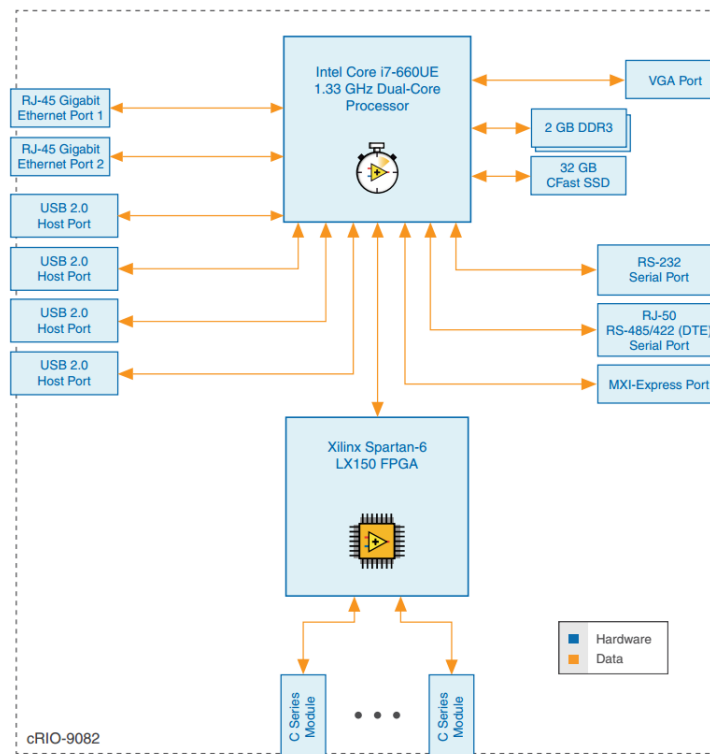


Figure 6.12: NI cRIO-9082 structure

The FPGA is used to manage the data acquisition, perform high speed calculations, update analog outputs and share data with the processor. As the FPGA is based on reconfigurable digital ports, it can take advantage of hardware parallelism to speed up the execution of the algorithms. In other words, the cells of an FPGA can be wired together to realize as many parallel processes, as the number of the cells into the FPGA and the processes complexity permits it. In NI cRIO hardware the high speed real time program has to be written in LabVIEW FPGA code, which is then translated in VHDL code to reconfigure the FPGA. Moreover, the FPGA has direct access to the I/O interfaces as shown in Fig. 6.12. Controlling the I/O peripherals at hardware level allows to minimize response times and latencies.

The platform has to be programmed using LabVIEW programming language and LabVIEW FPGA.

6.6.3 Texas Instruments TMS320F28377S microcontroller

A microcontroller (μC) usually is a processor combined with multiple hardware peripherals, implementing input/output interfaces, ADCs, DACs, digital ports, PWM modulators, and communications modules, such as the I²C and SPI protocols. Usu-

ally, to reduce costs, the processor calculation power is limited, as a μC main purpose is versatility in interfacing with the external world.

In digital signal processors (DSPs) the philosophy is inverted. As a DSP is intended to perform fast elaborations, it usually does not include any peripheral, in order to optimize processing power over costs.

In the actual market the edge between DSPs and μC s is becoming less evident and, in some cases, such as in the Texas Instruments (TI) C2000 family, there are some DSP like high performance μC s that integrate peripherals such as ADCs, DACs, PWM modulators, internal flash memory and communication interfaces such as UART, I²C and SPI, that are typical of μC s as well as advanced computing capabilities such as floating point ALUs, coprocessors, trigonometric and complex number calculator units, that are typical of DSPs.

More specifically, the TI LAUNCHXL-F28377S platform, based on the TMS320F28377S μC and shown in Fig. 6.13, has been evaluated. The TMS320F28377S, whose structure is shown in Fig. 6.14, features a 32 bit CPU operating with a clock frequency of 200MHz. To perform fast, advanced calculations on digital signals, the μC is equipped with a single-precision floating point unit (FPU), used to perform single-cycle instructions on floating point data. The structure of the FPU is based on a modified Harvard architecture, allowing instruction and data fetches to be performed in parallel, writing data and reading instructions in parallel, to maintain single-cycle instruction execution across the pipeline. This function is performed over six separate address data buses [76]. The C2000 family features a trigonometric mathematical unit (TMU) extending the capabilities of the FPU. The TMU is designed to speed up the execution of common trigonometric and arithmetic operations, enhancing the FPU instructions set to perform trigonometric calculations more efficiently. The TMU uses the same register set and flags of the FPU [76].

The Texas Instruments C2000 family includes a Viterbi/complex control unit (VCU), used to perform fast fourier transforms (FFTs) in 5 cycles with automatic saturation, rounding and scaling to maximize computation accuracy. The VCU can be used to compute complex numbers calculations and it may be used to implement complex filters. The VCU can perform multiplications between complex numbers and their coefficients in 5 clock cycles [74].

The TMS320F28377S features a programmable control law accelerator (CLA), an independent 32 bit floating point math processor for concurrent control loop execution. The low interrupt latency of the CLA allows to read ADC samples reducing significantly the ADC sample to output time. By using the CLA to process time-critical control loops the CPU is free to perform other operations in parallel. The CLA instruction set includes single-precision floating point math operations with parallel load and store, data type conversions, and conditional branch-and-call. The CLA has a separate memory to store the program, which can consist of up to eight tasks or interrupt service

routines. Interrupt routines can be connected to external interfaces such as ADCs and PWMs [77].

The μC is equipped with 512kB of Flash Memory and with 132kB of RAM. The available communication peripherals include USB 2.0, universal parallel port (UPP), two controller area network (CAN) modules, three serial peripheral interface (SPI) ports, two multichannel buffered serial ports (McBSP), four serial communication interfaces (SCI/UART) and two I²C interfaces.

Four multiplexed ADCs are available in two different operation modes and resolutions: the single-mode and the differential-mode. When the differential mode is selected the ADCs can operate at 1.1 MSPS with a resolution of 16 bits using up to 12 channels. On the other hand, if the single-ended input mode is selected the ADCs can operate at 3.5 MSPS with a resolution of 12 bits using up to 24 channels. The ADC peripheral is also equipped with a post-processing hardware interface, performing operations like offset removal, error from setpoint calculations and high, low and zero-crossing compare with interrupt capability. The analog subsystem also features eight windowed comparators with 12 bits digital to analog converters (DAC) driven references. Moreover, the μC is equipped with three buffered DACs outputs with a resolution of 12 bits.

Finally the TMS320F2837S μC features 24 PWM channels and 16 high resolution PWM modulators.

This μC can be used to implement a high-speed real-time hardware in the loop platform for the application considered in this work. First of all, the architecture using FLU and TMU allows to describe all the simulation data in floating point representation, allowing data math operations to be performed without risking arithmetic saturation. The extreme flexibility of the analog interfaces, the system speed and efficiency make this μC suitable to implement a real time hardware simulator.

6.7 CRIO PROGRAMMING AND TESTING

In the first part of the experimental design the NI cRIO-9082 RT platform has been used to inspect the system requirements in terms of speed and processing power. A NI-9215 four inputs, 16 bits, 100kS/s ADC module has been used to acquire the input currents signals from the sensing board. The module channels are isolated for safety, noise immunity and high common mode voltage rejection.

A NI-9263 four outputs, 16 bits, 100kS/s DAC module has been used to convert the permanent magnet digital representation in analog output control voltages. As both modules are isolated, no additional signal conditioning is required.

The computer user graphic interface has been programmed using LabVIEW. The user interface, shown in Fig. 6.15, allows to visualize the main data during the WT simulation and to set the parameters of the emulation system.

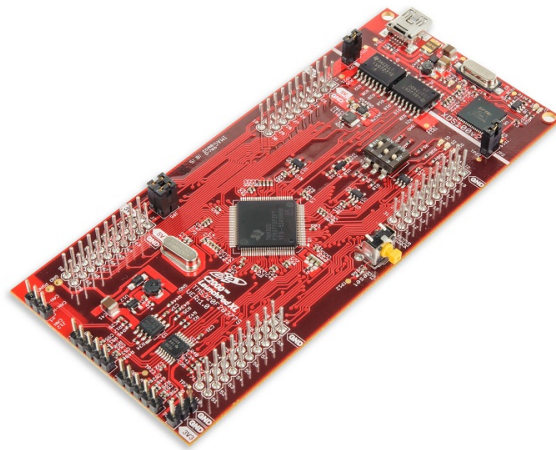


Figure 6.13: Texas Instruments LAUNCHXL-F28277S

In Fig. 6.17 a screenshot representing the LabVIEW code is reported. Many parts of the emulation program has been reduced in submodels to tidy up the code, make it more readable and simpler to debug.

Most of the digital signals used in the simulation are described in fixed point representation. Their digital resolution has been carefully chosen to obtain a trade-off between resolution and hardware capability. More specifically, high resolution signals processing costs more in terms of FPGA cells than low resolution ones. As the simulation program has proven to be very complex and expensive in terms of digital hardware usage, the data representation of the entire structure has to be optimized. Moreover, the design of every arithmetic operation must take into account of possible arithmetic saturation.

The final implementation has been able to perform a processing cycle in a fixed time of $17\mu\text{s}$. Large part of this time window is dedicated to the A/D conversion. This is the main limit of this implementation as only $5\mu\text{s}$ are required by the FPGA to perform all the calculations, the remaining time $12\mu\text{s}$ are needed by the ADC to convert analog signals into digital data. This limits the cycling frequency to 58kHz , if higher speed is needed, faster ADC modules should be used. For example the NI-9223 module presents four channels, 16 bits, 1 MSPS analog to digital convertes.

As the FPGA is basically a programmable digital hardware circuit, parallel routines can be programmed to perform parallel operations. The DAC module takes almost $9\mu\text{s}$ to be updated, so a parallel routine has been programmed to be able to not further increase the time step T_s . As shown in Fig. 6.16, the DAC outputs are continuously updated with the last value computed by the main processing routine. As shown in Fig. 6.16, the time lapse T_{ur} between the parallel routine update and the DAC output update is always larger than the DAC update time $T_{up,d}$. As a matter of fact

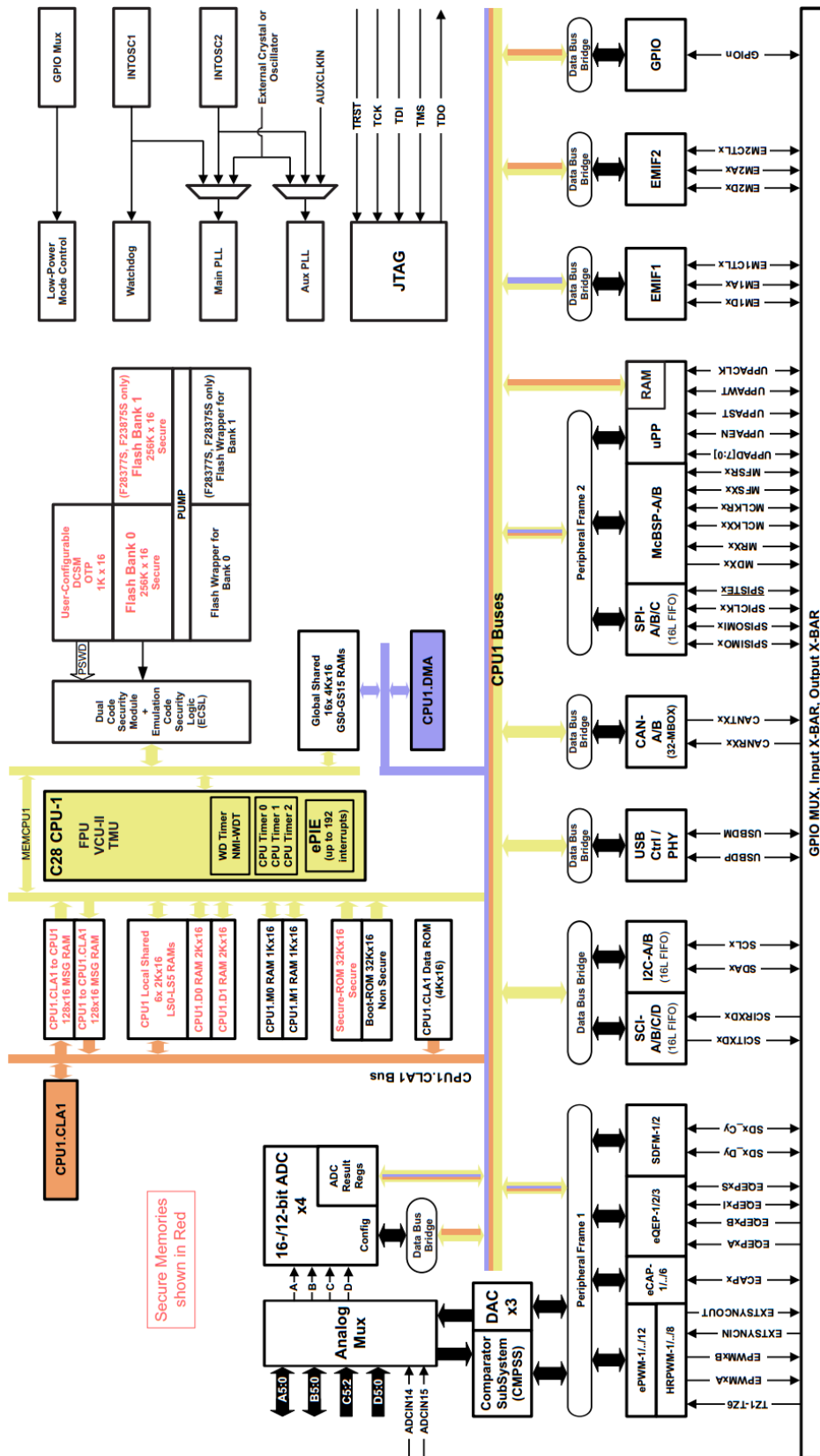


Figure 6.14: Texas Instruments TMS320F28377S μ C internal structure

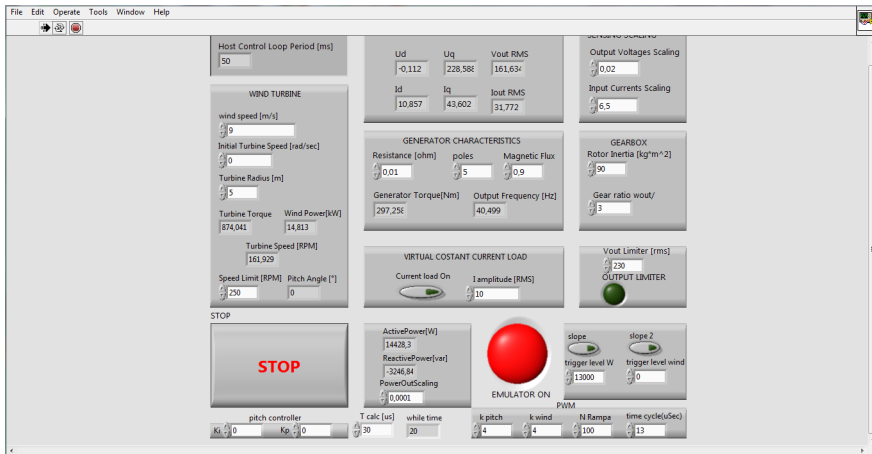


Figure 6.15: Emulator graphical user interface developed under LabVIEW

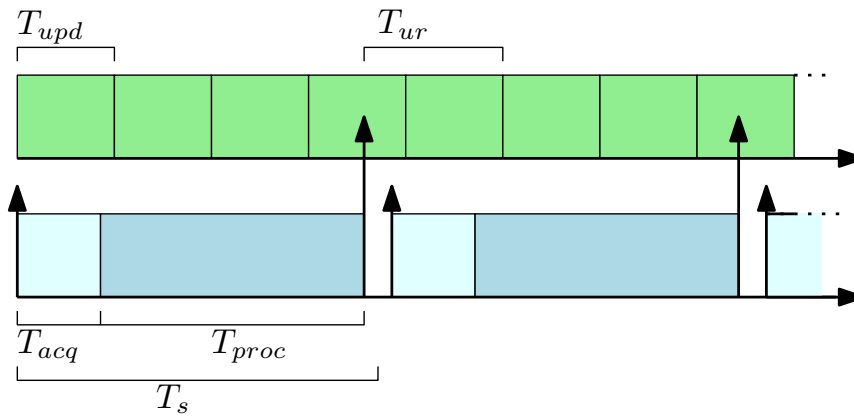


Figure 6.16: cRIO time scheduling

depending on when the parallel routine is updated, T_{ur} can be as large as twice T_{upd} . This happens because the DAC routine waits for the DAC end of conversion before starting a new conversion. As there is no correlation between the DAC conversion time and the total simulation time step T_s , a jitter of amplitude T_{ur} is obtained. In other words, the emulation routine runs with a time step of T_s but the delay between the inputs acquisition and the outputs update varies between $T_s + T_{upd}$ and $T_s + 2T_{upd}$. This jitter, depending on the application, can be unacceptable. For example, if a high speed output current loop has to be realized, this jitter can add a delay that can result in system instability.

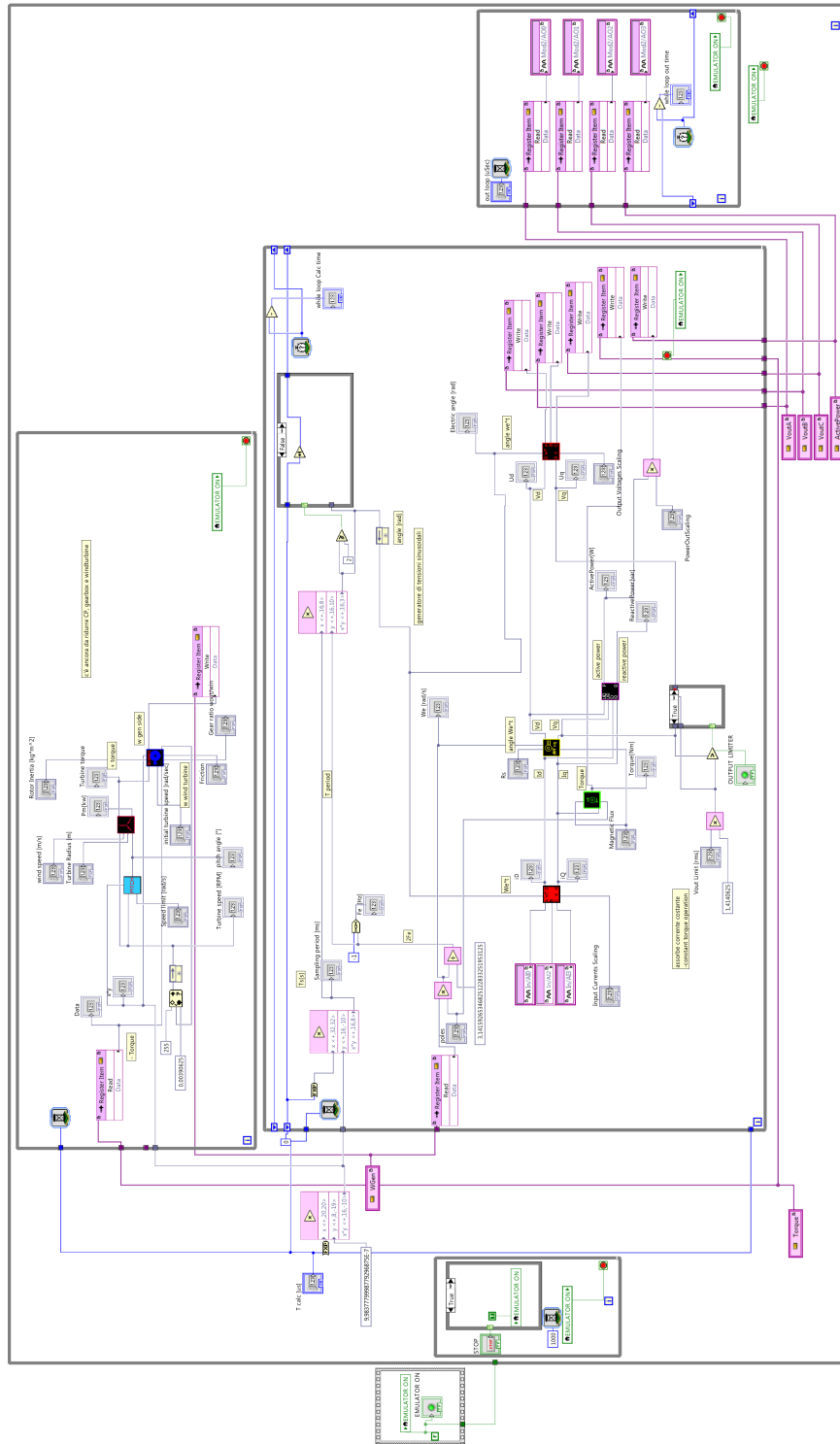


Figure 6.17: Main LabVIEW FPGA code, including analog signal acquisition, data processing and outputs update

6.8 TI LAUNCHXL-F28377S PROGRAMMING AND TESTING

A second real time hardware implementation has been designed using the TI LAUNCHXL-F28377S board. As the μC is a serial processing device the time scheduling is similar to the one depicted in Fig. 6.11. The emulation program sequentially performs:

- analog acquisition in T_{acq}
- data processing in T_{proc}
- DAC update T_{upd}

An additional conditioning board is required to adapt the measured signal to the $0 - 3\text{V}$ range of the ADC. Moreover, instead of using the μC internal 12 bits μC DAC, a 16 bits, 8 channels external DAC has been added to obtain a better resolution for the voltage signal driving the controllable power supply. The μC controls the external DAC by means of an SPI communication port.

An output conditioning circuit has been designed to adapt the $0 - 3\text{V}$ DACs outputs to the $\pm 12\text{V}$ of the controllable power supply inputs. Three of the DAC outputs has been used to control the amplifier output voltages, other three to control its offset calibration. The remaining two DAC outputs has been used for debugging and simulation variables monitoring purposes.

A six channels conditioning circuit has been designed to filter the input signals from the sensing board and to adapt them to the ADC voltage range and offset. Protection circuits has been included both at the input and at the output of the conditioning circuit. This ensure protections for safe voltage levels for the operational amplifiers and the μC ADCs. The input impedance of the conditioning circuits has been dimensioned to 50Ω to adapt the impedance between the sensing board, the coaxial cable and the emulator board.

The schematic of the conditioning board is shown in Fig. 6.19. An isolated power supply has been designed as well to power both the TI board and the conditioning board. The μC program has been structured to be easily modified, replaced and debugged. A system timer has been programmed to launch an interrupt when its counter reaches a precise value. This interrupt calls the main simulation routine to convert analog input data, process the simulation models and update the system outputs.

To control the WT emulator a graphical user interface (GUI) has been programmed by using C++ and QT cross platform software, shown in Fig. 6.18. On the μC the data communication routine uses the UART serial interface and a serial-to-Ethernet converter module to exchange data with teh PC running the GUI. The C++ program running on the PC implements the Ethernet communication routines to exchange data with the μC and the display visualizing the simulation parameters.

The first version of the board took, in the worst case, a step time $T_s = 39\mu\text{s}$ to perform an analog to digital conversion, run the emulation algorithm, update the

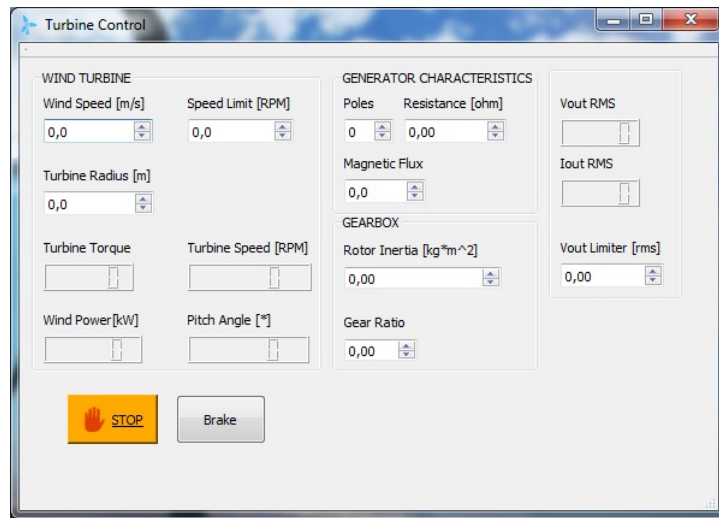


Figure 6.18: Graphical user interface developed for the implemented μC based WT emulator

external DAC, acquire data from the PC and update the GUI. This allowed to reach a system model simulation frequency of $F_s = 25\text{kHz}$. This emulation speed is enough to perform an open loop WT emulation but it is not enough to implement the current control loop needed to perform the PMSG inductance emulation.

A faster second version of the board has been realized by using the μC internal DAC, and controlling the emulation program without a GUI, using the watch variable function inside the TI Code Composer Studio integrated development environment (IDE). The offset calibration signals have been obtained from high resolution PWM outputs. This faster version of the WT emulator is able to acquire analog data, process the simulation model and update the DAC outputs in only $11\mu\text{s}$, allowing the emulation to run at a frequency of $F_s = 90\text{kHz}$.

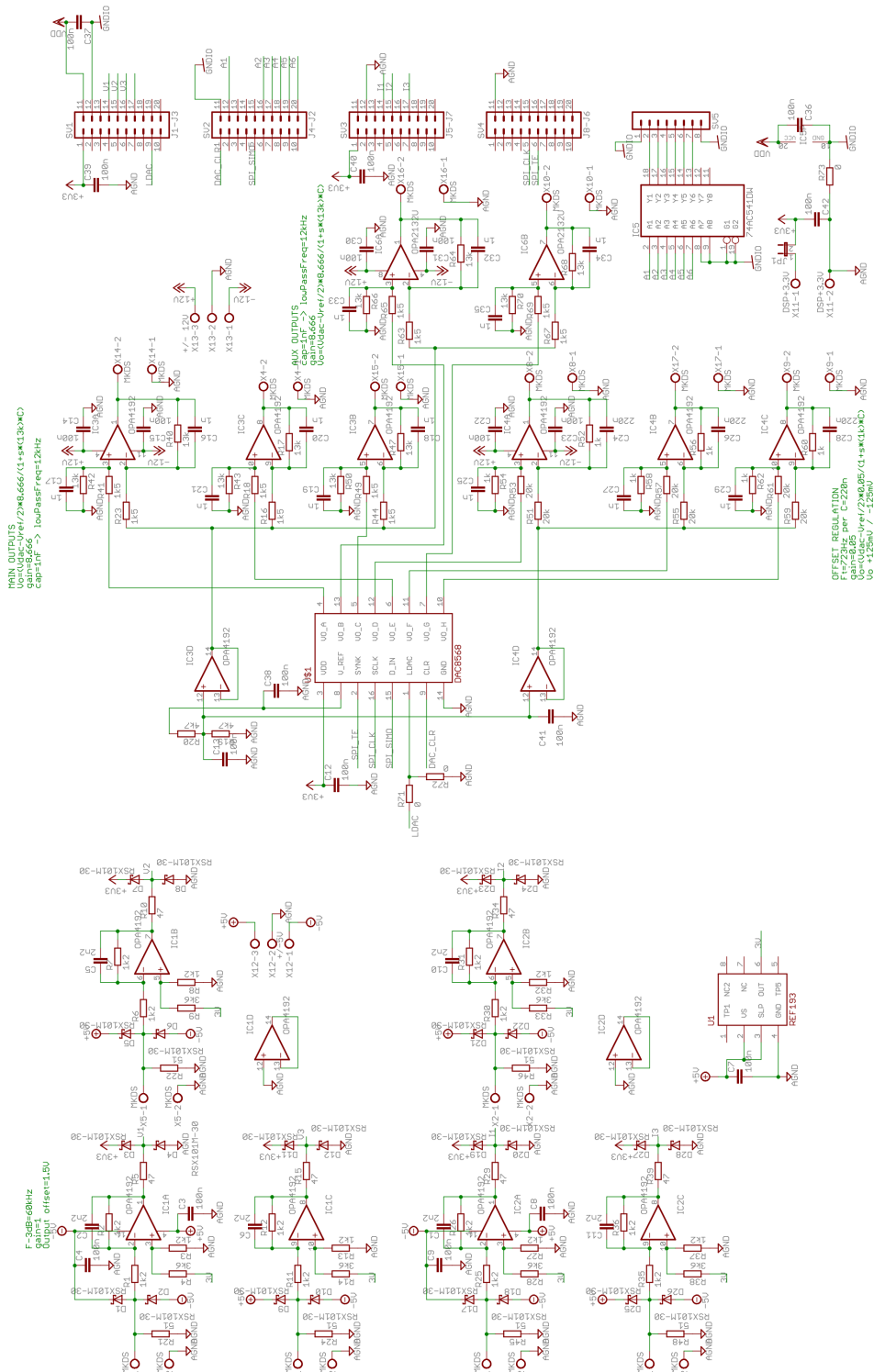


Figure 6.19: Analog signals conditioning board schematic

6.9 IMPEDANCE EMULATION

The PMSG inductance emulation can be used to set a more accurate inductance value seen by the WEC. More specifically, without inductive emulation the inductances seen by the WEC are just filter inductors L_{abc} . If the PMSG is a non-salient pole generator and if its inductance value is similar to the L_{abc} one, a software emulation is not needed to correctly model the generator impedance. On the other hand, if the PMSG inductance value is different from the L_{abc} one, or if it depends on the rotor position, a software emulation is needed to simulate the PMSG impedance correctly.

An example of impedance emulation is reported in [13, 14, 23], where a current controlled source is used to emulate a generic impedance. As stated in [13, 14] emulating a capacitive impedance using a current controlled source can be a difficult task due to the inclusion of a derivative term in the emulated impedance equation. This derivative term can lead to detrimental behaviours. Similarly, the same problems arise when emulating an inductive impedance using a voltage controlled source.

This study is focused on inductance emulation using a voltage controlled source, represented by the controlled power supply. This is achieved by measuring the amplifier output current and subtracting the inductance voltage drop caused by the output current on the amplifier output voltages.

As stated in (6.1), this approach includes in the control loop the derivative of the measured output current.

The emulation of a derivative behaviour can lead to :

- High frequency noise amplification
- Instability issues due to high gain and positive phase shift at high frequency

As reported in [13, 14], a low pass filter $G_f(s)$ can be used to limit the derivative behaviour at high frequency, the high frequency noise amplification and to stabilize the system.

The system can be approximated as shown in Fig. 6.20, a principle schematic where L_{emabc} are the emulated inductances, L_{abc} the filtering output inductances and $Z_{dut abc}$ the WEC input impedances. The three phase output currents i_{abc} are measured and used by the real time hardware to calculate the inductive behaviour of the controlled power supply voltage outputs. The overall external impedance Z_0 is obtained as the series of the WEC impedance $Z_{dut abc}$ and the external inductances L_{abc} :

$$\begin{aligned} Z_{0a} &= Z_{dut a} + sL_a \\ Z_{0b} &= Z_{dut b} + sL_b \\ Z_{0c} &= Z_{dut c} + sL_c \end{aligned} \tag{6.3}$$

Hereafter the description refers to a generic single phase, unless differently specified.

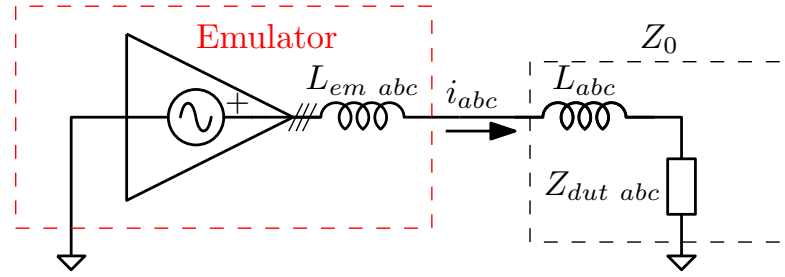


Figure 6.20: Normalized schematic of the impedance emulation of series inductance

Fig. 6.21 shows the normalized block diagram of the impedance emulation control loop of a generic phase, where G'_{amp} is the normalized amplifier transfer function obtained by dividing the amplifier transfer function by its baseband gain:

$$G_{amp}(s)' = \frac{G_{amp}(s)}{G_{amp}(0)} \quad (6.4)$$

and G_{z0} the transfer function between output voltage and current, given by the overall output admittance:

$$G_{z0} = \frac{1}{Z_0} \quad (6.5)$$

G_f is the transfer function of the low pass filter, and $s \cdot L_{em}$ the transfer function of the inductance to emulate.

The sensing board transfer function has been neglected because its cutoff frequency, $F_{sns} = 150\text{kHz}$, is higher than the emulator running frequency $F_s = 90\text{kHz}$ and the amplifier cutoff frequency $F_{amp} = 10\text{kHz}$. Consequently, the overall open loop transfer function of the system is:

$$G_{tot}(s) = G'_{amp}(s) \cdot G_{z0}(s) \cdot G_f(s) \cdot s \cdot L_{em} \quad (6.6)$$

In the following subsections the inductance emulation is studied by assuming different WEC input impedances.

6.9.1 Resistive load

As a first example let us assume the input impedance of the WEC to be a resistance R_0 . In this condition, the G_{z0} can be modelled as a low pass filter:

$$G_{z0} = \frac{1}{R_0 + sL_a} \quad (6.7)$$

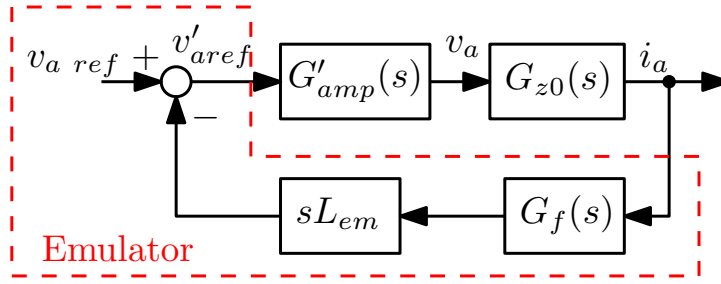


Figure 6.21: Principle block diagram of the impedance emulation of series inductance

Fig.6.22 displays the bode plot of the transfer functions composing the control loop. The effect of the emulator timestep has been described with G_{del} , a transfer function modelling a fixed delay of $T_s = 12\mu s$.

The resulting overall open loop transfer function G_{tot} is shown in Fig. 6.23 for different values of R_0 . More specifically, the smaller resistance value, $R_0 = 5\Omega$, has been obtained by dividing the WEC single phase nominal power, 10kW, by its nominal voltage, 230V. The bode graph has been traced for $L_{em} = 10mH$, $L_a = 2mH$ and emulator step time $T_s = 12\mu s$. The proportional constant is used to increase the closed loop system precision.

As shown in Fig. 6.23 the open loop transfer function G_{tot} presents a phase $\angle G_{tot}(s)|_{0dB} = -280^\circ$ when the high frequency gain reaches 0dB. As the phase margin $PM = 180^\circ - \angle G_{tot}(s)|_{0dB}$ is negative for every value of R_0 , the system is unstable, according to the reduced Nyquist stability criterion. In other words, the total open loop gain is crossing the 0dB gain axis with a 40dB/dec slope, which results in closed loop instability. The worst case is represented by the smaller value of $R_0 = 5\Omega$ as this value maximizes the open loop gain.

To stabilize the system a low pass filter has to be designed to reduce the open loop bandwidth and allow the total open loop transfer function to cross the 0dB gain axis with a 20dB/dec slope with a sufficient phase margin. The low pass filter cutoff frequency has been dimensioned through a recursive algorithm to obtain the desired phase margin. Fig. 6.24 shows the open loop gain G'_{tot} , stabilized by using a low pass filter with cutoff frequency dimensioned to obtain an open loop phase margin $PM = 60^\circ$.

Fig. 6.25 and Fig. 6.26 show a simulation of the $L_{abc} = 10mH$ inductance emulation. The resistive load $R_0 = 5\Omega$ is repeatedly connected and disconnected from the emulator to highlight the voltage transient on the amplifier output voltages v_{abc} . The permanent magnet generator model is rotating at 480 rpm and the pole number is $p = 5$, so the output voltage frequency is $F_e = 40Hz$. In Fig. 6.26 it is clearly visible the transients produced by the load disconnection (time = 0.1s), the phase jump produced by the load insertion (time = 0.2s) and the voltage drop caused by the inductive impedance on the amplifier output voltages v_{abc} .

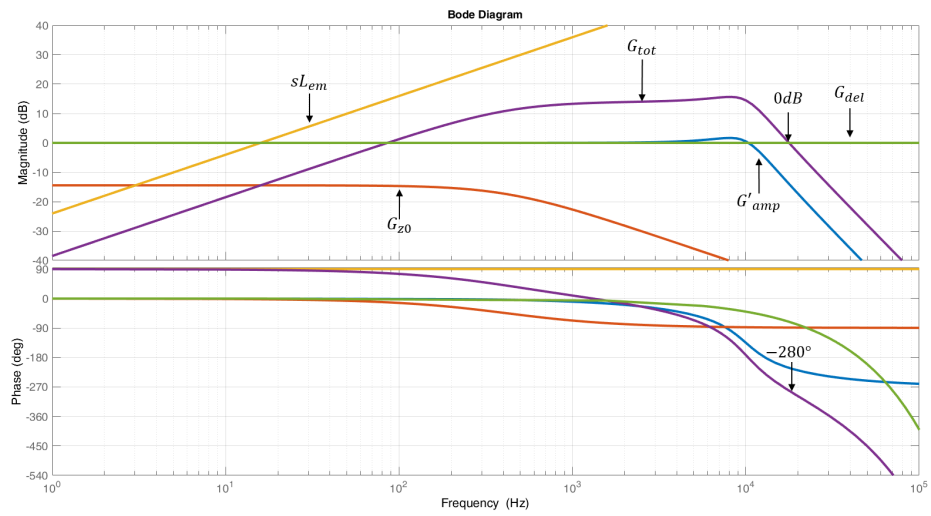


Figure 6.22: Transfer function of $G_{tot}(s)$, $G'_{amp}(s)$, $G_{z0}(s)$ and sL_{em}

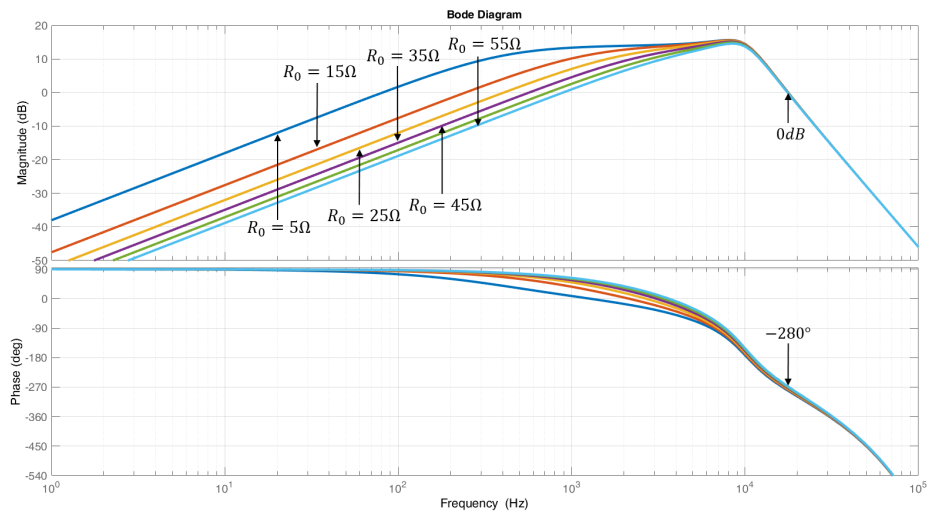


Figure 6.23: Open loop gain for different values of R_0

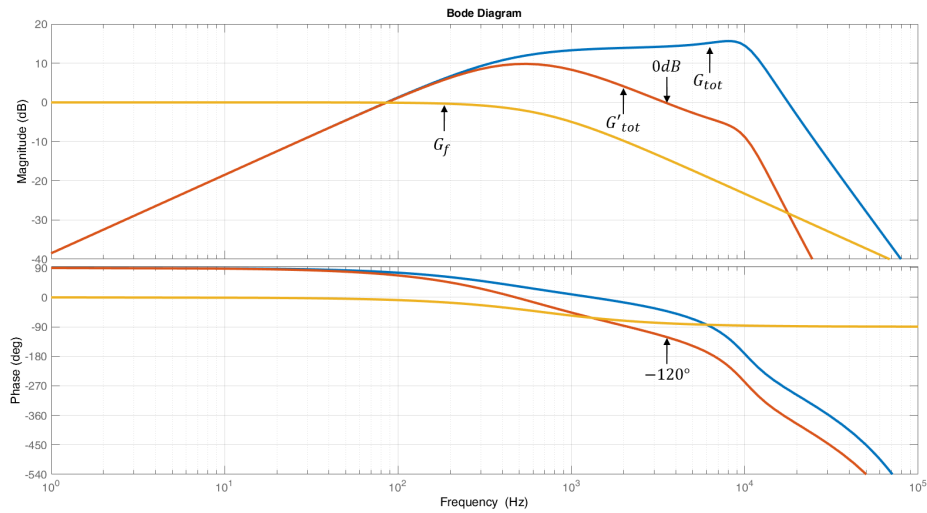


Figure 6.24: Transfer function of the low pass filter $G_f(s)$, the unstable open loop gain without filter $G_{tot}(s)$, the stabilized open loop gain with the filter $G'_{tot}(s)$

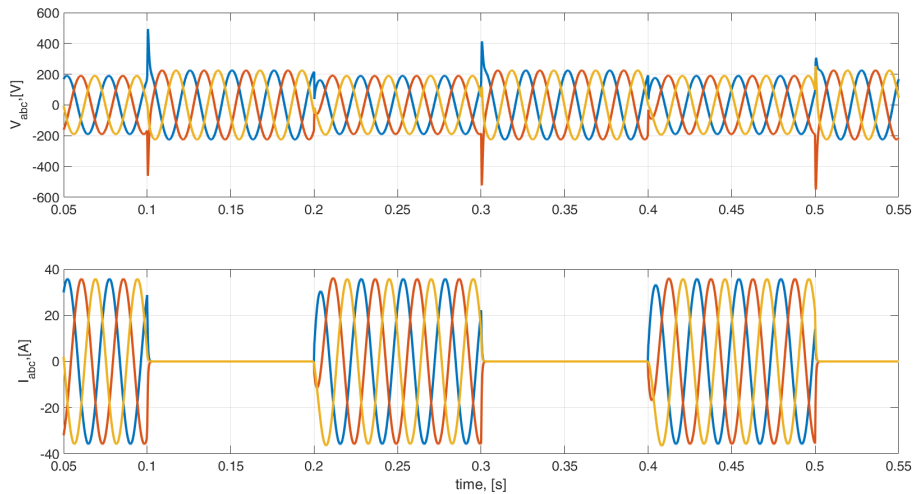


Figure 6.25: Simulation of the L_{abc} inductance emulation during a $R_0 = 5\Omega$ resistive load connection and disconnection

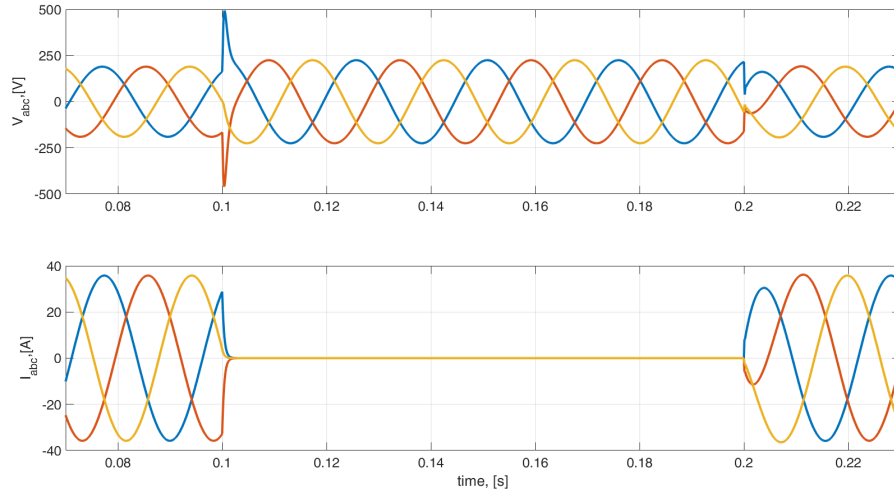


Figure 6.26: Detail of Fig. 6.25

6.9.2 Current controlled inverter load

Let us now consider a simplified model of a typical WEC input inverter, whose schematic is shown in Fig. 6.27. Its block schematic is shown in Fig. 6.28. In this simplified case the WEC input impedance is given by:

$$Z_0(s) = \frac{e_x(s)}{i_x(s)} = sL_{inv}[1 + T_{inv}(s)] \quad (6.8)$$

where L_{inv} is the inverter inductive input filter, i_x the measured current, e_x the output voltage of the emulator, and T_{inv} the WEC open loop gain obtained as:

$$T_{inv}(s) = \frac{G_{reg}(s) \cdot G_{pwm}(s)}{sL_{inv}} \quad (6.9)$$

where G_{reg} is the regulator processing the error between the reference current i_{ref} and the measured current i_x , G_{pwm} is the PWM modulator transfer function, which has been modelled as a normalized symmetrical PWM modulator with a switching frequency of $F_{inv} = 5\text{kHz}$ and a switching time of $T_{sw} = 200\mu\text{s}$:

$$G_{pwm}(s) = e^{-\frac{s \cdot T_{sw}}{2}} \quad (6.10)$$

From 6.9 and 6.10 it is clear that the WEC input impedance depends on the WEC regulator implementation and the switching frequency. As an example, the transfer

functions of an inverter controlled by using a PI regulator are shown in Fig. 6.29, where Z_0 is the inverter input impedance. The PI regulator transfer function is defined as:

$$G_{reg}(s) = k_p + \frac{k_i}{s} \quad (6.11)$$

The WEC impedance depends on the k_i and k_p constants, more specifically, the worst case is obtained by neglecting the k_i constant: the WEC impedance is directly proportional to the k_p constant, which represents the converter bandpass resistance. The bode diagrams in Fig. 6.29 are obtained with $k_p = 5$ and $k_i = 1000$. The value of k_p is chosen to obtain an input impedance of 5Ω , that is the nominal resistance to obtain 1pu.

In Fig.6.29 it is possible to see that, as expected, the WEC impedance Z_0 is dependent on the PI regulator transfer function G_{reg} and on the inverter open loop transfer function T_{inv} .

In this scenario the stabilized transfer function G'_{tot} of the inductance emulator is shown in Fig. 6.30, obtained by designing a low pass filter to reduce G_{tot} bandwidth and archive a phase margin $PM = 60^\circ$. In Fig. 6.30 the overall impedance seen from the amplifier G_{z0} and the low pass filter G_f are also reported.

It is also clear that using this approach the emulated inductive behaviour is limited by the response of the low pass filter G_f . In this case, to emulate a 10mH inductance the cutoff frequency must be 72Hz to obtain a phase margin of 50° . The filter limits both the static and dynamic response of the emulated inductance. In other words, the response of the derivative effect of the inductance emulation block sL_{em} shown in Fig.6.21 is limited by the response of the filter $G_f(s)$. Therefore, the derivative of the harmonics of i_a at frequencies higher than the $G_f(s)$ cutoff frequency will be correspondingly attenuated.

Moreover, the filter cutoff frequency needed to stabilize the system is inversely proportional to the emulated inductance value for a given system phase margin. Therefore, to obtain higher values of emulated inductance the cutoff frequency of the filter must be placed at a lower frequencies.

Fig. 6.31 and Fig. 6.32 show the simulation results of an emulated inductance $L_{abc} = 10\text{mH}$ connected to a current controlled inverter using a PI regulator. The inverter is connected and disconnected from the emulator to inspect the voltage transients on the amplifier output voltages v_{abc} . Fig. 6.26 shows a detail of the transient produced by the load disconnection (at 0.1s) and the phase jump produced by the load insertion (at 0.2s).

6.9.3 Inductance emulation in DQ reference frame

Inductance emulation in the DQ reference frame allows to limit the effect of the static distortion introduced by the filter G_f . As the amplifier output currents are constant in

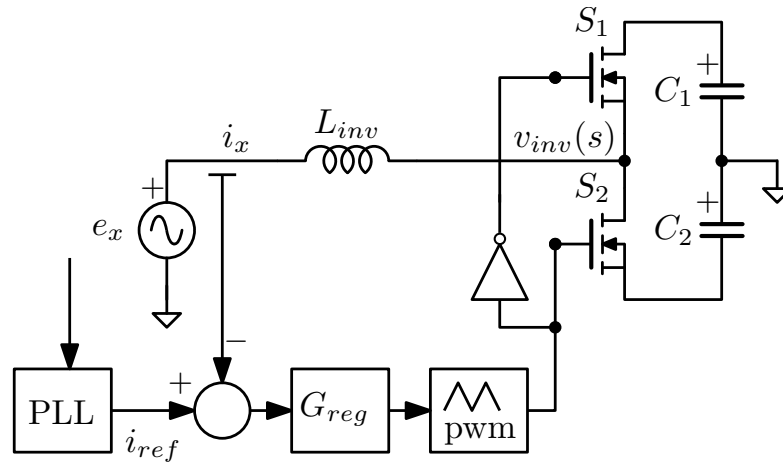


Figure 6.27: Simplified schematic of a single phase in a WEC input inverter

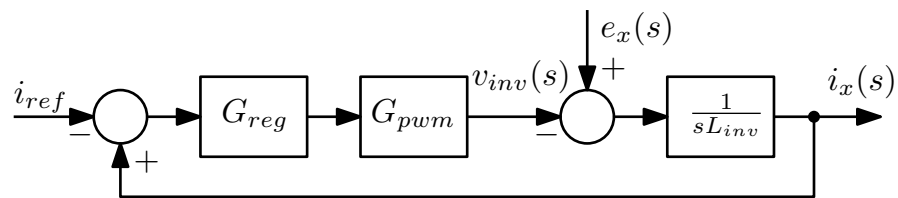


Figure 6.28: Block diagram of a typical WEC input inverter

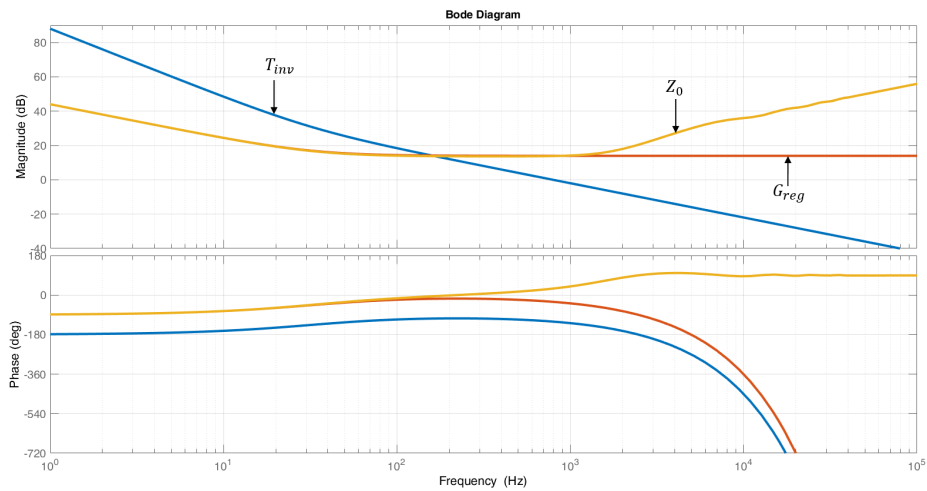


Figure 6.29: Inverter open loop transfer function $T_{inv}(s)$, regulator transfer function $G_{reg}(s)$ and input impedance $Z_0(s)$

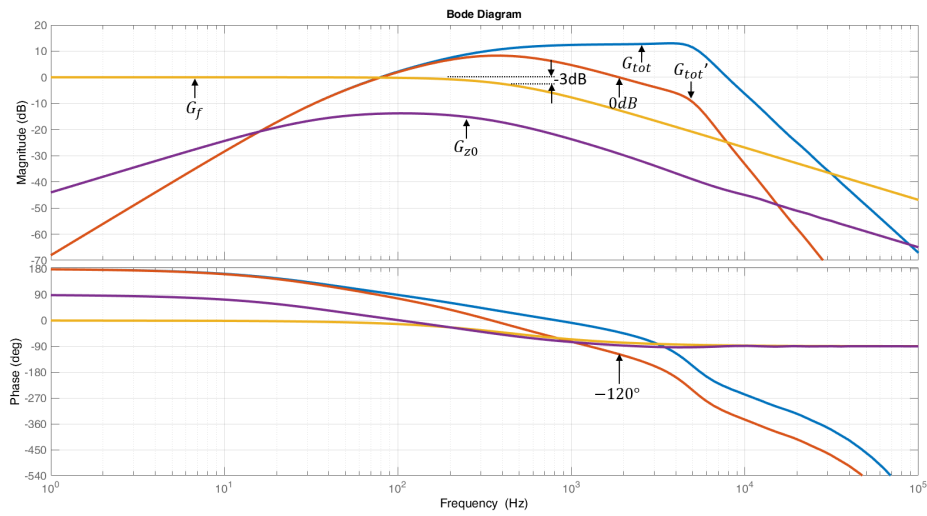


Figure 6.30: Transfer function of the low pass filter $G_f(s)$, the unstable open loop gain without filter $G_{tot}(s)$, the stabilized open loop gain with the filter $G'_{tot}(s)$ and the transfer function between amplifier voltage and current $G_{z0}(s)$

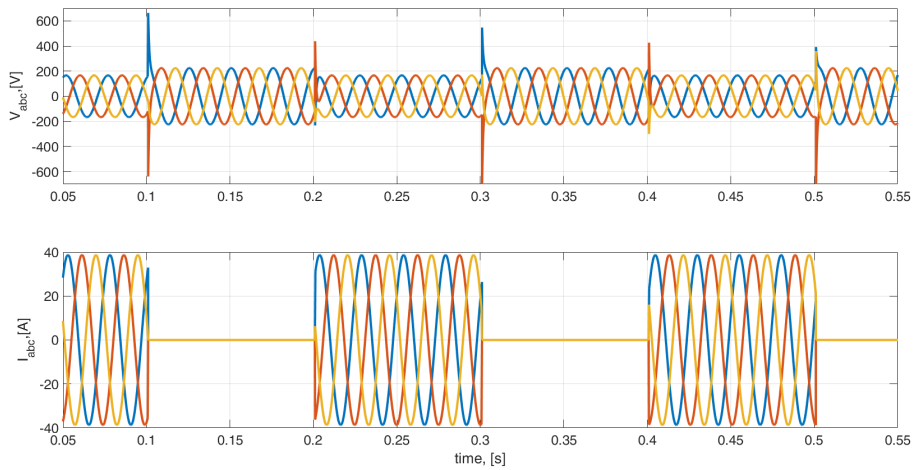


Figure 6.31: Simulation of the Labc inductance emulator driving a current controlled inverter being connected and disconnected repeatedly

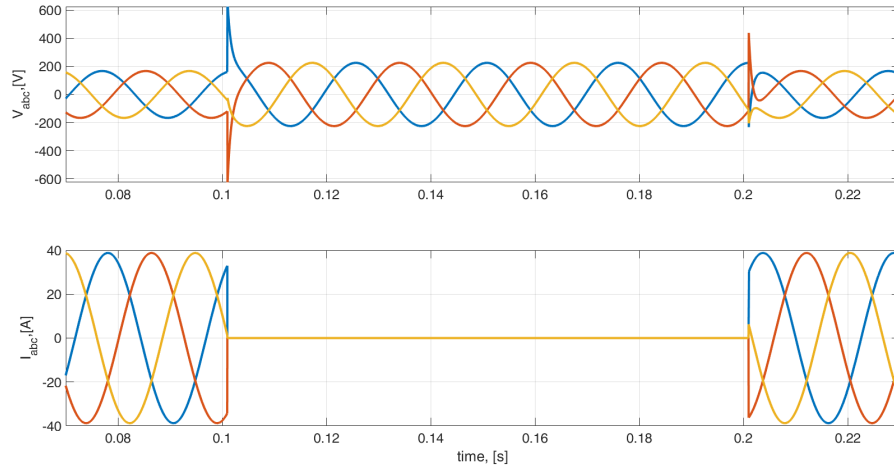


Figure 6.32: Detail of Fig. 6.31

the DQ reference frame, applying a low pass filter to their direct and quadrature components would influence just their dynamic response. As a result, the static response of the emulated inductance is correctly modeled.

In the DQ reference frame the PMSG can be written as following:

$$\begin{aligned} u_d &= L_d \frac{di'_d}{dt} + R_s \cdot i'_d - \omega_e \cdot L_q \cdot i'_q \\ u_q &= L_q \frac{di'_q}{dt} + R_s \cdot i'_q + \omega_e \cdot L_d \cdot i'_d + \omega_e \cdot \Psi_f \end{aligned} \quad (6.12)$$

where i'_d and i'_q are the filtered quadrature and direct components of the PMSG currents. As shown in Fig. 6.33, the currents i_d and i_q are filtered by the filters G_{fd} and G_{fq} to limit the influence of the derivative terms $L_d \frac{di'_d}{dt}$ and $L_q \frac{di'_q}{dt}$.

Fig. 6.34 and Fig. 6.35 show a simulation of the L_{dq} inductance emulation. As in the previous L_{abc} emulation a resistive load $R_0 = 5\Omega$ is repeatedly connected and disconnected to highlight the voltage transients on the amplifier output voltages v_{abc} . The direct and quadrature emulated inductances are set to $L_d = 5\text{mH}$ and $L_q = 10\text{mH}$. As the modeled permanent magnet generator is rotating at 480 rpm and the pole number is $p = 5$, the output voltage frequency is $F_e = 40\text{Hz}$.

Similarly, Fig. 6.36 and Fig. 6.37 show a simulation of the L_{dq} inductance emulator connected to a current controlled inverter using a PI regulator. The active load is repeatedly connected and disconnected, highlighting the voltage transients on the emulator voltage output. Analogously to the previous test case, the direct and quadrature emulated inductances are set to $L_d = 5\text{mH}$ and $L_q = 10\text{mH}$ and the emulated PMSG output frequency is $F_e = 40\text{Hz}$.

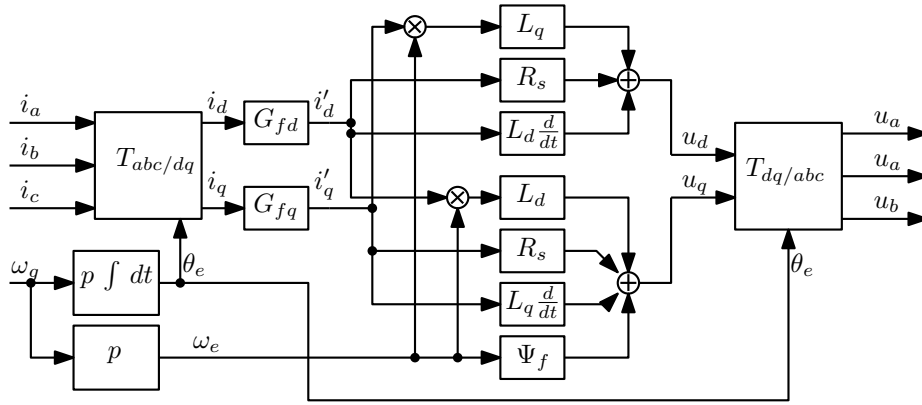


Figure 6.33: PMSG model including the L_d and L_q inductance emulation and the current filters G_{fd} and G_{fq}

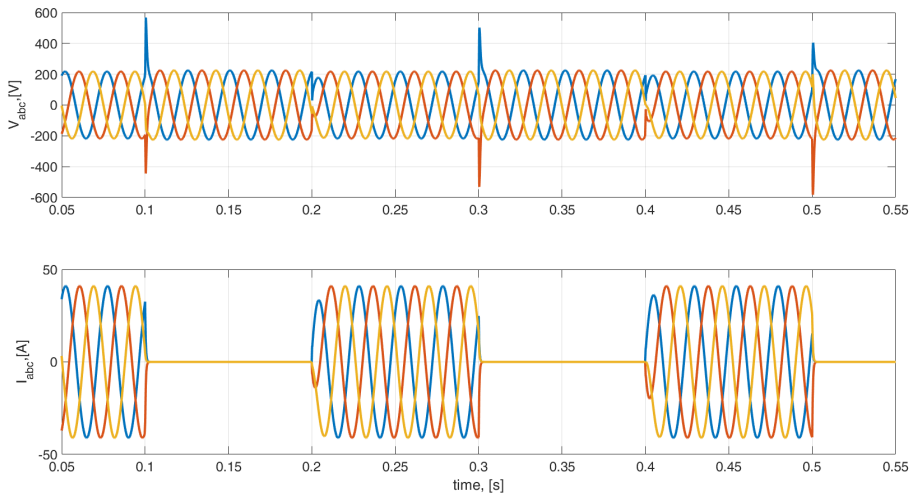


Figure 6.34: Simulation of a $L_d = 5\text{mH}$ and a $L_q = 10\text{mH}$ inductance emulation during a $R_0 = 5\Omega$ resistive load connection and disconnection.

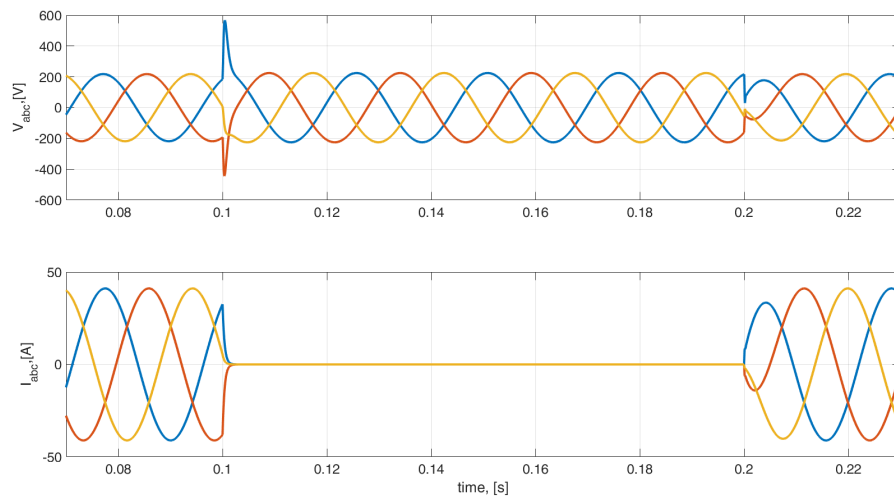


Figure 6.35: Detail of Fig. 6.34

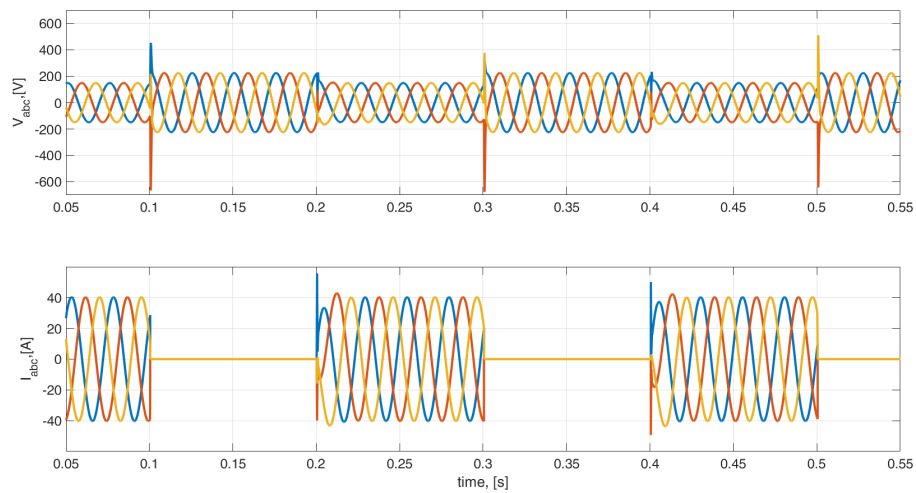


Figure 6.36: Simulation of a $L_d = 5\text{mH}$ and a $L_q = 10\text{mH}$ inductance emulation driving a current controlled inverter. The load is disconnected and reconnected to highlight the emulator output voltage transients reproduced by the inductance emulation.

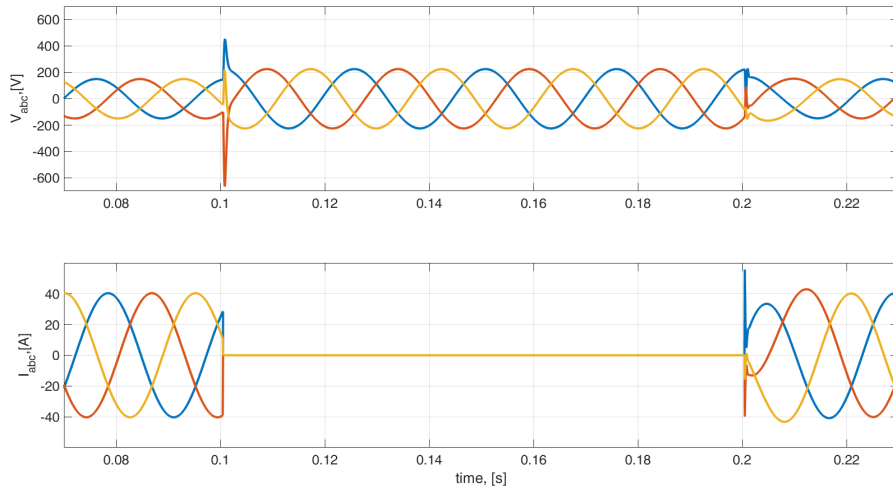


Figure 6.37: Detail of Fig. 6.36

Part IV

LOW VOLTAGE RIDE THROUGH TESTING

RESULTS

7.1 INTRODUCTION

The final test bench realization is shown in Fig. 7.1. The WEC under test is a 20kW wind converter for medium power PMSG based wind turbines. The WEC can be programmed to realize a maximum power point tracking inverter to maximize the power absorption from the WT. The grid side converter of the WEC can be programmed using a serial interface to realize both a torque or a power control over generator frequency and archive maximum efficiency extraction. The curve used to program the WEC, depicted in Fig. 7.2, has been calculated by connecting all the maximum power points in the WT power curve, converting it in torque values and consequently translating in i_q values. As shown in Fig. 7.2, the WEC PMSG side converter has been programmed to limit the currents to a nominal value of 40A. Over that value, the converter maximum efficiency is not reached and all the power extracted from the PMSG is injected into the grid up to reaching the nominal power of the WEC (i.e. 20kW).

7.2 TEST PROCEDURE

The test procedure consists of the following steps:

- Controllable power supply calibration
- Voltage sag emulator parameters programming
- Voltage sag emulator start
- WT emulation turn on
- Voltage sag test

When the controllable power supply is turned on, a voltage offset calibration is automatically performed on the amplifier outputs. After the calibration phase, the emulator model parameters can be inserted into the computer graphic user interface. The parameters used in the tests are reported in tab.7.1. The voltage sag generator can be started to generate the grid side three phase voltages, causing the WEC to activate. Consequently, the WT emulator can be activated.

Both the grid side and the generator side are monitored by using two oscilloscopes, as shown in Fig. 7.4. When the PMSG output frequency became greater than 9Hz

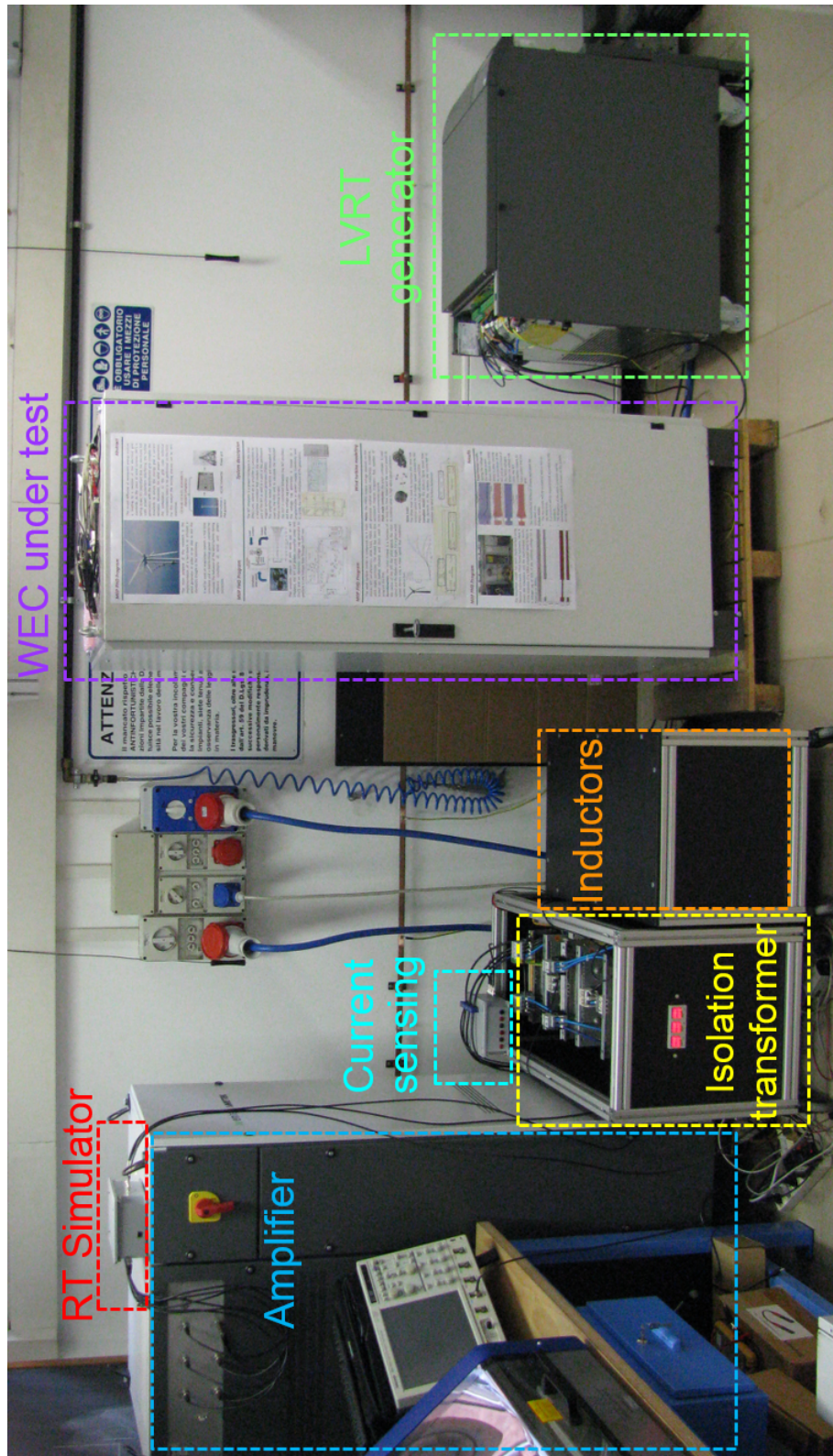
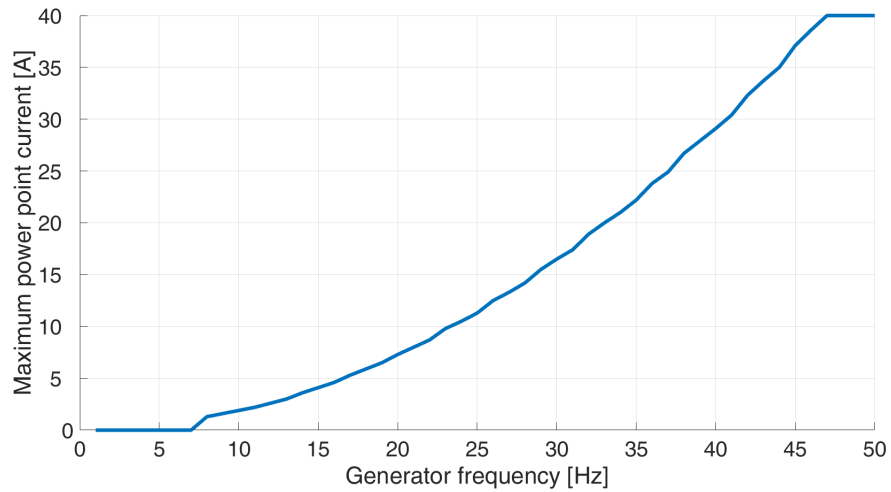


Figure 7.1: Test bench realization

Table 7.1: Simulation parameters

Parameter	Value
WT nominal power [kW]	30
WEC nominal power [kW]	20
Grid nominal voltage V_n [V]	230
Grid nominal frequency [Hz]	50
Air density [kg/m^3]	1.205
Turbine radius [m]	5
Rotor flux [Wb]	0.9
Number of pole couples	5
Generator inductance [mH]	4
Generator resistance [Ω]	0.1
Gear ratio	3
Friction coefficient [Nm/rad]	0
Rotor inertia [$\text{kg} \cdot \text{m}^2$]	90
Pitch actuator maximum speed [$^\circ/\text{s}$]	10

Figure 7.2: I_q current versus frequency lookup table used to program the WEC under test

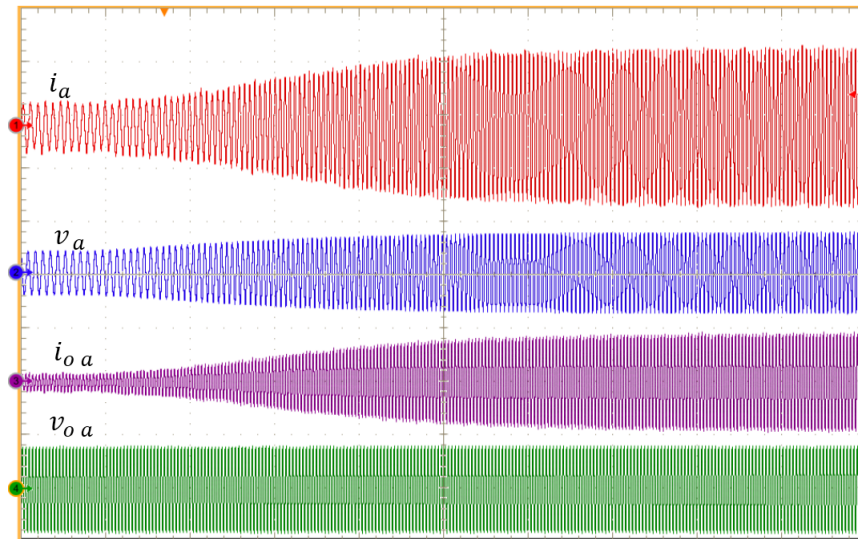


Figure 7.3: Example of gradual wind and rotation speed after emulator turn on, measured on a single oscilloscope. v_a (300V/div), i_a (30A/div), $v_{o a}$ (400V/div), $i_{o a}$ (30A/div), timebase 500ms/div.

the WEC starts absorbing current from the controllable power supply. This frequency threshold is directly programmed into the WEC and is used to allow the WT to gain enough kinetic energy and to produce a significant torque before the WEC starts absorbing power from the emulated PMSG. This allows the WT to not be stopped by the electromagnetic torque produced by the WEC on the emulated PMSG at the start up. The WT emulator increases the rotor speed until a steady state value is reached, corresponding to an equilibrium between the torque generated by the wind on the rotor and the resisting torque applied by the PMSG. When the equilibrium is reached, the voltage sag can be programmed and triggered to produce voltage sags of any amplitude and duration. Fig. 7.3 shows the results of a gradual increase of wind speed and WT rotation speed. The oscilloscopes are synchronized with the voltage sag starting point so that both the WEC sides synchronized responses can be recorded and saved to be inspected.

7.3 LVRT TEST RESULTS

The LVRT testing results are reported in this section. Multiple test cases are inspected depending on the voltage sag entity and the pitch angle controller operation. To be easily compared, all tests has been performed applying the same 9m/s wind speed. This value has been chosen to reach a 15kW power extraction, which corresponds to a WEC operating point where the generator side currents are not limited by the maximum efficiency lookup table depicted in Fig.7.2. Moreover, as the power extraction

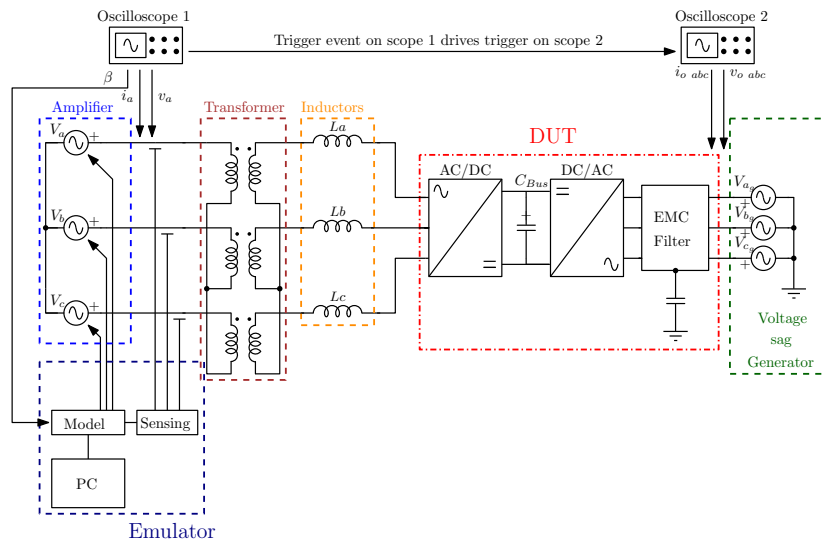


Figure 7.4: Test bench oscilloscopes measure points.

value is 75% of the WEC nominal power, a sufficient margin is available during the transients caused by voltage sags. At the same time, at this operating point, the controllable power supply currents are small enough to not cause saturation effects on the isolation transformer and filtering inductances.

The test results have been acquired using two four channels, 500MHz bandwidth Tektronix 7054 oscilloscopes, one connected to the emulator side and the other to the voltage sag generator side, as shown in Fig. 7.4. The trigger of the oscilloscopes has been connected to a common event, so that a synchronized representation of both sides of the test bench has been obtained. More specifically the trigger of the generator side oscilloscope drives the trigger of the voltage sag emulator side oscilloscope.

Both symmetrical and asymmetrical voltage sags has been reproduced to inspect their effects on the WEC under test. In the generator side and in the grid side, only single phase measures has been taken. Differently, to correctly represent asymmetrical voltage sags, two phase-to-phase voltages has been measured, obtaining the third by their difference. Similarly the three phase currents has been obtained by the difference of two line currents. The results waveforms notation is described in tab.7.2.

7.3.1 $45\%V_n - 390\text{ ms}$ symmetrical voltage sag LVRT test

In Fig. 7.5 a LVRT test is performed generating a symmetrical $45\%V_n - 390\text{ms}$ voltage sag. This test case is chosen on the basis of the CEI 0-21 standard [17], as shown in Fig. 7.6. In these conditions, the WEC is allowed to stop injecting power into the grid during the voltage sag but cannot disconnect from the grid. Immediately after the end

Table 7.2: Waveforms notation for the LVRT test results

Generator side voltages [V]	v_{abc}
Current side currents [A]	i_{abc}
Generator side extracted power [kW]	P_e
Blades pitch angle [°]	β
Grid emulator side line voltages [V]	$v_{o\ abc}$
Grid emulator side line currents [A]	$i_{o\ abc}$
Grid emulator side line-to-line voltages [V]	v_{oLL}
Grid emulator side line-to-line currents [A]	i_{oLL}

of the voltage sag the standard specifies the WEC to restart injecting power into the grid. In this specific test case, the pitch angle controller is disabled.

As shown in Fig. 7.5, the WEC stops injecting power into the grid and absorbing power from the WT emulator right after the beginning of the voltage sag and the absorbed currents, and consequently, the PMSG torque drop to zero. As the rotor torque is not balanced by the generator one, the WT rotation speed increases together with the generator output voltages. At the end of the voltage sag, the WEC restarts absorbing power from the emulated generator and injecting it into the grid emulator. In this situation the WEC lookup table drives the current absorption to a higher value as the generator frequency. This causes the resisting torque to be higher than the rotor one. The torque unbalance leads to a decrease in the WT rotational speed, until a new equilibrium state is reached again.

In Fig. 7.7 a LVRT test is displayed using the same operative condition of the previous one. In this test, the pitch angle controller reference rotation speed is programmed to be slightly higher than the WT steady state rotation speed. The purpose is to induce the pitch angle controller to activate right after the voltage sag to inspect its behavior and its effect on the WT. At the beginning of the voltage sag, the blades pitch angle is increased linearly as the pitch drive system operates at its maximum speed. From Fig. 7.7, it can be noticed that the pitch angle controller is too slow to significantly decrease the WT generator overvoltages, compared to the previous test case. After the voltage sag, the rotor speed decreases and the pitch angle controller decreases the blades angle accordingly until the initial steady state operation is met again. As the WT rotation speed value is below the programmed limit, the pitch angle returns to its initial zero value.

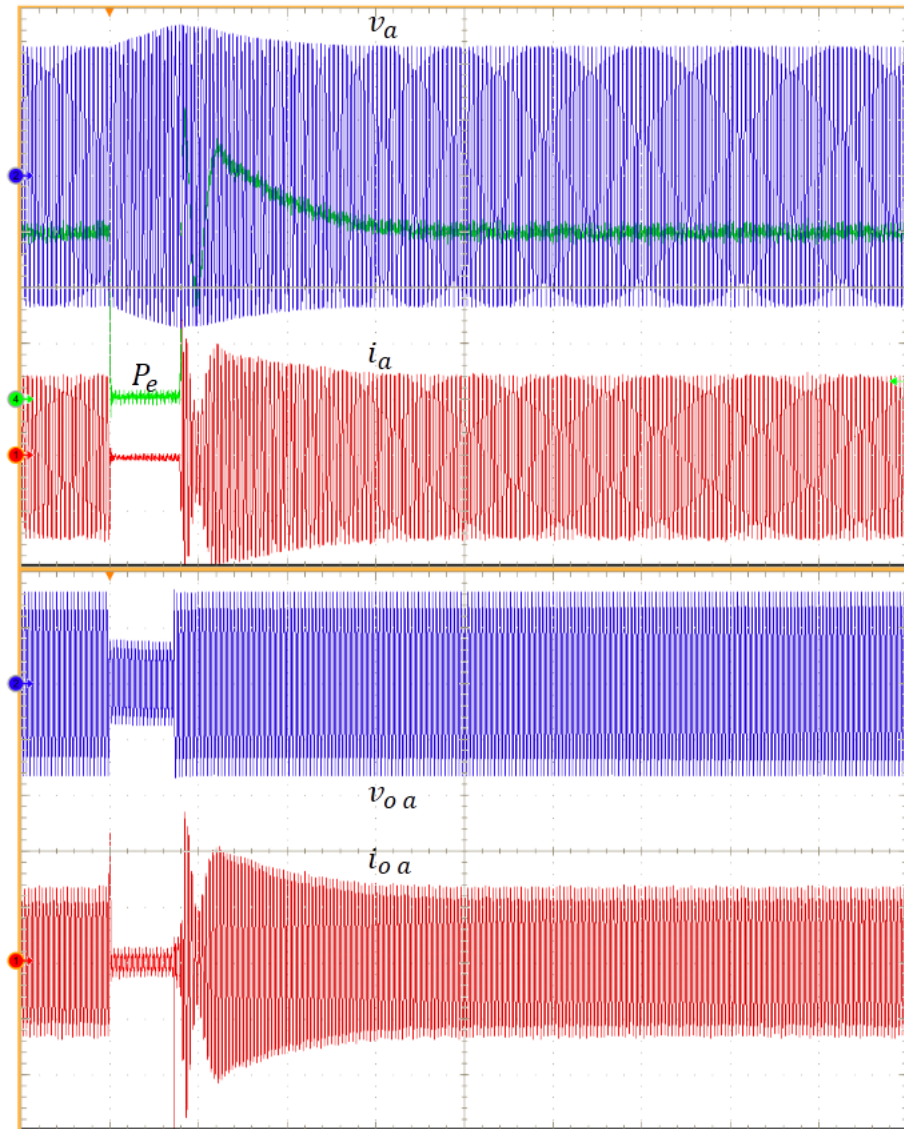


Figure 7.5: 390 ms, $45\%V_n$ symmetrical voltage sag, pitch angle controller disabled. v_{abc} (100V/div), i_{abc} (30A/div), P_e (5kW/div), $v_{o abc}$ (200V/div), $i_{o abc}$ (20A/div); timebase 500 ms/div.

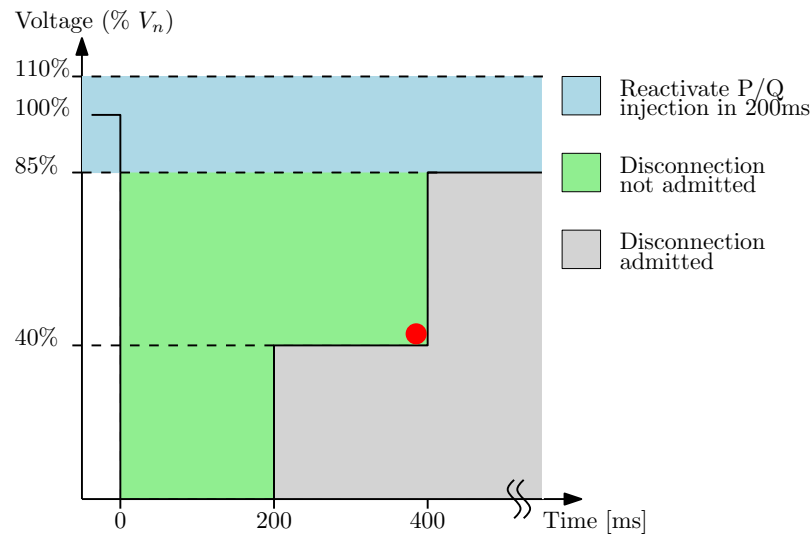


Figure 7.6: 390ms, 45% V_n voltage sag profile as specified in [17]

7.3.2 45% V_n - 390 ms asymmetrical voltage sag LVRT test

Fig. 7.8 and Fig. 7.10 shows two asymmetrical 45% V_n , 390ms voltage sag LVRT tests on a WT in the operating conditions specified in tab.7.1. As in Fig. 7.7, the test shown in Fig. 7.10 is taken by programming the pitch angle controller reference speed to be similar to the WT speed preceding the voltage sag. The voltage sag is applied only on one of the three phases of the emulated grid. The three output voltages are measured phase-to-phase. As the voltage sag is positioned within an area where disconnection is not allowed by the CEI-021 standard, as shown in Fig. 7.6, during the voltage sag the WEC is allowed to stop injecting power into the grid and absorbing it from the emulated PMSG. As in the previous test cases, the WT speed increase during the voltage sag, as the emulator PMSG resisting torque drops to zero. After the voltage sag, the WEC restarts its normal operation absorbing active power from the emulated PMSG, the WT speed decreases, the WT reaches the equilibrium between the rotor torque and the generator one. In Fig. 7.9 the oscilloscopes timebase is 100ms/div, to better inspect the effect of the voltage sag on the system waveforms.

In Fig. 7.10 the same voltage sag is applied to a WT in the same operating conditions. As in the test shown in Fig. 7.7, the angle controller reference rotation speed is programmed to be slightly higher than the WT steady state rotation speed to activate the pitch angle controller right after the voltage sag. As the voltage sag starts, the pitch angle controller increases the blades pitch angle to limit the WT overspeed. After the voltage sag ends, as the turbine speed decreases under the pitch angle controller reference value, the blades angle is driven to its initial position.

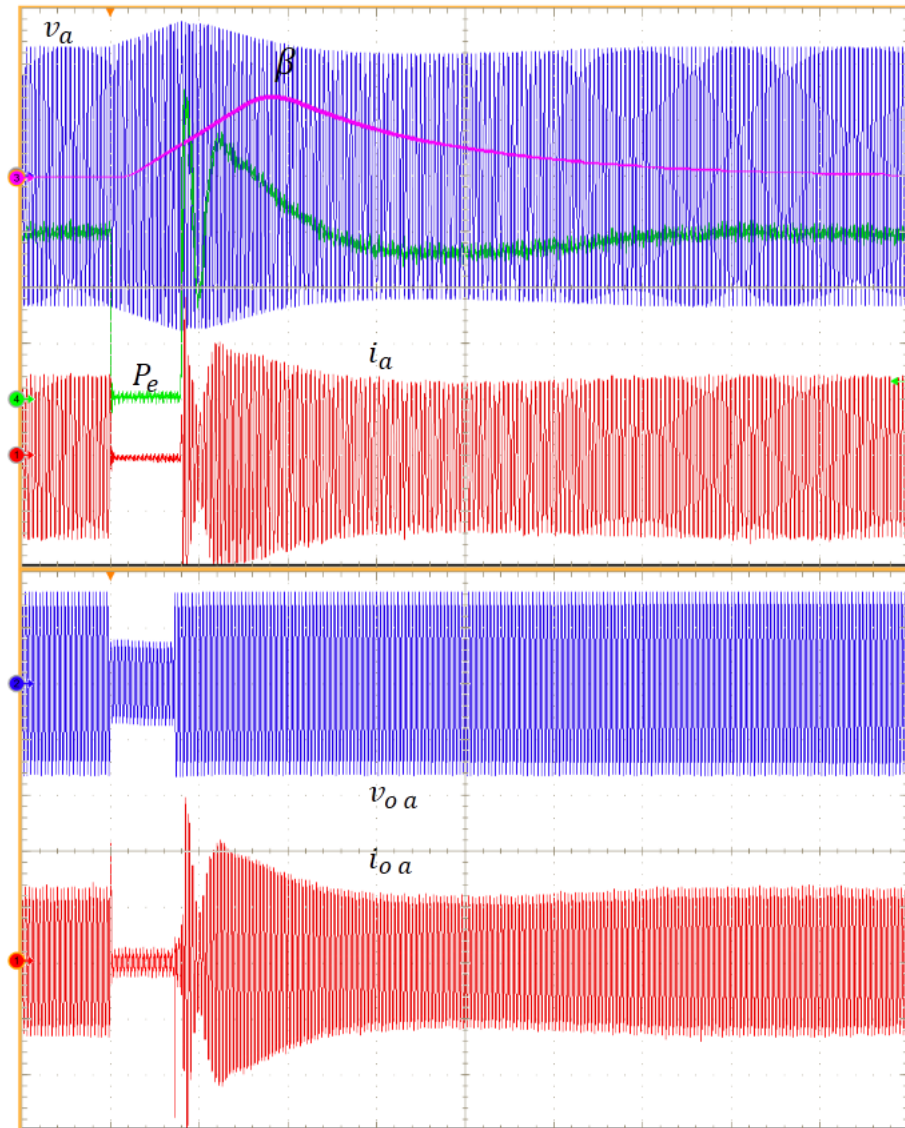


Figure 7.7: 390ms, 45% V_n symmetrical voltage sag, pitch angle reference speed set to 165rpm. v_{abc} (100V/div), i_{abc} (30A/div), P_e (5kW/div), $v_o abc$ (200V/div), $i_o abc$ (20A/div), β (5° /div); timebase 500ms/div.

In Fig. 7.11 the same test is performed to a WT with double rotational inertia, 180 kg/m^2 . The oscilloscopes are set to a timebase of 50 ms/div . As expected, the generator overspeed is reduced, because the increased inertia slows down the system response.

7.3.3 *Wind speed step variation*

In Fig. 7.12 the results from a wind speed step variation are shown. As the wind speed changes suddenly from 5 m/s to 9 m/s , the emulated rotor speed increases from 88 rpm to 162 rpm . In this test case, no voltage sag is applied and the WEC power extraction is not interrupted, increasing from 2.5 kW to 15 kW . This test allows to inspect the dynamics of the WT system and can be very useful to evaluate the behavior of a complete WT system during sudden changes in wind speed. In Fig. 7.13 the same test is considered, with the pitch angle controller activated, setting its reference WT speed to 120 rpm . As observed in the previous cases, the pitch angle controller regulates the blades pitch angle to limit the rotor rotation speed. When the pitch angle controller detects the WT overspeed, the pitch drive system operates at its maximum speed, as it is possible to see by the linear increase of the blades pitch. After a brief transient, the WT reaches an equilibrium state where the pitch angle controller regulates the WT speed to its reference value.

7.3.4 *45% V_n 410ms symmetrical voltage sag LVRT test*

In this LVRT test a voltage sag of $45\%V_n$ is applied for 410 ms . As shown in Fig. 7.15, the voltage sag is positioned outside the disconnection not allowed area in the CEI 0-21 standard voltage profile area. Consequently, the WEC is allowed to completely disconnect from the grid, or from the grid emulator in this case. As the emulated PMSG resisting torque becomes zero, the WT rotor speed increases until it becomes greater than the pitch angle controller reference. The pitch angle controller in this test is active and starts to regulate the blades angle in the instant their rotational speed becomes greater than the controller reference. As it is possible to note in Fig. 7.14, after a brief transient, the pitch angle controller regulates the blades pitch angle even if the WEC is not absorbing power from the generator. This test case highlights the importance of the pitch angle controller, because in case of WEC failures the WT speed can increase well beyond its nominal speed, leading to dangerous situations.

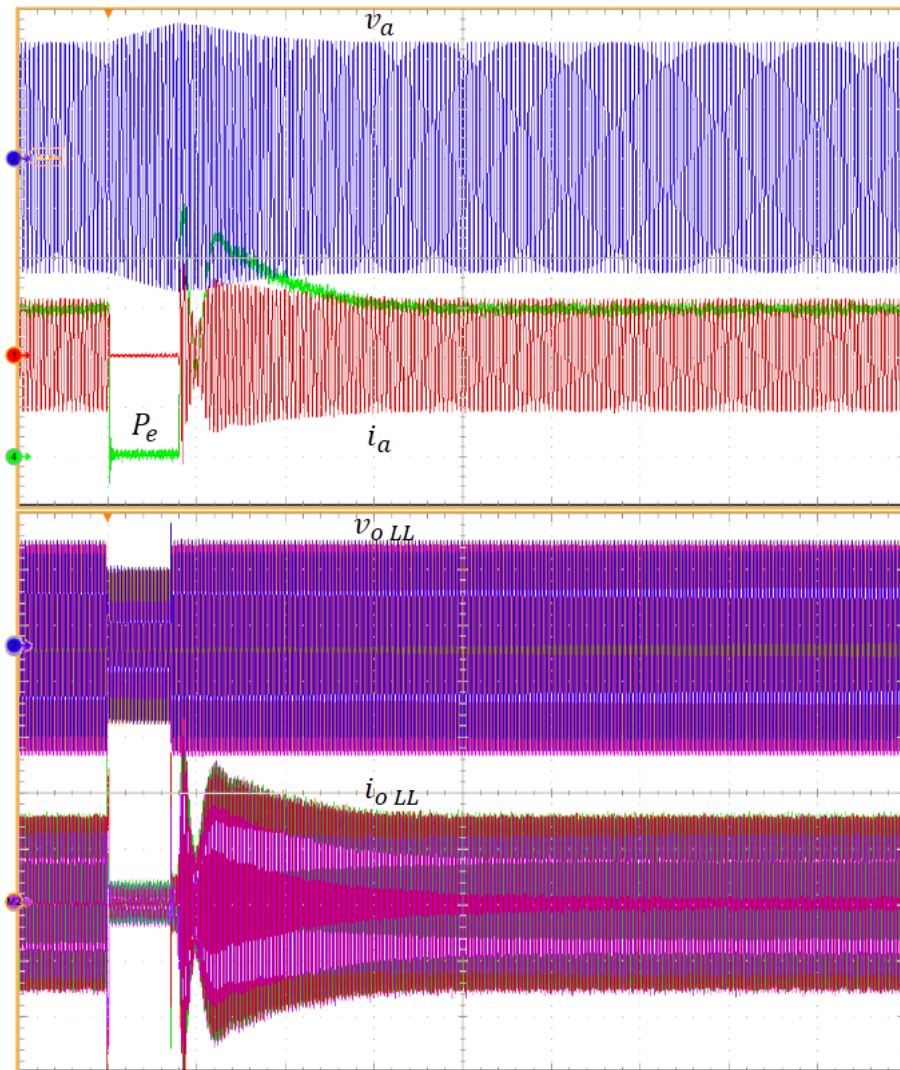


Figure 7.8: 390ms, 45% V_n asymmetrical voltage sag, pitch angle controller disabled, phase-to-phase grid side voltages. v_a (100V/div), i_a (30A/div), P_e (5kW/div), v_{oLL} (300V/div), i_{oLL} (30A/div); timebase 500ms/div.

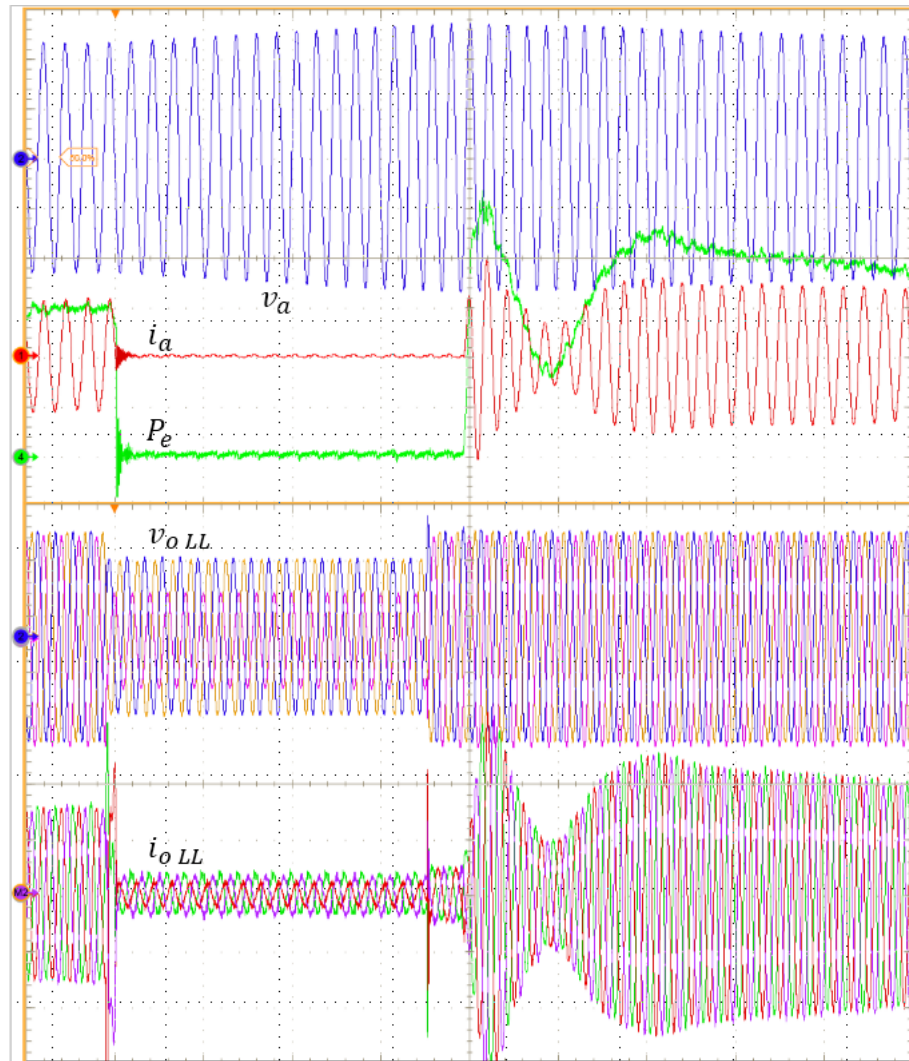


Figure 7.9: Zoomed-in view of Fig. 7.8. v_a (100V/div), i_a (30A/div), P_e (5kW/div), v_{oLL} (300V/div), i_{oLL} (30A/div); timebase 100ms/div.

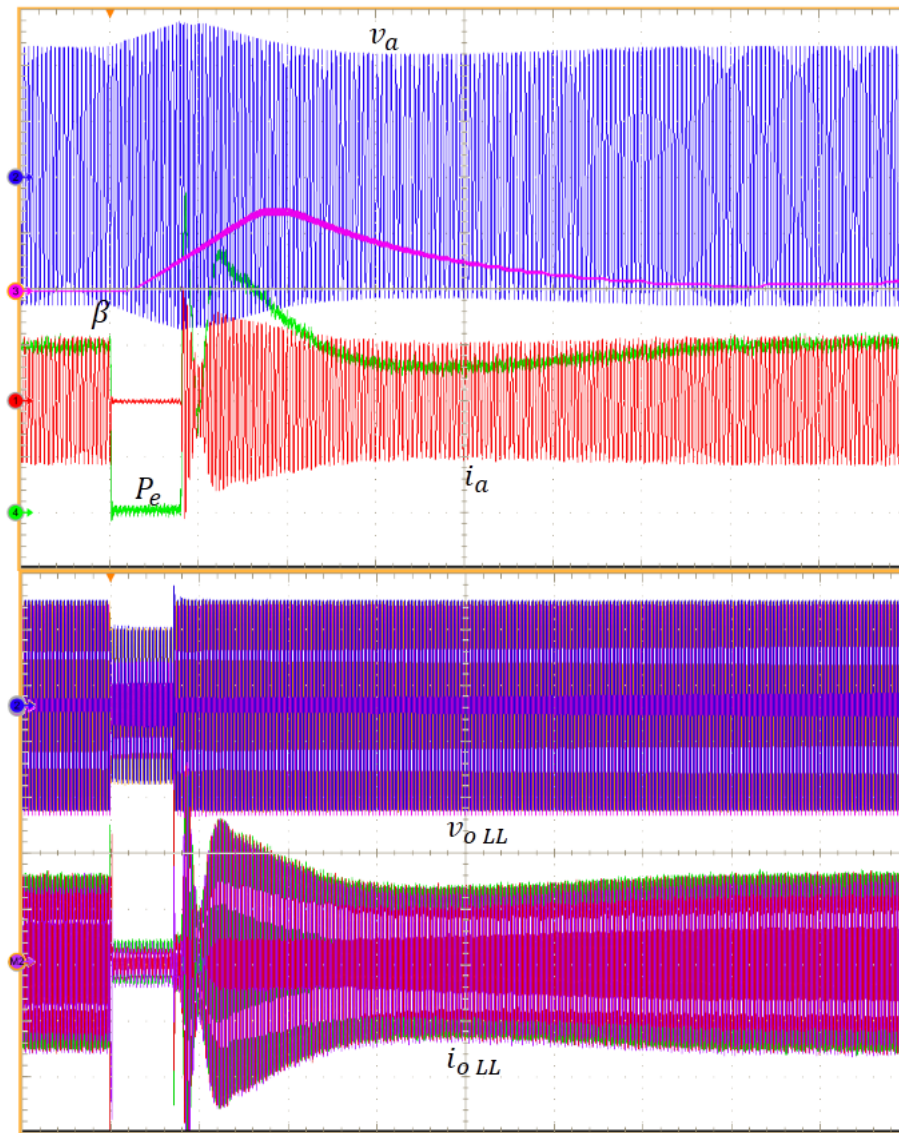


Figure 7.10: 390ms, 45% V_n symmetrical voltage sag, pitch angle controller reference speed set to 165rpm. v_a (100V/div), i_a (30A/div), P_e (5kW/div), v_{oLL} (300V/div), i_{oLL} (30A/div), β (5° /div); timebase 500ms/div.

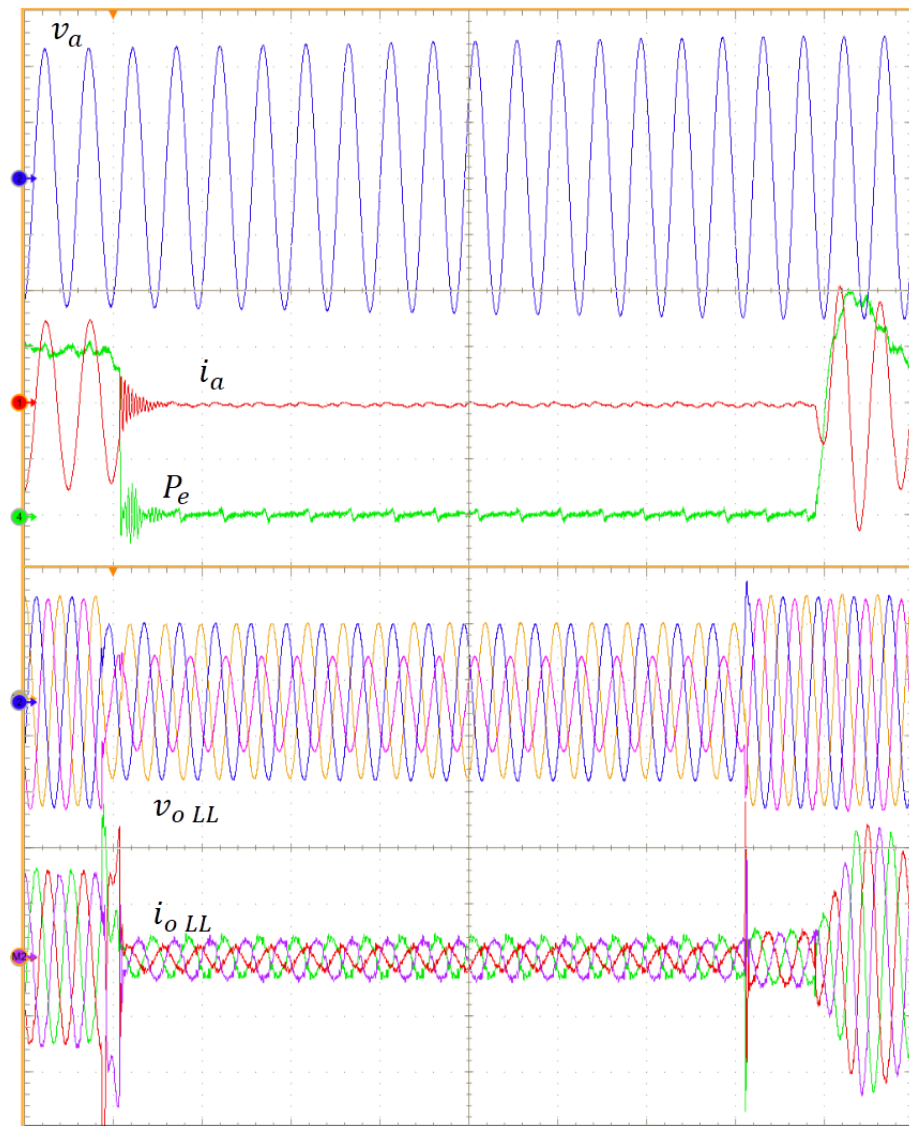


Figure 7.11: 390ms, $45\%V_n$ asymmetrical voltage sag, WT inertia 180 kgm^2 , pitch angle controller disabled, phase-to-phase grid side voltages. v_a (100V/div), i_a (30A/div), P_e (5kW/div), v_{oLL} (300V/div), i_{oLL} (30A/div); timebase 100ms/div.

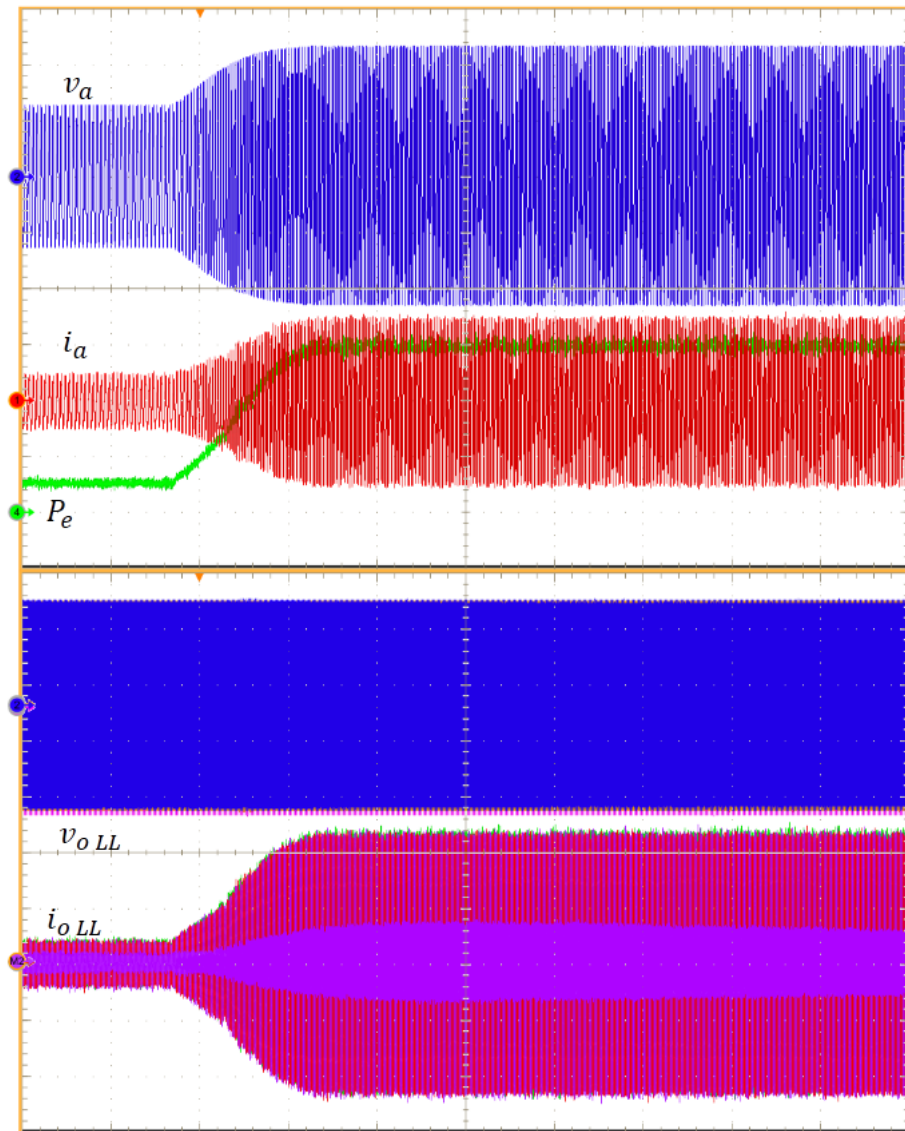


Figure 7.12: Wind speed step variation from 5m/s to 9m/s, pitch angle controller disabled, grid side phase-to-phase voltages. v_a (100V/div), i_a (30A/div), P_e (5kW/div), v_{oLL} (300V/div), i_{oLL} (20A/div); timebase 1s/div.

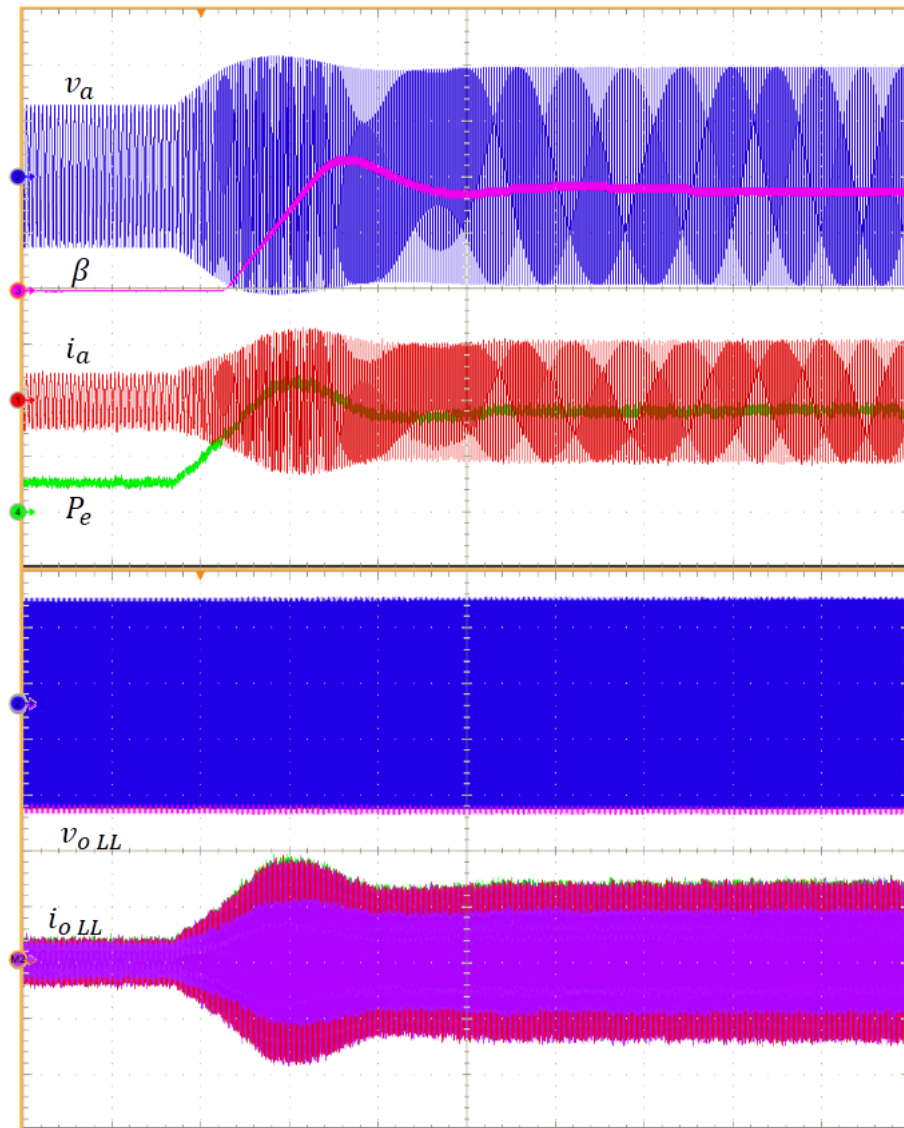


Figure 7.13: Wind speed step variation from 5m/s to 9m/s, pitch angle controller reference speed set to 150rpm, grid side phase-to-phase voltages. v_a (100V/div), i_a (30A/div), P_e (5kW/div), β (5° /div), v_{oLL} (300V/div), i_{oLL} (20A/div); timebase 1s/div.

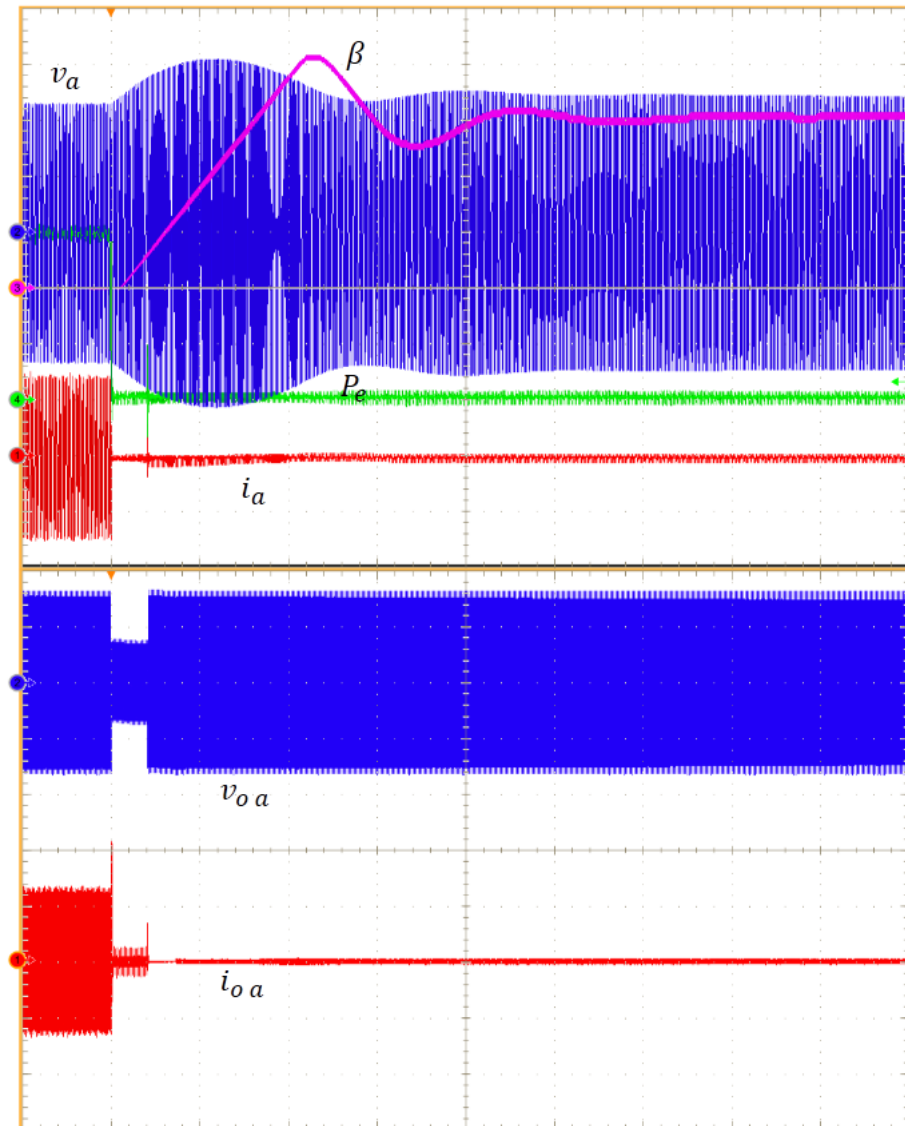


Figure 7.14: WEC disconnection due to a 420ms, 40% V_n voltage sag, pitch angle controller reference speed set to 165rpm. v_a (100V/div), i_a (30A/div), P_e (5kW/div), β (5° /div), v_{oLL} (200V/div), i_{oLL} (20A/div); timebase 1s/div.

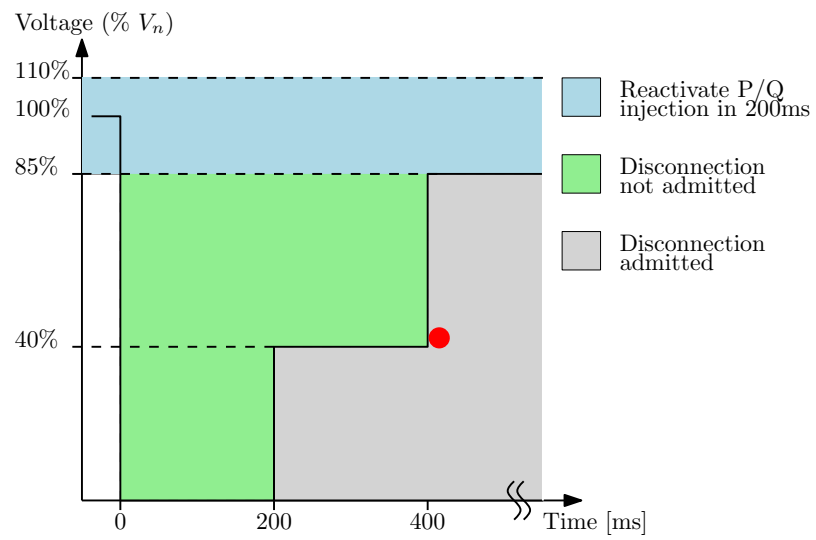


Figure 7.15: 420ms, 40% V_n voltage sag in the CEI-021 standard LVRT profile

7.4 ON FIELD TESTS

Fig.7.16 shows the voltages, currents and output frequency waveforms of a real PMSG based, 70kW WT. In this case the WT is operating with the wind blowing at 11m/s, in nominal conditions of power extraction. The rotor diameter of the WT is 20m, its nominal rotation speed is 72rpm its pitch angle drive system is a very fast hydraulic linear driving system. The generator voltages are measured phase-to-phase, the current waveforms are the three line currents absorbed from the WEC and the frequency has been obtained from the voltage waveforms zero crossing. The WT is based on a direct drive PMSG with a nominal voltage of 410V. The WEC is CEI 0-21 certified and its maximum three-phase input line-to-neutral voltage is 480V.

When the WEC is disconnected from the grid the currents absorption from the generator drops to zero. This causes the output voltages to experiment a sudden magnitude increase as the internal generator impedances voltage drop became zero too. In this situation the voltage at the generator terminals are:

$$\begin{aligned} u_d &= 0 \\ u_q &= \omega_e \cdot \Psi_f \end{aligned} \tag{7.1}$$

The reactive nature of the generator impedances cause a phase jump on the generator voltages. This is the effect of the generator current absorption drop. As the frequency measure is obtained by calculating the mean zero crossing on the generator voltages, the phase jump causes a disturbance on the frequency waveform. Therefore, at 100ms, a peak in the frequency waveform appears evident, as shown in fig.7.16.

As the WEC stops absorbing currents, the PMSG resisting torque drops to zero, and the WT starts to accelerate until the pitch angle driving system turns the WT blades enough to decrease the WT rotor torque. From the generator frequency waveform it is possible to note the WT reacts very well to the WEC disconnection:

- The WT rotor speed increases only by 2% in the first 200ms, after the currents absorption drops to zero. This effect is due to a very large moment of inertia of the rotor, which naturally helps to slow down the WT overspeed. In case of a voltage sag contained into the disconnection not allowed area, i.e. , from 200ms to 400, this WT experiences an overspeed that is almost negligible.
- The pitch angle controller and pitch drive system are so fast and responsive that after only 500ms the blades pitch have been increased to a value high enough to decrease the rotor torque to a negative value. As a consequence, the WT speed starts to decrease.

As the wind turbine characteristics and parameters are confidential, it is not possible to perform a match between the emulation model and the on field results. Nonetheless,

the qualitative analysis shows the obtained waveforms are coherent with the expected ones.

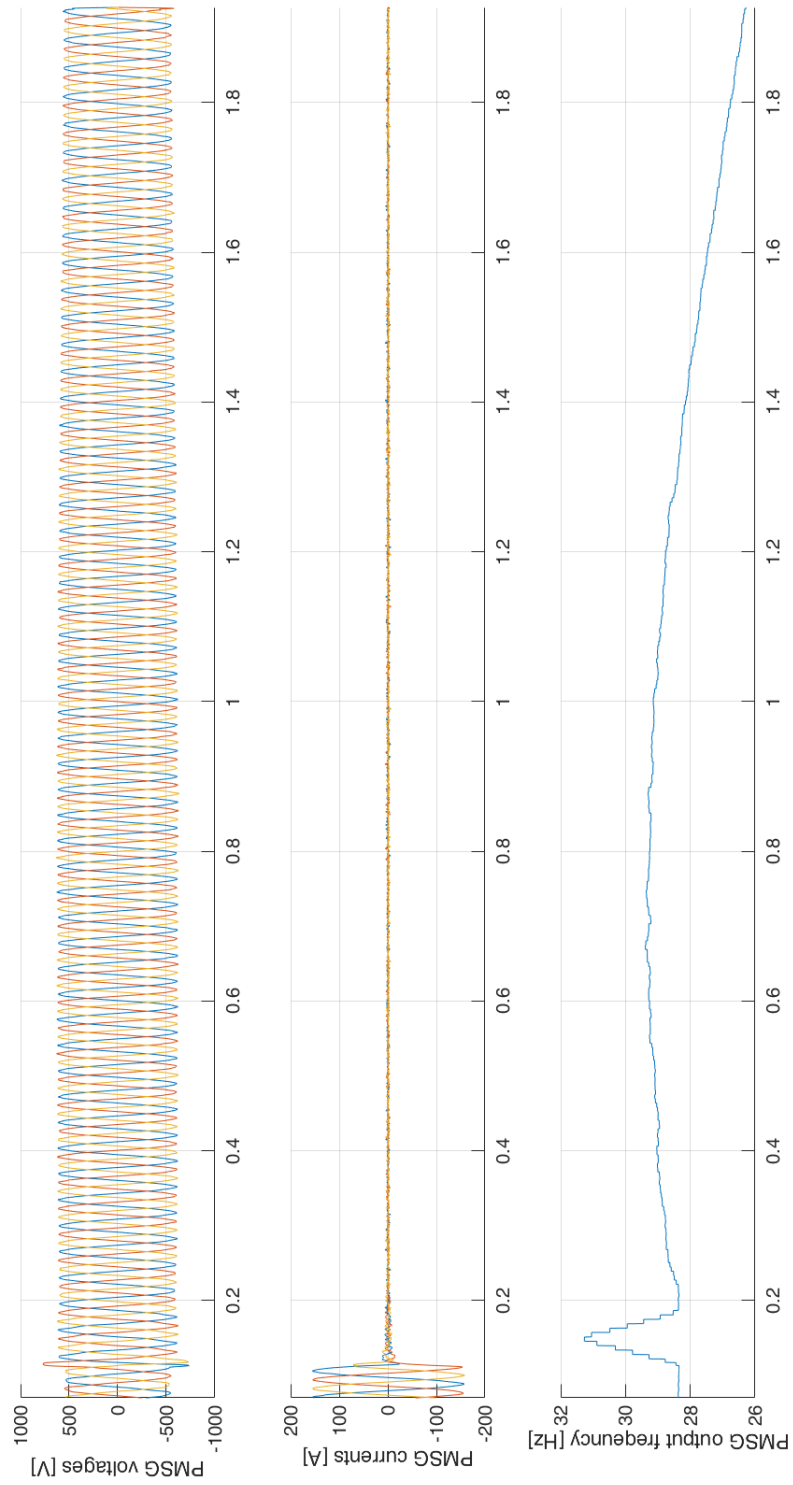


Figure 7.16: WEC disconnection due to a large voltage sag. From top to bottom: phase-to-phase voltages [V], line currents [A],

CONCLUSIONS

Due to the massive increase of wind energy penetration into the distribution grid, the ability of a wind turbine to react correctly to grid faults is becoming more and more important as the correct behavior of a grid characterized by a large penetration of wind turbine energy sources depends on how the electronic WECs interact with the grid, especially during faults.

Since the on-the-field certification tests needed to obtain the LVRT standard compliance are extremely expensive and time consuming, the interest of WT constructors and certification laboratories in cheaper certification processes has led to the identification of new solutions and cheaper test procedures.

Although some solutions have already been proposed, the work described in this thesis shows a novel approach based on a power hardware in the loop system to perform standard compliance tests on electronic WECs. The implemented WT emulator has proven to behave like a real wind turbine during normal and abnormal operating conditions. The tests performed on the entire system show that this approach can be a valid solution to perform certification tests on WT electronic converters directly into development or certification laboratories. More specifically, tests have been performed in laboratory to inspect the WT emulator and the WEC behavior during grid faults. Both balanced and unbalanced voltage sags have been applied to the electronic converter in normal working conditions, and the results were comparable with the on field measurements on a real WT during grid voltage sag.

8.1 FUTURE WORK

The WT emulator needs to be programmed with a series of parameters that identify the electrical and mechanical characteristics of a wind turbine. From a certification laboratory point of view, thrusting the WT constructor on the parameters reliability can not be acceptable. For this reason it can be useful to identify a series of tests to be performed on the real wind turbine, in order to identify or evaluate the correctness of these parameters.

As an example, the inertia of a WT can be identified by disconnecting temporarily the load and observing the rotor speed increase; the generator magnetic flux can be obtained from the output voltages amplitude without load, knowing the generator poles number and the generator rotation speed.

8.2 OTHER APPLICATIONS

The real time hardware emulation platform developed in this work can be used to emulate different hardware structures. As the test bench is based on a power hardware in the loop structure, it can be used to emulate and test different types of power electronics or electromechanical devices, within the system bandwidth and the power capability of the controllable power supply.

As an example, the very same structure has been used to emulate a diesel generator and to perform load change tests to study their effects on the output voltage waveforms. Future studies will focus on using the test bench to emulate a photovoltaic sources in order to test PV energy converters. To do so, the real time hardware needs to be programmed with a detailed model of the P V source, and by disconnecting the isolation transformer from the controllable power supply.

BIBLIOGRAPHY

- [1] ABB. *Technical Application Papers No.13 - Wind Power Plants*. ABB Sace L.V. Breakers, Bergamo, Italy. 2011.
- [2] M.A. Abdullah et al. "A review of maximum power point tracking algorithms for wind energy systems." In: *Renewable and Sustainable Energy Reviews* 16 (2012), pp. 3220–3227.
- [3] International Energy Agency. *Energy and Climate Change*. Available: <http://www.iea.org>. 2015.
- [4] J. C. Ausin et al. *Fault ride-through capability test unit for wind turbines*. Vol. 11. 1. John Wiley & Sons, Ltd., 2008, pp. 3–12. DOI: 10.1002/we.255.
- [5] N. R. Averous et al. "Performance tests of a power-electronics converter for multi-megawatt wind turbines using a grid emulator." In: *Journal of Physics: Conference Series* 753.7 (2016), p. 072015. URL: <http://stacks.iop.org/1742-6596/753/i=7/a=072015>.
- [6] N. R. Averous et al. "Development of a 4 MW Full-Size Wind-Turbine Test Bench." In: *IEEE Journal of Emerging and Selected Topics in Power Electronics* PP.99 (2017), pp. 1–1. ISSN: 2168-6777. DOI: 10.1109/JESTPE.2017.2667399.
- [7] F.D. Bianchi et al. *Wind Turbine Control Systems: Principles, Modeling and Gain Scheduling Design*. Springer, 2007.
- [8] F. Blaabjerg and Z. Chen. *Power electronics for modern wind turbines*. Morgan & Claypool Publishers, 2006.
- [9] F. Blaabjerg et al. "Impact of modulation strategies on power devices loading for 10 MW multilevel wind power converter." In: (June 2012), pp. 751–758.
- [10] A. Buckspan et al. "Combining droop curve concepts with control systems for a wind turbine active control." In: *IEEE Symposium on Power Electronics and Machines in Wind Applications* (2012).
- [11] Yiguang C. et al. "A control strategy of direct driven permanent magnet synchronous generator for maximum power point tracking in wind turbine application." In: (Oct. 2008), pp. 3921–3926.
- [12] T. Caldognetto et al. "Design Controller Development Methodology based on Real-Time Simulation with LabView-FPGA Hardware/Software toolsets." In: *Electronics Journal* 7.2 (Dec. 2014), pp. 110–117.

- [13] T. Caldognetto et al. "Impedance synthesis by inverter control for active loads in anti-islanding testbenches." In: *2016 IEEE Energy Conversion Congress and Exposition (ECCE)*. Sept. 2016, pp. 1–7. DOI: 10.1109/ECCE.2016.7855184.
- [14] T. Caldognetto et al. "Power Electronics Based Active Load for Unintentional Islanding Testbenches." In: *IEEE Transactions on Industry Applications* PP.99 (2017), pp. 1–1. ISSN: 0093-9994. DOI: 10.1109/TIA.2017.2694384.
- [15] R. Carter. *Boat remains and maritime trade in the Persian Gulf during the sixth and fifth millennia BC*. Vol. 80. 307. 2006.
- [16] CEI Comitato Elettrotecnico Italiano. *Standard-CEI 0-16, Reference technical rules for the connection of active and passive consumers to the HV and MV electrical networks of distribution Company*. Standards. 2011.
- [17] CEI Comitato Elettrotecnico Italiano. *Standard-CEI 0-21, Reference technical rules for the connection of active and passive users to the LC electrical Utilities*. Standards. 2011.
- [18] CENELEC. *Standard-CENELEC TS-50549-1, Requirements for the connection of a generating plant to a distribution system - Part 1: Connection to a LV distribution system and above 16A*. Technical Specification. 2015.
- [19] CENELEC. *Standard-CENELEC TS-50549-2, Requirements for the connection of a generating plant to a distribution system - Part 2: Connection to a MV distribution system*. Technical Specification. 2015.
- [20] E.R. Collins and R. Morgan. "A three-phase sag generator for testing industrial equipment." In: *Transactions on power delivery* (1996).
- [21] Global Wind Energy Council. *Global Wind Report*. Available: <http://www.gwec.net>. 2015.
- [22] Global Wind Energy Council. *Global wind energy statistics 2016*. Available: <http://www.gwec.net>. 2017.
- [23] L. Dalla Santa et al. "Implementation of an active RLC load for unintentional islanding test." In: *2016 18th European Conference on Power Electronics and Applications (EPE'16 ECCE Europe)*. Sept. 2016, pp. 1–8. DOI: 10.1109/EPE.2016.7695653.
- [24] S. Das et al. "Time-Domain Modeling of Tower Shadow and Wind Shear in Wind Turbines." In: *ISRN Renewable Energy, HINDAWI* (2011).
- [25] A.B. Dehkordi et al. "Permanent Magnet Synchronous Machine Model for Real-Time Simulation." In: *International Conference on Power Systems Transients (IPST 2005)*. June 2005.
- [26] Energinet. *Technical regulation 3.2.5 for wind power plants with a power output greater than 11kW*. Document 55986/10. 2010.
- [27] E.ON. *Grid code - high and extra high voltage*. E.ON Netz GmbH. 2006.

- [28] N. Espinoza. *Grid Code Testing of Wind Turbines by Voltage Source Converter Based Test Equipment*. Chalmers University of Technology, PHD Thesis, 2016.
- [29] N. Espinoza et al. "Grid code testing of full power converter based wind turbine using back-to-back voltage source converter system." In: *Annual Event Conference Proceedings* (2013). Available: [http:// www.ewea.org/](http://www.ewea.org/).
- [30] Wind Europe. *Wind in Power, 2016 European statistics*. Available: [http:// www.windeurope.org](http://www.windeurope.org).
- [31] FGW. *Standard-FGW Technical Guidelines for Power Generation Units and Farms. Part 3: determination of electrical characteristics of power generating units and systems connected to MV, HV and EHV grids*. Technical Specification. Rev. 23, 2013.
- [32] J. Fletcher and J. Yang. "Introduction to the Doubly-Fed Induction Generator for Wind Power Applications." In: *InTech* (2010).
- [33] G. Gail et al. *Controller design and analysis of a variable speed wind turbine with doubly fed induction generator*. EWEA, The European Wind Energy Association. Available: [http:// www.ewea.org/](http://www.ewea.org/). 2006.
- [34] E.W. Golding. *The Generation of Electricity by Windpower*. E. & F.N. Spon Ltd, 1976.
- [35] M.H. Hansen et al. *Control design for a pitch -regulated, variable speed turbine*. IEA, International Energy Agency. Available: [http:// www.iea.org/](http://www.iea.org/). 2005.
- [36] Md.E. Haque et al. "A Novel Control Strategy for a Variable-Speed Wind Turbine With a Permanent-Magnet Synchronous Generator." In: *Industry Applications, IEEE Transactions on* 46.1 (Jan. 2010), pp. 331–339.
- [37] M.E. Haque et al. "Control of a stand alone variable speed wind turbine with a permanent magnet synchronous generator." In: *Power and Energy Society General Meeting - Conversion and Delivery of Electrical Energy in the 21st Century, 2008 IEEE*. July 2008, pp. 1–9.
- [38] A. Helmedag et al. "Fault Ride Through Certification of Wind Turbines Based on a Hardware in the Loop Setup." In: *Instrumentation and Measurement, IEEE Transactions on* 63.10 (Oct. 2014), pp. 2312–2321. ISSN: 0018-9456. DOI: 10.1109/TIM.2014.2315736.
- [39] A. Helmedag et al. "Testing nacelles of wind turbines with a hardware in the loop test bench." In: *Instrumentation Measurement Magazine, IEEE* 17.5 (Oct. 2014), pp. 26–33. ISSN: 1094-6969. DOI: 10.1109/MIM.2014.6912198.
- [40] V.C. Hernandez et al. *JRC Wind energy status report 2016 Edition*. JRC Science for policy report. 2016.
- [41] J. Hui. *An Adaptive Control Algorithm for Maximum Power Point Tracking for Wind Energy Conversion Systems*. Queen's University, PHD Thesis, 2008.

- [42] IEC International Electrotechnical Commission. *Standard-IEC 61400, Part 4-7: Testing and measurement techniques - General guide on harmonics and interharmonics measurements and instrumentation, for power supply systems and equipment connected thereto*. International Standards. 2002.
- [43] IEC International Electrotechnical Commission. *Standard-IEC 61400, Part 21: Measurement and assessment of power quality characteristics of grid connected wind turbines*. International Standards. 2008.
- [44] IEC International Electrotechnical Commission. *Standard-IEC 61400, Part 4-15: Testing and measurement techniques - Flickermeter - Functional and design specifications*. International Standards. 2010.
- [45] F. Iov et al. "Power electronics control of wind energy in distributed power systems." In: *Optimization of Electrical and Electronic Equipment, 2008. OPTIM 2008. 11th International Conference on*. May 2008, pp. XXIX–XLIV.
- [46] IRENA. *Scaling up variable renewable power: the role fo grid codes*. IRENA International Renewable Energy Agency, Available: [www . irena.org/ Publications](http://www.irena.org/Publications). 2016.
- [47] J. Jonkman et al. *Definition of a 5-MW Reference Wind Turbine for Offshore System Development*. NREL, National Renewable Energy Laboratory. 2009.
- [48] C. Junfei et al. "Modeling and simulation of directly driven wind turbine with permanent magnet synchronous generator." In: (May 2012), pp. 1–5.
- [49] E. Kaya et al. "A method based on the Van der Hoven spectrum for performance evaluation in prediction of wind speed." In: *Turkish Journal of Earth Sciences* 22 (2013), pp. 681–689.
- [50] P. C. Krause. *Analysis of electric machinery*. McGraw-Hill, 1986.
- [51] Z. Lubosny. *Wind Turbine Operation in Electric Power Systems*. Springer, 2003.
- [52] C. Luo et al. "Strategies to Smooth Wind Power Fluctuations of Wind Turbine Generator." In: *IEEE Transactions on Energy Conversions* (2007).
- [53] Darrell M. Dodge. *Wind Power's Beginnings*. Available: [http:// www.telosnet.com/wind/early.html](http://www.telosnet.com/wind/early.html). 2003.
- [54] B. Malinga et al. "Modeling and control of a wind turbine as a distributed resource." In: *System Theory, 2003. Proceedings of the 35th Southeastern Symposium on*. Mar. 2003, pp. 108–112.
- [55] Rui Melicio et al. "Wind Turbines with Permanent Magnet Synchronous Generator and Full-Power Converters: Modelling, Control and Simulation." In: (2011), pp. 465–494.
- [56] Y. Ming et al. "Modeling of the Wind Turbine with a Permanent Magnet Synchronous Generator for Integration." In: (June 2007), pp. 1–6.

- [57] W.S. Mohod and M.V. Aware. "Power Quality and Grid Code Issues in Wind Energy Conversion System." In: (2013).
- [58] M. Mohseni and S.M. Islam. "Review of international grid codes for wind power integration: Diversity, technology and a case for global standard." In: *Renewable and Sustainable Energy Reviews, Elsevier* 16 (2012), pp. 3876–3890.
- [59] S. Muller et al. "Design Controller Development Methodology based on Real-Time Simulation with LabView-FPGA Hardware/Software toolsets." In: *IEEE industry application magazine* (June 2002).
- [60] K. Patil and B. Mehta. "Modeling and simulation of variable speed wind turbine with direct drive permanent magnet synchronous generator." In: *Green Computing Communication and Electrical Engineering (ICGCCEE), 2014 International Conference on*. Mar. 2014, pp. 1–6.
- [61] M. Paz Comech et al. "Wind farms and grid codes." In: *From Turbine to Wind Farms - Technical Requirements and Spin-Off Products* (2011).
- [62] A. Pintea et al. "Optimal control of variable speed wind turbines." In: *Control Automation (MED), 2011 19th Mediterranean Conference on*. June 2011, pp. 838–843. DOI: 10.1109/MED.2011.5983056.
- [63] Z. Quin et al. "A rotating speed controller design method for power leveling by means of inertia energy in wind power systems." In: *Instrumentation and Measurement, IEEE Transactions on energy conversion* 30.3 (Sept. 2015), pp. 1052–1060.
- [64] A. Rolan et al. "Modeling of a variable speed wind turbine with a Permanent Magnet Synchronous Generator." In: *Industrial Electronics, 2009. ISIE 2009. IEEE International Symposium on*. July 2009, pp. 734–739.
- [65] Riccardo Sgarbossa. *Unintentional Islanding in Distribution Networks with Large Penetration of Power Electronics and Renewable Energy Systems*. University of Padova, PHD Thesis, 2016.
- [66] G. V. Siva et al. "Matemactical modeling and simulation of permanent magnet synchronous motor." In: (Aug. 2013).
- [67] J.G. Slootweg et al. "Representing wind turbine electrical generating systems in fundamental frequency simulations." In: *Energy Conversion, IEEE Transactions on* 18.4 (Dec. 2003), pp. 516–524.
- [68] C. Sourkounis and P. Tourou. "Grid Code Requirements for Wind Power Integration in Europe." In: *Conference Papers in Energy* (2013).
- [69] T. Sun et al. "Voltage recovery of grid-connected wind turbines with DFIG after a short-circuit fault." In: 3 (June 2004), 1991–1997 Vol.3.
- [70] V.P. Suppioni and A.P. Grilo. "A Study of Flicker Emission of a Mid-Scale Wind Turbine." In: (2011).

- [71] Herbert J. Sutherland et al. *A retrospective of VAWT technology*. Sandia National Laboratories report. 2012.
- [72] J. Tan et al. "Time-Domain Modeling of Tower Shadow and Wind Shear in Wind Turbines." In: *Energies* 6 (2013), pp. 6352–6372.
- [73] R. Teodorescu et al. *Grid Converters for Photovoltaic and Wind Power Systems*. Wiley-IEEE Press, 2011.
- [74] A. Tessarolo and P. Chowdhury. *Bringing Efficient Communications to Real-Time Motor Control and Power Conversion Applications with TI Viterbi Complex Math Unit (VCU)*. Texas Instruments. 2011.
- [75] *Test and Demonstration Facilities for Wind Energy Needed to Promote a Competitive Wind Industry in Denmark*. Megavind, Danish wind industry association. 2016.
- [76] *TMS320C28x Floating Point Unit and Instruction Set Reference Guide*. Texas Instruments. 2015.
- [77] *TMS320x2803x Piccolo Control Law Accelerator (CLA)*. Texas Instruments. 2009.
- [78] Pinar Tokat. *Development and evaluation of a pitch regulator for a variable speed wind turbine*. Chalmers University of Technology, 2012.
- [79] Isaac Van der Hoven. "Power spectrum of horizontal wind speed in the frequency range from 0.0007 to 900 cycles per hour." In: *Journal of Meteorology* 14 (1956), pp. 160–164.
- [80] Chunxue W. et al. "Vector control strategy for small-scale grid-connected PMSG wind turbine converter." In: (Dec. 2011), pp. 1–7.
- [81] Hu Weihao et al. "Flicker study on variable speed wind turbines with permanent magnet synchronous generator." In: *2008 13th International Power Electronics and Motion Control Conference*. Sept. 2008, pp. 2325–2330.
- [82] D Wenzhong Gao et al. *Comparison of standards and technical requirements of grid-connected wind power plants in China and in the United States*. NREL, National Renewable Energy Laboratory. 2016.
- [83] C. Wessels et al. "Transformer Based Voltage Sag Generator to perform LVRT and HVRT Tests in the Laboratory." In: *14th International Power Electronics and Motion Control Conference, EPE-PEMC*. 2010.
- [84] T. Wizelius. *Wind power projects*. Routledge, 2015.
- [85] B. Wu et al. *Power conversion and control of wind energy systems*. Wiley-IEEE Press, 2011.
- [86] Z. Wu et al. "Operation and Control of a Direct-Driven PMSG-Based Wind Turbine System with an Auxiliary Parallel Grid-Side Converter." In: *Energies* 6 (2013), pp. 3405–3421.

- [87] Jianzhong Zhang et al. "Pitch angle control for variable speed wind turbines." In: *Electric Utility Deregulation and Restructuring and Power Technologies, 2008. DRPT 2008. Third International Conference on*. Apr. 2008, pp. 2691–2696. DOI: 10.1109/DRPT.2008.4523867.